Cell Reports

Article

Anillin forms linear structures and facilitates furrow ingression after septin and formin depletion

Graphical abstract

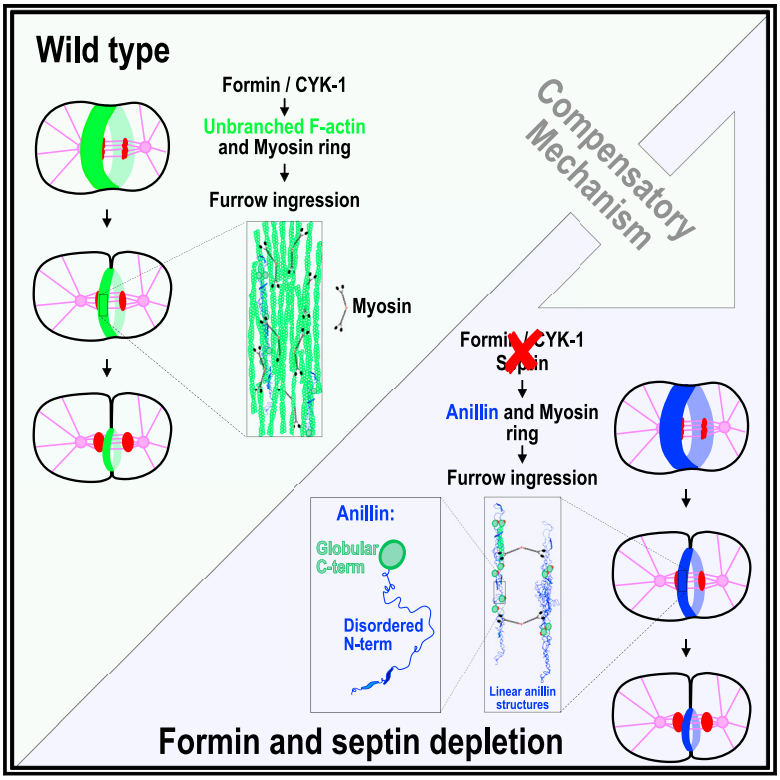

Highlights

- An anillin-dependent compensatory mechanism drives furrowing if F-actin is low
- The disordered anillin N terminus forms linear structures under the plasma membrane
- Non-muscle myosin II represents in independent membrane anchor during cytokinesis
- The anillin ring constricts to form a cleavage furrow when septins are also reduced

Authors

Mikhail Lebedev, Fung-Yi Chan, Anna Lochner, ..., Tamara Mikeladze-Dvali, Ana Xavier Carvalho, Esther Zanin

Correspondence

esther.zanin@fau.de

In brief

During cytokinesis in animal cells, an actin-based ring constricts at the cell equator to form the cleavage furrow. Lebedev et al. discover a compensatory mechanism mediated by linear anillin structures and membrane-bound myosin II that drives cleavage furrow formation and ingression in case actin ring assembly fails.

Lebedev et al., 2023, Cell Reports *42*, 113076
September 26, 2023
https://doi.org/10.1016/j.celrep.2023.113076

CellPress

Cell Reports

CellPress
OPEN ACCESS

Article

Anillin forms linear structures and facilitates furrow ingression after septin and formin depletion

Mikhail Lebedev,[1,2] Fung-Yi Chan,[3,4] Anna Lochner,[1] Jennifer Bellessem,[2] Daniel S. Osório,[3,4] Elisabeth Rackles,[2] Tamara Mikeladze-Dvali,[2] Ana Xavier Carvalho,[3,4] and Esther Zanin[1,2,5,*]

[1]Friedrich-Alexander-Universität Erlangen-Nürnberg, Department Biologie, 91058 Erlangen, Germany
[2]Department Biologie, Ludwig-Maximilians University, Munich, 82152 Planegg-Martinsried, Germany
[3]i3S - Instituto de Investigação e Inovação em Saúde (i3S), Universidade do Porto, 4200-135 Porto, Portugal
[4]IBMC - Instituto de Biologia Molecular e Celular, Universidade do Porto, 4200-135 Porto, Portugal
[5]Lead contact
*Correspondence: esther.zanin@fau.de
https://doi.org/10.1016/j.celrep.2023.113076

SUMMARY

During cytokinesis, a contractile ring consisting of unbranched filamentous actin (F-actin) and myosin II constricts at the cell equator. Unbranched F-actin is generated by formin, and without formin no cleavage furrow forms. In *Caenorhabditis elegans*, depletion of septin restores furrow ingression in formin mutants. How the cleavage furrow ingresses without a detectable unbranched F-actin ring is unknown. We report that, in this setting, anillin (ANI-1) forms a meshwork of circumferentially aligned linear structures decorated by non-muscle myosin II (NMY-2). Analysis of ANI-1 deletion mutants reveals that its disordered N-terminal half is required for linear structure formation and sufficient for furrow ingression. NMY-2 promotes the circumferential alignment of the linear ANI-1 structures and interacts with various lipids, suggesting that NMY-2 links the ANI-1 network with the plasma membrane. Collectively, our data reveal a compensatory mechanism, mediated by ANI-1 linear structures and membrane-bound NMY-2, that promotes furrowing when unbranched F-actin polymerization is compromised.

INTRODUCTION

During cytokinesis, a contractile ring consisting of unbranched filamentous actin (F-actin) and non-muscle myosin II assembles underneath the plasma membrane between the segregating chromosomes. Constriction of the actin-myosin ring splits the mother cell into two daughter cells.[1–3] Stimulatory and inhibitory signals emanating from the mitotic spindle activate RhoA at the cell equator, which in turn induces contractile ring assembly.[4–11] Active RhoA releases the autoinhibitory conformation of formin with the help of the contractile ring component anillin and IQGAP1.[12–15] Anillin is a widely conserved protein that links the actin-myosin ring with the plasma membrane.[1,2,16,17] Active formin binds to the barbed end of actin filaments and induces the polymerization of long unbranched F-actin.[18] F-actin circumferentially aligns around the cell equator, which is thought to facilitate furrow ingression.[19–23] Without formin, cleavage furrow formation and cytokinesis fail.[24–27]

In addition to formin, RhoA also recruits and activates non-muscle myosin II (NMY-2 in *Caenorhabditis elegans*) via RhoA kinase. The myosin motor domain interacts with unbranched F-actin, and myosin II is required for cytokinesis in many systems.[28–30] To be active, myosin II has to bind the phosphorylated regulatory light chain (RLC) and essential light chain (ELC).[31] In addition to RhoA-dependent myosin II recruitment, a positive-feedback mechanism between ring myosin II and equatorial-directed cortical flows that brings more myosin II into the ring dictates the amount of myosin II in the contractile ring.[32] Nevertheless, myosin II can enrich at the cell equator independently of its binding partner F-actin or anillin.[33,34] Myosin II inhibition does not prevent the recruitment of other ring components to the equator but blocks ring constriction.[28,35,36] In fission yeast, myosin II is targeted to the membrane by the anillin homolog Mid1p[37,38] and, together with formin and numerous other proteins, they form defined protein assemblies called nodes.[39–42] Within each node, myosin II heads point away from the membrane and grab and pull on actin filaments generated and anchored at adjacent nodes.[40,41,43] This leads to the coalescence of nodes and eventually ring constriction.[3]

Another component of the contractile ring is the multidomain protein anillin (ANI-1 in *C. elegans*).[1,2,16,17] Anillin is considered a scaffolding component of the contractile ring that links the actin-myosin ring with the plasma membrane. With its C terminus, anillin interacts with microtubules,[44] with lipids and importin[45] through the C2 domain, with membrane-associated active RhoA via the RhoA-binding domain (RBD),[46,47] and with septins via the PH domain.[48–52] With its N terminus, anillin binds to myosin II,[53] F-actin,[49,54–57] and formins.[13,58] Anillin localization

to the cell equator requires RhoA activation but not myosin II, F-actin, septins, or formins.[27,33,34,53,59] Consistent with its role as a membrane-actomyosin linker, anillin depletion results in unstable furrows and in cytokinesis failure in fly and human cells.[33,46,53,60] ANI-1 depletion in the one-cell *C. elegans* zygotes does not cause cytokinesis failure but results in symmetric furrow ingression.[34,61] Anillin positively feeds back on RhoA activity[46] by stabilizing active RhoA at the membrane,[62] and anillin also binds and recruits septins to the contractile ring.[33,34,48,50,52] Recent *in vitro* work suggests that anillin could contribute to force generation and ring constriction independently of myosin II.[63]

Besides F-actin and myosin II, septins are the third filament-forming protein of the contractile ring, and septins bind the plasma membrane.[64] Similar to anillin, septins are required for cytokinesis in human cells[65] but are not essential in *C. elegans* zygotes. Whereas humans have 13 septins, *C. elegans* has two septins, which are only essential for some postembryonic divisions.[66] Together, septin and anillin also function during the late stages of cytokinesis.[65,67–69]

During the initial assembly phase, ring components such as F-actin, myosin II, and anillin localize in a broad equatorial band, which subsequently compacts into the contractile ring.[70] Super-resolution microscopy in sea urchin embryos revealed that myosin II, anillin, and septin initially co-localize in puncta reminiscent of the nodes in yeast.[71] Subsequently, a dense meshwork forms in which myosin II filaments orient parallel to actin filaments.[20,72,73] This organization is consistent with myosin II mediating ring constriction by actin filament sliding in a purse-string-like fashion. Consistently myosin II motor activity is required for ring constriction.[74]

Although actin-based contractility appears to be the predominant mechanism for furrow ingression, alternative mechanisms were also reported sporadically. For example, the migration of the two daughter cells away from each other supports furrow ingression in the absence of a visible F-actin ring in human RPE1 cells and in *Dictyostelium*.[75–77] In *Chlamydomonas*, furrow ingression does not require F-actin.[78] In *C. elegans*, depletion of septin in a formin (CYK-1) temperature-sensitive (ts) mutant restored furrow ingression, although no F-actin ring was detectable.[79] Here we investigate the mechanism of furrow ingression after co-depletion of CYK-1 and septins in the *C. elegans* embryo. We uncover a compensatory ANI-1-dependent mechanism of cleavage furrow ingression when unbranched F-actin is low.

RESULTS

ANI-1 is required for furrow ingression after CYK-1 and septin co-depletion

CYK-1 is the only *C. elegans* formin known to be essential for cytokinesis.[24,25,80,81] Surprisingly, it was found that *cyk-1ts* mutant embryos, which have strongly reduced unbranched F-actin levels, still ingress a cleavage furrow when septins are depleted (Figure 1A).[79,81] We confirmed this observation as CYK-1 depletion by RNAi prevented cleavage furrow formation but septin^{UNC-61} co-depletion facilitated cleavage furrow ingression in all embryos (Figures 1B and 1C; Video S1). In five out of 10 *cyk-1(RNAi); septin^{unc-61}(RNAi)* embryos, the furrow remained closed until the onset of the second cell division. In the remaining embryos, the furrow eventually regressed around 800 s after nuclear envelope breakdown (NEBD) (Figures 1B and 1C). *C. elegans* has two septins (UNC-61 and UNC-59), which depend on each other for membrane localization[66]; therefore, depletion of one is expected to disrupt the function of the complex. Consistently, we observed that GFP-tagged septin^{UNC-59} did not localize to the cortex after *septin^{unc-61}(RNAi)* or *cyk-1(RNAi);septin^{unc-61}(RNAi)* (Figures S1A and S1B). Although the cortical accumulation of septin^{UNC-59} was strongly diminished after septin^{UNC-61} depletion, we tested whether the furrow still ingressed in *cyk-1(RNAi)* embryos after the co-depletion of both septins. In septin^{UNC-59} and septin^{UNC-61} co-depleted embryos treated with *cyk-1(RNAi)*, the cleavage furrow fully ingressed in 88% of the cases, which demonstrates that furrowing can occur after co-depletion of both *C. elegans* septins (Figure S1C). Immunoblot analysis of adult worms revealed that *septin^{unc-59}(RNAi)* and *cyk-1(RNAi)* strongly reduced endogenously tagged septin^{UNC-59} and CYK-1 protein levels, respectively (Figure S1D).

Septin depletion rescued furrow ingression after *cyk-1(RNAi)* and therefore we determined whether cortical CYK-1 levels were altered. Equatorial CYK-1 levels were slightly increased after septin^{UNC-61} depletion (Figure S1E), but, importantly, no equatorial enrichment of CYK-1 was observed after *cyk-1(RNAi)* or *cyk-1(RNAi);septin^{unc-61}(RNAi)* (Figure S1F). Similarly, equatorial F-actin no longer accumulated at the cell equator after single or double *cyk-1(RNAi)* treatments, confirming previous observations[79,81–83] (Figure S1F). This suggests that septin^{UNC-61} depletion does not rescue furrow ingression in *cyk-1(RNAi)* embryos by elevating either equatorial CYK-1 or F-actin levels.

In addition to formin-nucleated F-actin, the cortex contains Arp2/3 nucleated branched F-actin.[83] Thus, we tested whether the remaining Arp2/3-generated F-actin contributes to furrowing in CYK-1 and septin co-depleted embryos by additional depletion of the Arp2 homolog ARX-2. All *cyk-1(RNAi); septin^{unc-61}(RNAi);arx-2(RNAi)* embryos fully ingressed a cleavage furrow (Figures S2A and S2B), suggesting that Arp2/3-generated F-actin is not essential for furrowing in this condition.

To address the mechanism how CYK-1 and septin co-depleted embryos ingress a cleavage furrow, we determined whether ANI-1 is required for furrow ingression. Although ANI-1 depletion alone does not cause cytokinesis failure,[34] ANI-1 depletion together with CYK-1 and septin^{UNC-61} prevented furrow ingression (Figures 1B and 1C). Similar to septin^{UNC-61} depletion, *ani-1(RNAi)* resulted in a increase in equatorial CYK-1 levels (Figure S1E), but, in contrast, it did not rescue furrow ingression after *cyk-1(RNAi)* (Figure S2C). Immunoblot analysis of ANI-1 protein levels showed that ANI-1 levels were strongly reduced (Figure S2D). Further, imaging endogenously NeonGreen-tagged ANI-1 (NG::ANI-1) confirmed that ANI-1 depletion was highly efficient in all RNAi conditions (Figure S2E). Together, ANI-1 promotes furrow ingression in case CYK-1 and septin levels are low.

ANI-1 localizes to septin-independent linear structures, especially after the depletion of the formin CYK-1

Since ANI-1 was required for furrow ingression, we analyzed ANI-1 localization on the cortex during contractile ring assembly.

CellPress
OPEN ACCESS

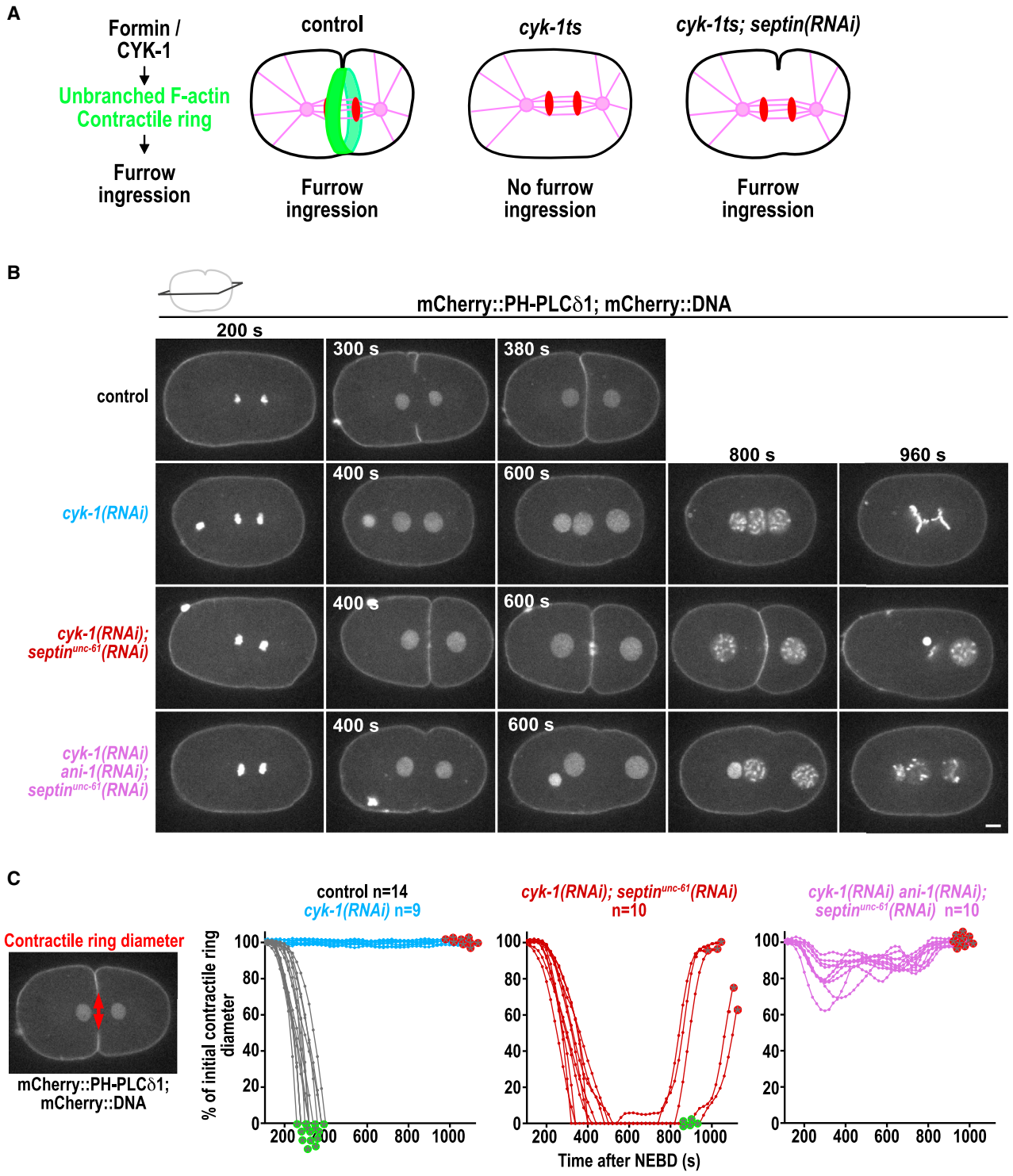

Figure 1. Furrow ingression of *cyk-1(RNAi);septin*$^{unc-61}$*(RNAi)* embryos requires ANI-1

(A) During cytokinesis, CYK-1 polymerizes the unbranched F-actin of the contractile ring. In *cyk-1ts* mutants, no contractile ring forms and cytokinesis fails, but, surprisingly, furrow ingression was restored by depleting septin.[79]

(B) Central plane images of embryos expressing a membrane and DNA marker, treated with the indicated RNAi conditions. Time is indicated in seconds (s) after NEBD. Scale bar, 5 μm.

(C) The contractile ring diameter is plotted over time for individual embryos for indicated RNAi conditions. Green and red encircled stars indicate whether embryos succeed or fail cytokinesis, respectively. n = number of embryos.

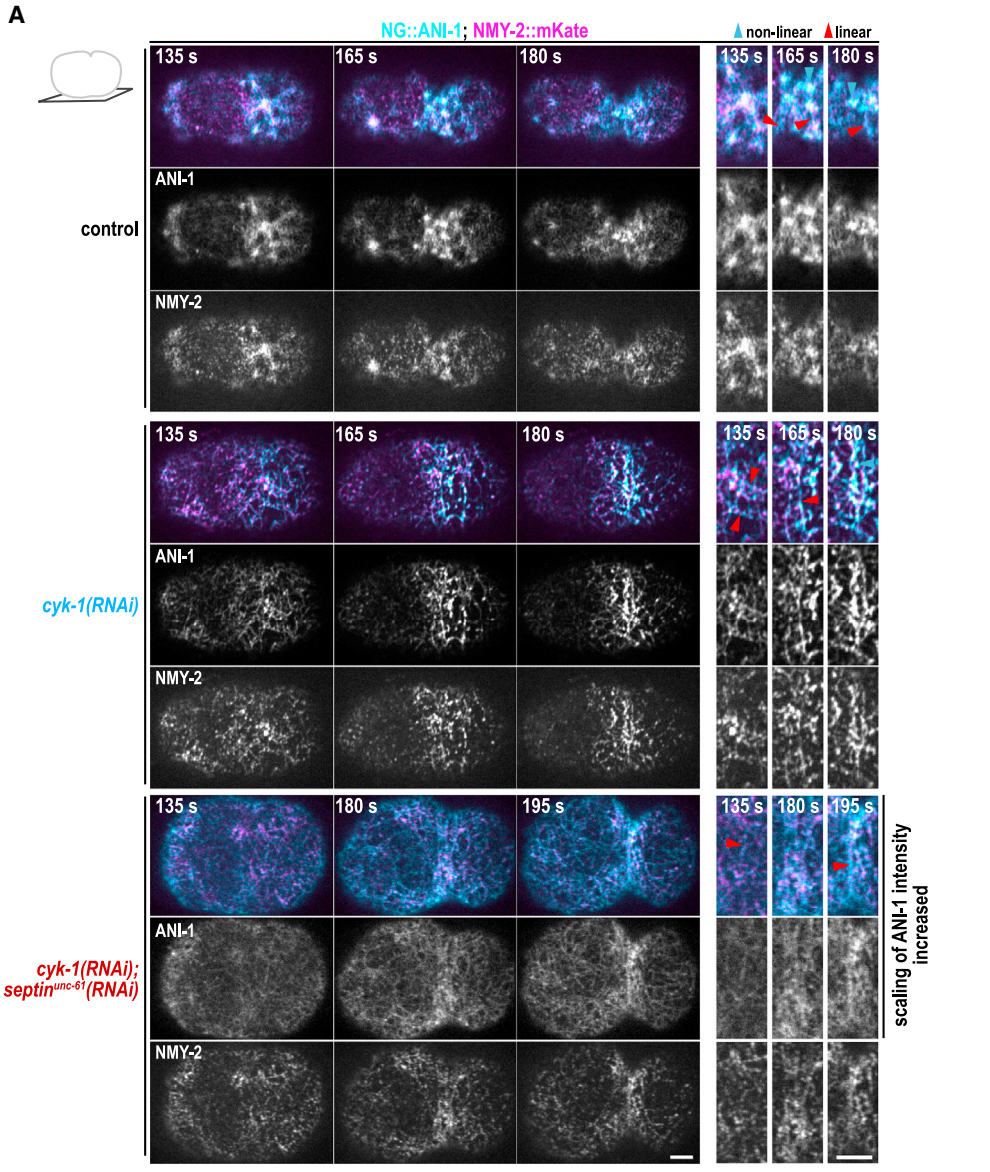

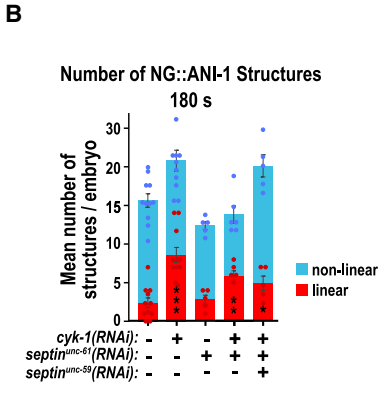

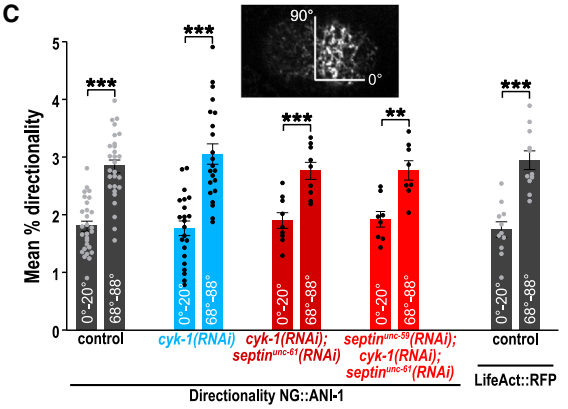

(legend on next page)

In control anaphase embryos, ANI-1 was enriched in cortical patches as previously published[70] but also localized in linear structures, which sometimes radiate out of cortical patches (Figure 2A; Video S2). Comparison of the localization of ANI-1 with myosin II (NMY-2::mKate) revealed that NMY-2 was also present in these cortical patches[84] and occasionally decorated the linear ANI-1 structures. In CYK-1-depleted embryos, cortical ANI-1 patches were absent and numerous linear structures, decorated with NMY-2, formed (Figure 2A; Video S2). Quantification revealed that linear ANI-1 structures were occasionally observed in control embryos and after *cyk-1(RNAi)* their number increased (Figures 2B and S3A). In *cyk-1(RNAi)* linear ANI-1 structures had a length of ~2–9 μm and width of ~0.5 μm. To determine whether the overall ANI-1 distribution was altered, ANI-1 fluorescence intensity was measured along the cell cortex. ANI-1 was still enriched in an equatorial zone after *cyk-1(RNAi)* and *cyk-1(RNAi); septin^{unc-61}(RNAi)* and its cortical levels were decreased in the latter (Figures 2A and S3B). Reduction of cortical ANI-1 levels is consistent with the fact that septins bind and contribute to anillin recruitment in other organisms.[48,49,85,86] Linear ANI-1 structures were still detected in *cyk-1(RNAi)* embryos co-depleted of septin^{UNC-61} alone or septin^{UNC-59} and septin^{UNC-61} together (Figures 2A, 2B, and S3C). Measurement of the orientation of ANI-1 revealed that ANI-1 circumferentially aligns around the cell equator similar to F-actin in control embryos (Figure 2C). Reduction of unbranched F-actin alone or together with septin^{UNC-61} or with septin^{UNC-59} and septin^{UNC-61} did not alter alignment of ANI-1 (Figure 2C).

Since ANI-1 appeared to form those linear structures, we determined whether septin also localized to linear structures after *cyk-1(RNAi)*. Indeed, we observed that, after *cyk-1(RNAi)*, septin^{UNC-59} was also present in linear structures and its cortical intensity levels were increased (Figures S3D–S3F). In contrast to the linear ANI-1 structures, which could still be observed after *septin^{unc-61}(RNAi)*, septin^{UNC-59} was no longer enriched at the cell equator after *ani-1(RNAi)* (Figures S4D and S4E[34]). This shows that septin^{UNC-59} fully depends on the presence of ANI-1 for equatorial enrichment, but, in contrast, a pool of ANI-1 localizes independently of septins to the cortex.

Since reduction of CYK-1-nucleated unbranched F-actin altered ANI-1 localization, we analyzed whether Arp2/3-nucleated branched F-actin also has an influence on ANI-1. Consistent with previous reports, we observed a reduction of F-actin foci, a delay in furrow formation, and ANI-1 accumulation after *arx-2(RNAi)* (Figures S4A–S4C).[36,83,87] However, ARX-2 depletion did not affect ANI-1 localization to linear structures in control or *cyk-1(RNAi)* embryos (Figures S4B and S4D; Video S3).

In summary, CYK-1-nucleated unbranched F-actin limits the formation of linear ANI-1 structures. Septin co-depletion did not affect the formation of linear ANI-1 structures, although efficient ANI-1 targeting to the cell equator required septin function.

NMY-2 is required for the orientation of the linear ANI-1 structures and furrow ingression in embryos depleted of CYK-1 and septin

We found that ANI-1 forms linear structures decorated by NMY-2 and supports furrow ingression in *cyk-1(RNAi);septin^{unc-61}(RNAi)* embryos. To test whether NMY-2 is required for the formation or alignment of the linear ANI-1 structures, we depleted NMY-2 together with CYK-1 or CYK-1 and septin^{UNC-61}. Immunoblot analysis and quantification of cortical NMY-2 fluorescence intensity confirmed that *nmy-2(RNAi)* strongly reduced NMY-2 protein levels in all RNAi conditions (Figures S5A–S5C). Depletion of NMY-2 alone or in combination with CYK-1 or CYK-1 and septin^{UNC-61} did not prevent linear ANI-1 structure formation, although they were no longer circumferentially aligned around the cell equator (Figures 3A–3C; Video S4). This suggests that NMY-2 aligns linear ANI-1 structures, perhaps by directly binding to the ANI-1 N terminus. In normal cytokinesis, myosin II binds and aligns F-actin and mediates furrow ingression,[74] so we asked whether NMY-2 still mediates furrow ingression in *cyk-1(RNAi);septin^{unc-61}(RNAi)* embryos. NMY-2 co-depletion abolished furrow ingression in *cyk-1(RNAi);septin^{unc-61}(RNAi)* embryos (Figures 3D and S5D), although ANI-1 was still enriched at the cell equator (Figures 3A and S5E). In conclusion, NMY-2 is absolutely required to mediate furrow ingression after the reduction of CYK-1 and septins. Further, NMY-2 is involved in aligning the linear ANI-1 structures circumferentially but is not essential for their formation.

ANI-1 and NMY-2 form membrane-localized structures in the absence of F-actin independently of the ANI-1 N terminus

After depolymerization of F-actin in *Drosophila* cells, anillin and the RLC of myosin II enrich in circular foci that evolve into linear structures, and these structures also form independently of each other.[33,49,52,59] In the *C. elegans* zygote, NMY-2 also forms circular foci after Latrunculin A addition.[88,89] However, whether ANI-1 is also present in those circular NMY-2 foci and whether linear structures still form after F-actin depolymerization have not been investigated in *C. elegans*. To study this, we treated embryos with Latrunculin A, which caused a rapid disappearance of F-actin from the cortex and the appearance of dynamic NMY-2 and ANI-1 structures (Figures S6A–S6E; Video S5). After loss of cortical F-actin, NMY-2 and ANI-1 co-localized in

Figure 2. ANI-1 forms linear structures decorated by NMY-2 foci when CYK-1-nucleated F-actin levels are low

(A) Cortical confocal images of NG::ANI-1 (cyan) and NMY-2::mKate (magenta) for indicated RNAi conditions and time points after NEBD. Magnifications of the equatorial region are shown. Since NG::ANI-1 levels are reduced after septin^{UNC-61} co-depletion (Figure S3B), intensity scaling was increased. Non-linear (blue) and linear (red) structures are highlighted by arrowheads. Scale bars, 5 μm.

(B) The mean number of linear and non-linear NG::ANI-1 structures at an equatorial region (Figure S3A) for indicated RNAi conditions. The p values were calculated using Mann-Whitney U or Student's t test: *p < 0.05, **p < 0.01, and ***p < 0.001 in comparison to control embryos treated without RNAi.

(C) Mean percentage of 0°–20° (anterior to posterior) and 68°–88° (circumferential) directionality measured for NG::ANI-1 and LifeAct::RFP at 180 s after NEBD for indicated RNAi conditions. The p values were determined with Student's t test: **p < 0.01, ***p < 0.001.

All error bars indicate SEM, and dots represent data points of individual embryos.

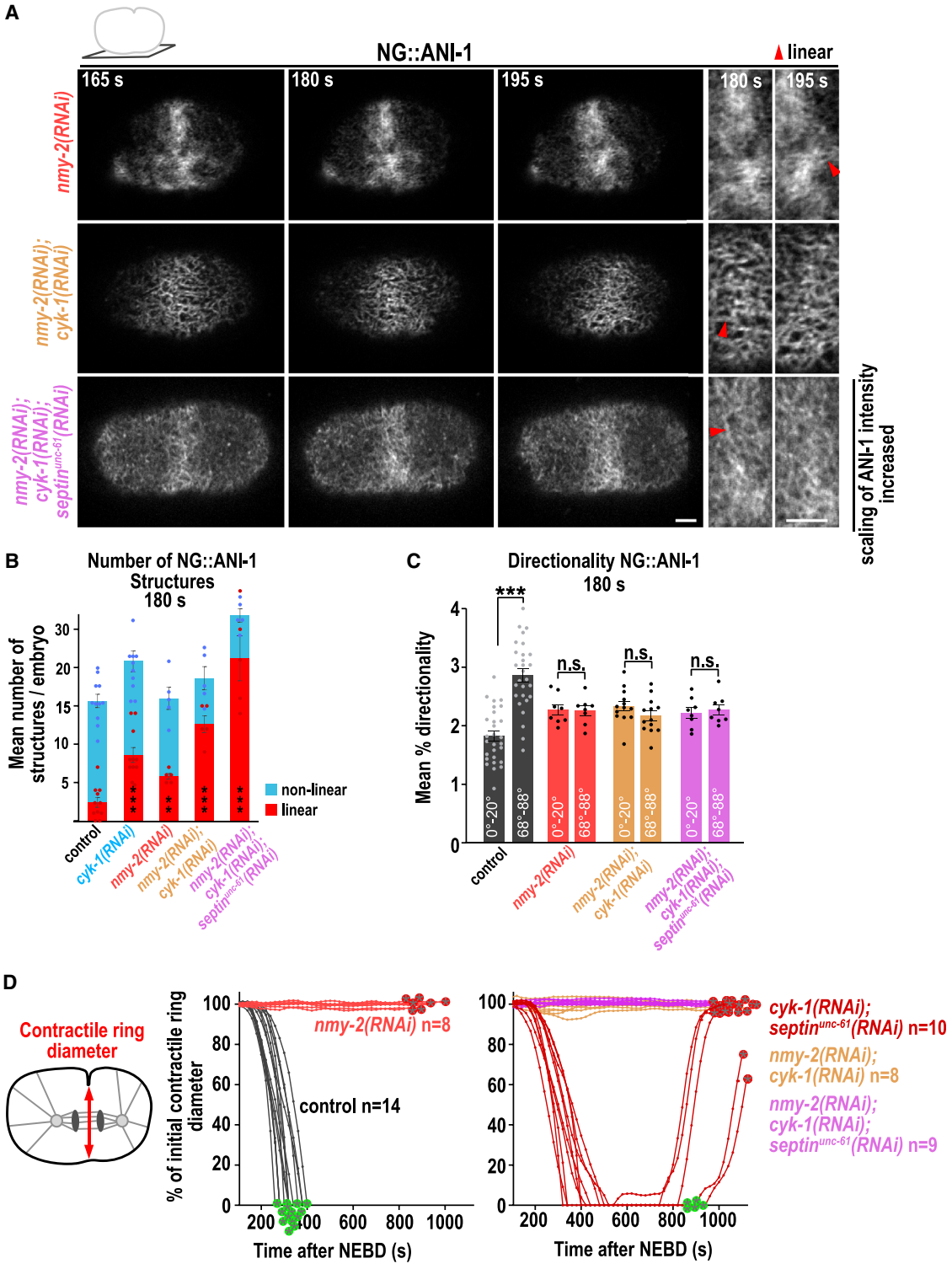

Figure 3. NMY-2 is not required for the formation of the linear ANI-1 structures but for their circumferential alignment

(A) Cortical confocal images of NG::ANI-1 for indicated RNAi conditions and time points after NEBD. Magnifications of the equator are shown (right). Since NG::ANI-1 levels are reduced after *septin*$^{unc-61}$*(RNAi)*, intensity scaling was increased. Linear structures are highlighted by red arrowheads. Scale bars, 5 μm.

(B) Mean number of NG::ANI-1 structures at the equator for indicated RNAi conditions. The p values were calculated using Mann-Whitney-U or Student's t test: **p < 0.01, ***p < 0.001 in comparison to control embryos; dots represent data points of individual embryos. Control and *cyk-1(RNAi)* conditions are reproduced from Figure 2B.

(legend continued on next page)

numerous non-linear structures that became linear at later time points (Figures 4A and 4B). Measurement of fluorescence intensities revealed that, upon F-actin depolymerization, NMY-2 and ANI-1 accumulated in an equatorial zone similar to control embryos, although NMY-2 fluorescence was increased at 255 s (Figure S6F). To test whether the linear structures are septin dependent, we repeated Latrunculin A treatment after septin^{UNC-61} depletion. In Latrunculin A-treated *septin^{unc-61}(RNAi)* embryos, linear ANI-1 structures were still present; however, they were less frequent and defined than those in Latrunculin A-only-treated embryos (Figures S7A and S7B; Video S6). Finally, we tested whether *septin^{unc-61}(RNAi)* restores furrow ingression in Latrunculin A-treated embryos like it does in *cyk-1(RNAi)* embryos. No cleavage furrow formed in Latrunculin A-treated control or *septin^{unc-61}(RNAi)* embryos (Figure S7C). This suggests, although F-actin does not enrich at the cell equator in *cyk-1(RNAi);septin^{unc-61}(RNAi)* embryos, some residual F-actin contributes to furrow ingression in those embryos.

Vertebrate anillin binds myosin II with its N terminus[53] and the co-localization of anillin and myosin II requires the anillin N terminus in *Drosophila* cells.[91] Since NMY-2 and ANI-1 structures co-localize after Latrunculin A treatment and NMY-2 is expected to interact with the ANI-1 N terminus, we analyzed whether ANI-1 and NMY-2 still form structures that co-localize when the N terminus of ANI-1 is absent. We used an ANI-1 fragment that comprises the RBD, C2, and PH domain (Δ1–680, ANI-1^{AH-PH}[90]) and depleted endogenous ANI-1 by RNAi to prevent NMY-2 binding via full-length endogenous ANI-1. After Latrunculin A addition, NMY-2 and ANI-1^{AH-PH} both formed circular structures, but these did not co-localize and did not become linear over time (Figures 4C and 4D; Video S7). This shows that the N terminus of ANI-1 is required for the formation of linear but not non-linear structures and is essential for the co-localization with NMY-2 structures.

Since NMY-2 formed membrane-localized structures independently of its binding partner F-actin and of the ANI-1 N terminus, we hypothesized that NMY-2 could bind the membrane directly. To test this, we purified NMY-2 in a complex with the myosin ELC (MLC-4) and the myosin RLC (MLC-5). We found that the NMY-2/MLC-4/MLC-5 complex, but not MLC-4 alone, bound to several lipids known to be enriched in the plasma membrane (Figures 4E and 4F).

In summary, in the absence of F-actin, ANI-1 and NMY-2 co-localize to non-linear and linear structures and linear structure formation requires the ANI-1 N terminus and is facilitated by septin^{UNC-61}. The co-localization but not the formation of the ANI-1 and NMY-2 non-linear structures requires the ANI-1 N terminus, suggesting that the binding of NMY-2 to the ANI-1 N terminus pulls those structures together. The NMY-2/MLC-4/MLC-5 complex bound to several membrane lipids, suggesting that this complex likely represents an independent membrane anchor.

The linker region of ANI-1 facilitates linear structure formation

ANI-1 contains multiple distinct domains: an actin-binding domain (ABD)[55] and a predicted myosin II-binding domain (MBD)[34] at the N terminus, and an RBD, a C2 membrane-binding domain, and a PH domain at the C terminus[47] (Figure S8A). Sequence analysis predicts that the ANI-1 N terminus contains numerous intrinsically disordered regions (IDRs) similar to human anillin (Figures S8A and S8B) and yeast Mid1p.[92]

To analyze which region of ANI-1 is required for linear structure formation, we generated *ani-1* RNAi-resistant transgenes in which the MBD (Δ48–160), the ABD (Δ236–460), the MBD and ABD (Δ48–460), and the entire N-terminal half (ANI-1^{C-term} Δ48–680) were deleted (Figures 5 and S8C–S8F). As a control we generated wild-type ANI-1 transgene (ANI-1^{WT}), which rescued embryonic lethality after *ani-1(RNAi)* and localized to circumferentially aligned linear structures after CYK-1 depletion, together suggesting that it is functional (Figures 5A–5C, S8F, and S9A; Video S8).

All ANI-1 transgenes were found to express at similar levels as ANI-1^{WT} (Figure S8E), and the MBD (Δ48–160), the ABD (Δ236–460), and the MBD and ABD (Δ48–460) deletion variants fully rescued embryonic lethality in the absence of endogenous ANI-1. The ANI-1^{C-term} rescued lethality only partially after *ani-1(RNAi)* (Figure S8F). After *ani-1(RNAi)* or *cyk-1(RNAi)ani-1(RNAi)*, the Δ48–160, Δ236–460, and Δ48–460 ANI-1 mutants enriched at the cell equator and formed linear structures that circumferentially aligned comparably to those of ANI-1^{WT} (Figures 5A–5D and S9A–S9C; Videos S8, and S9). Furthermore, the ANI-1 Δ48–460 still formed some linear structures in the presence of Latrunculin A (Figures S9D and S9E; Video S10). After co-depletion of CYK-1 and septin^{UNC-61}, the cortical levels of ANI-1 Δ48–460 were strongly reduced and only pulsatile accumulation was visible, but the levels of ANI-1 Δ48–160 and ANI-1 Δ236–460 were comparable to those of ANI-1^{WT} (Figures 5D; Video S9). In those embryos, ANI-1 Δ48–160 and ANI-1 Δ236–460 still formed linear structures that aligned circumferentially around the cell equator (Figures 5C and S9A–S9C; Video S9).

Since the MBD and ABD were not required for linear structure formation in *cyk-1(RNAi)*, we analyzed the ANI-1^{C-term}, which lacks the MBD, ABD, and the linker region. The ANI-1^{C-term} formed very few linear but numerous non-linear structures after *ani-1(RNAi)*. After *cyk-1(RNAi)ani-1(RNAi)*, the few ANI-1^{C-term} linear structures were completely absent and instead numerous non-linear structures that did not circumferentially align were present (Figures 5C, 5E, and S9A; Video S8). This demonstrates that the presence of the linker region is required for linear structure formation. Co-depletion of CYK-1 and septin^{UNC-61} resulted in a strong reduction of cortical ANI-1^{C-term} levels in comparison to ANI-1^{WT} levels, but transient pulsatile accumulation of ANI-1^{C-term} was still observed (Figures 5B and 5E; Video S8). The absence of non-linear

(C) Mean percentage of directionality for NG::ANI-1 for indicated RNAi conditions. The p values were determined with Student's t test: ***$p < 0.001$; n.s., $p > 0.05$. Control condition is reproduced from Figure 2C.

(D) Plotted is the contractile ring diameter over time for indicated RNAi conditions. Green and red encircled stars indicate whether embryos succeed or fail cytokinesis, respectively. Control and *cyk-1(RNAi);septin^{unc-61}(RNAi)* conditions are reproduced from Figure 1C; n = number of embryos.

All error bars indicate SEM.

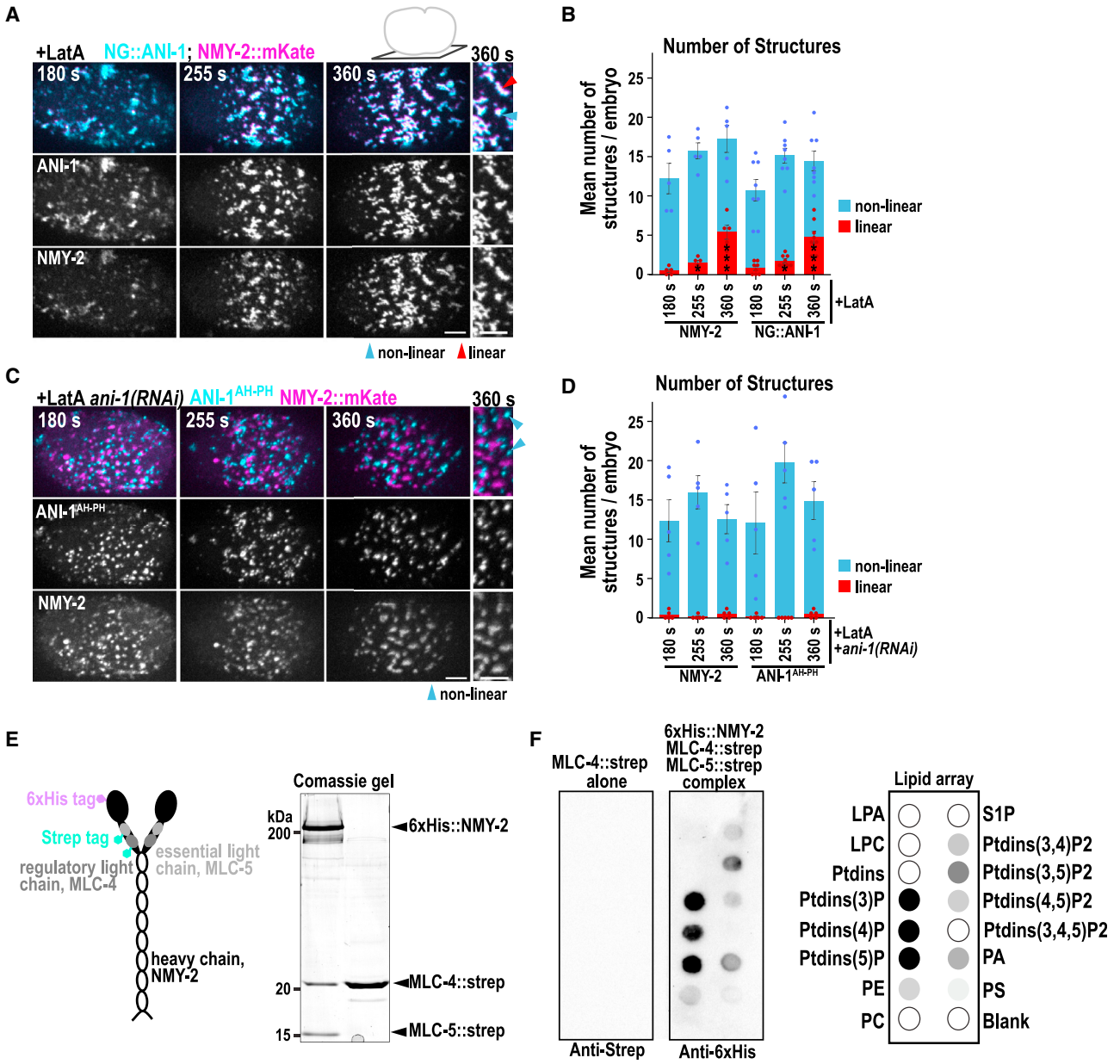

Figure 4. NMY-2 forms membrane-localized structures independently of F-actin and the ANI-1 N terminus and interacts with lipids *in vitro*

(A) Maximum intensity projections of 10 cortical z planes of embryos treated with Latrunculin A (+LatA) expressing NG::ANI-1 (cyan) and NMY-2::mKate (magenta). A magnification of the equator is shown (right).

(B) Mean number of NMY-2::mKate and NG::ANI-1 structures at the cell equator after Latrunculin A treatment. The p values were calculated using Mann-Whitney-U or Student's t test: *p < 0.05, ***p < 0.001 in comparison to 180 s; dots represent data points of individual embryos.

(C) Maximum intensity projections of 10 cortical z planes of embryos expressing ANI-1^{AH-PH},[90] (cyan) and NMY-2::mKate (magenta) treated with Latrunculin A and *ani-1(RNAi)*. A magnification of the equator is shown.

(D) Mean number of NMY-2::mKate and ANI-1^{AH-PH} structures at the equator after *ani-1(RNAi)* and Latrunculin A treatment.

(E) Coomassie-stained gel of Strep-tagged MLC-4 alone or in complex with 6xHis-tagged NMY-2 and Strep-tagged MLC-5.

(F) Purified MLC-4 alone or in complex with 6xHis-tagged NMY-2 and Strep-tagged MLC-5 were incubated with lipid arrays and blotted with anti-Strep or anti-6xHis antibodies (left). Schematics of the lipid array: LPA, lysophosphatidic acid; LPC, lysophosphatidylcholines; PtdIns, phosphatidylinositol; PE, phosphatidylethanolamine; PC, phosphatidylcholines; S1P sphingosine-1-phosphate; PA, phosphatidic acid; PS, phosphatidylserine (right).

Non-linear (blue) and linear (red) structures are highlighted by arrowheads. All error bars indicate SEM; scale bars, 5 μm; time (s) is displayed after NEBD.

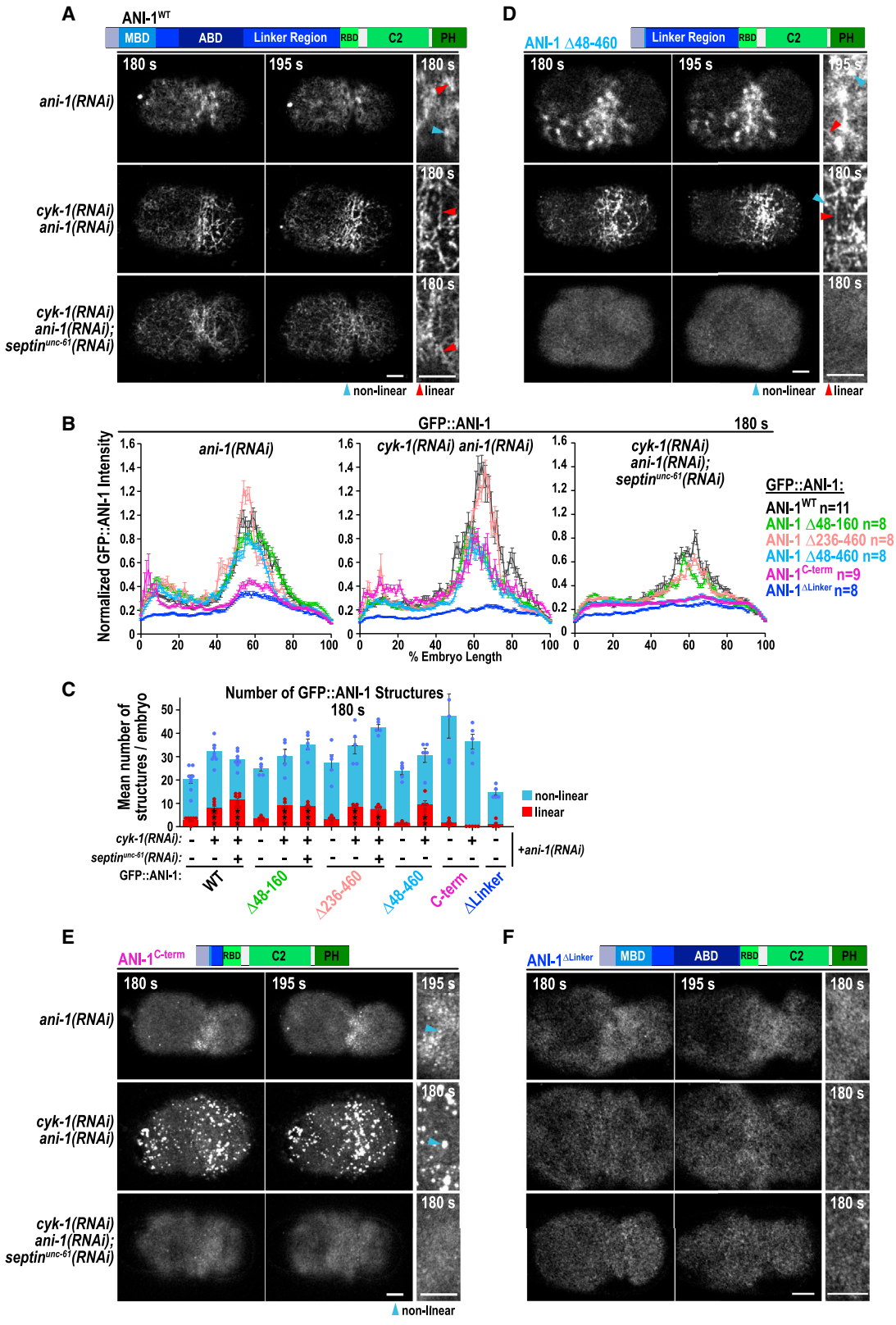

(legend on next page)

ANI-1$^{C\text{-}term}$ structures after co-depletion of CYK-1 and septin$^{UNC\text{-}61}$ suggests that their formation requires septin binding.

Finally, we asked whether deletion of the linker region from the full-length ANI-1 protein also abolished linear structure formation (Figure S8C). ANI-1$^{\Delta Linker}$ was expressed similar to ANI-1^{WT} and partially rescued embryonic lethality after *ani-1(RNAi)* (Figures S8E and S8F). Cortical equatorial levels of ANI-1$^{\Delta Linker}$ were reduced in comparison to the levels of ANI-1^{WT} after *ani-1(RNAi)* and almost no linear structures formed (Figures 5B, 5C, and 5F; Video S11), consistent with the observation that the absence of the linker in ANI-1$^{C\text{-}term}$ abolished linear structure formation. Depletion of CYK-1 or CYK-1 and septin$^{UNC\text{-}61}$ in the ANI-1$^{\Delta Linker}$ strain caused a further reduction in cortical ANI-1$^{\Delta Linker}$ levels, although pulsed accumulation was still visible (Figure 5F; Video S11). This contrasts with the ANI-1$^{C\text{-}term}$, which formed septin-dependent non-linear structures after *cyk-1(RNAi)* (Figures 5C, 5E, and 5F).

Together, the ANI-1 deletion analysis reveals that neither the predicted MBD nor the ABD are required for linear structure formation and that the linker region facilitates their formation.

The membrane-targeted ANI-1$^{N\text{-}term}$ is sufficient for linear structure formation

Since we observed that C-terminal ANI-1 half (ANI-1$^{C\text{-}term}$) is not sufficient for linear structure formation, we tested whether the N-terminal half is. The ANI-1$^{N\text{-}term}$, which comprises the putative MBD, the ABD, and the linker region, expressed well, partially rescued embryonic lethality, and weakly enriched at the cell equator after *ani-1(RNAi)* (Figures 6A–6C, S8C, S8E, and S8F). The ANI-1$^{N\text{-}term}$ formed some linear structures after depleting endogenous ANI-1; however, after CYK-1 or CYK-1 and septin$^{UNC\text{-}61}$ depletion, the cortical levels of ANI-1$^{N\text{-}term}$ were strongly diminished (Figures 6B–6D; Video S12) and therefore the structure analysis was not possible. To overcome this limitation, we targeted ANI-1$^{N\text{-}term}$ to the plasma membrane by fusing it with a membrane-targeting region (ANI-1$^{N\text{-}term\text{-}CX}$; Figure S8C). ANI-1$^{N\text{-}term\text{-}CX}$ was expressed similar to ANI-1^{WT} and rescued embryonic lethality more efficiently than the non-membrane-targeted ANI-1$^{N\text{-}term}$ (Figures S8E and S8F). The ANI-1$^{N\text{-}term\text{-}CX}$ fragment was enriched at the anterior cortex (Figures 6C and 6E; Video S13) and, therefore, we analyzed ANI-1$^{N\text{-}term\text{-}CX}$ structures not only at the equatorial but also at the anterior cortex. The ANI-1$^{N\text{-}term\text{-}CX}$ formed linear structures in all RNAi conditions at the anterior cortex and some, but less, at the cell equator (Figures 6D and 6E). To determine whether full actin depolymerization prevents linear structure formation, ANI-1$^{N\text{-}term\text{-}CX}$-expressing embryos were treated with Latrunculin A. Some linear ANI-1$^{N\text{-}term\text{-}CX}$ structures were still observed at late time points, although they were less defined than the ones formed by ANI-1^{WT} (Figures S9D and S9E; Video S10).

Since the N terminus permitted and its deletion abolished linear structure formation, we split the membrane-targeted N terminus into two fragments comprising the linker (ANI-1$^{Linker\text{-}CX}$) or the MBD-ABD (ANI-1$^{M\text{-}ABD\text{-}CX}$; Figure S8C). ANI-1$^{Linker\text{-}CX}$ and ANI-1$^{M\text{-}ABD\text{-}CX}$ were expressed comparable to ANI-1^{WT}; however, embryonic lethality caused by depleting endogenous ANI-1 was only marginally rescued by ANI-1$^{Linker\text{-}CX}$ and not by ANI-1$^{M\text{-}ABD\text{-}CX}$ (Figures S8E and S8F). The ANI-1$^{M\text{-}ABD\text{-}CX}$ fragment formed almost no linear structures and the ANI-1$^{Linker\text{-}CX}$ fragment made some linear structures, although they were less frequent than observed for the ANI-1$^{N\text{-}term\text{-}CX}$ (Figures 6D, 6F, and S9F; Video S14).

Together, the membrane-targeted ANI-1 N terminus is sufficient for linear structure formation and its linker region and the M-ABD region are both necessary to form them efficiently.

The ANI-1$^{N\text{-}term\text{-}CX}$ partially rescues furrow ingression in *cyk-1(RNAi);septin$^{unc\text{-}61}$(RNAi)* embryos

To investigate whether the different ANI-1 mutants support furrow ingression, we filmed embryos in the central plane. As expected, depletion of CYK-1 in ANI-1^{WT}-expressing embryos prevented furrow ingression and co-depletion of CYK-1 and septin$^{UNC\text{-}61}$ resulted in complete furrow ingression (Figures 7 and S10A). ANI-1 Δ48–160 and ANI-1 Δ236–460 rescued cleavage furrow ingression similar to ANI-1^{WT} (Figure 7), consistent with the fact that they formed linear structures. ANI-1 Δ48–460, ANI-1$^{C\text{-}term}$, ANI-1$^{N\text{-}term}$, and ANI-1$^{\Delta Linker}$ did not rescue furrow ingression, but, as they localized only weakly to the cortex, no rescue was expected (Figure S10). Similarly, the membrane-tethered ANI-1$^{Linker\text{-}CX}$ or ANI-1$^{M\text{-}ABD\text{-}CX}$ did not rescue furrow ingression, consistent with the observation that only a few or almost no linear structures were present, respectively (Figure S10B). Importantly, five out of eight embryos expressing ANI-1$^{N\text{-}term\text{-}CX}$ fully ingressed a cleavage furrow and, in two of those embryos, the cleavage furrow remained closed until the onset of the second cell division (Figure 7). This demonstrates that the N terminus of ANI-1, even though not being able to fully enrich at the cell equator, is able to partially rescue the cytokinesis failure in *cyk-1(RNAi) ani-1(RNAi);septin$^{unc\text{-}61}$(RNAi)* embryos.

DISCUSSION

In animal cells, the contractile ring consists of formin-nucleated unbranched F-actin, which circumferentially aligns around the cell equator. Myosin-dependent constriction of the contractile ring mediates cleavage furrow ingression.[93] Here we discover

Figure 5. The ANI-1 linker region facilitates linear structure formation

(A, D, E, and F) Representation of ANI-1 transgenes and confocal cortical images of GFP-tagged ANI-1 variants for indicated RNAi conditions and time points after NEBD. Magnifications of equatorial regions are shown (right). Non-linear (blue) and linear (red) structures are highlighted by arrowheads. To better visualize ANI-1$^{\Delta Linker}$ after *cyk-1(RNAi)ani-1(RNAi)* and all transgenes after septin$^{UNC\text{-}61}$ co-depletion, the signal intensity scaling was increased in those conditions. Scale bars, 5 μm.

(B) Mean normalized cortical fluorescence intensity of GFP-tagged ANI-1 variants for indicated RNAi conditions; n = number of embryos.

(C) Mean number of structures per embryo at the equator for different ANI-1 variants after RNAi depletions. The p values were calculated using Mann-Whitney U or Student's t test: $^{**}p < 0.01$ and $^{***}p < 0.001$ in comparison to *ani-1(RNAi)* embryos expressing the same transgene; dots represent data points of individual embryos. All error bars indicate SEM.

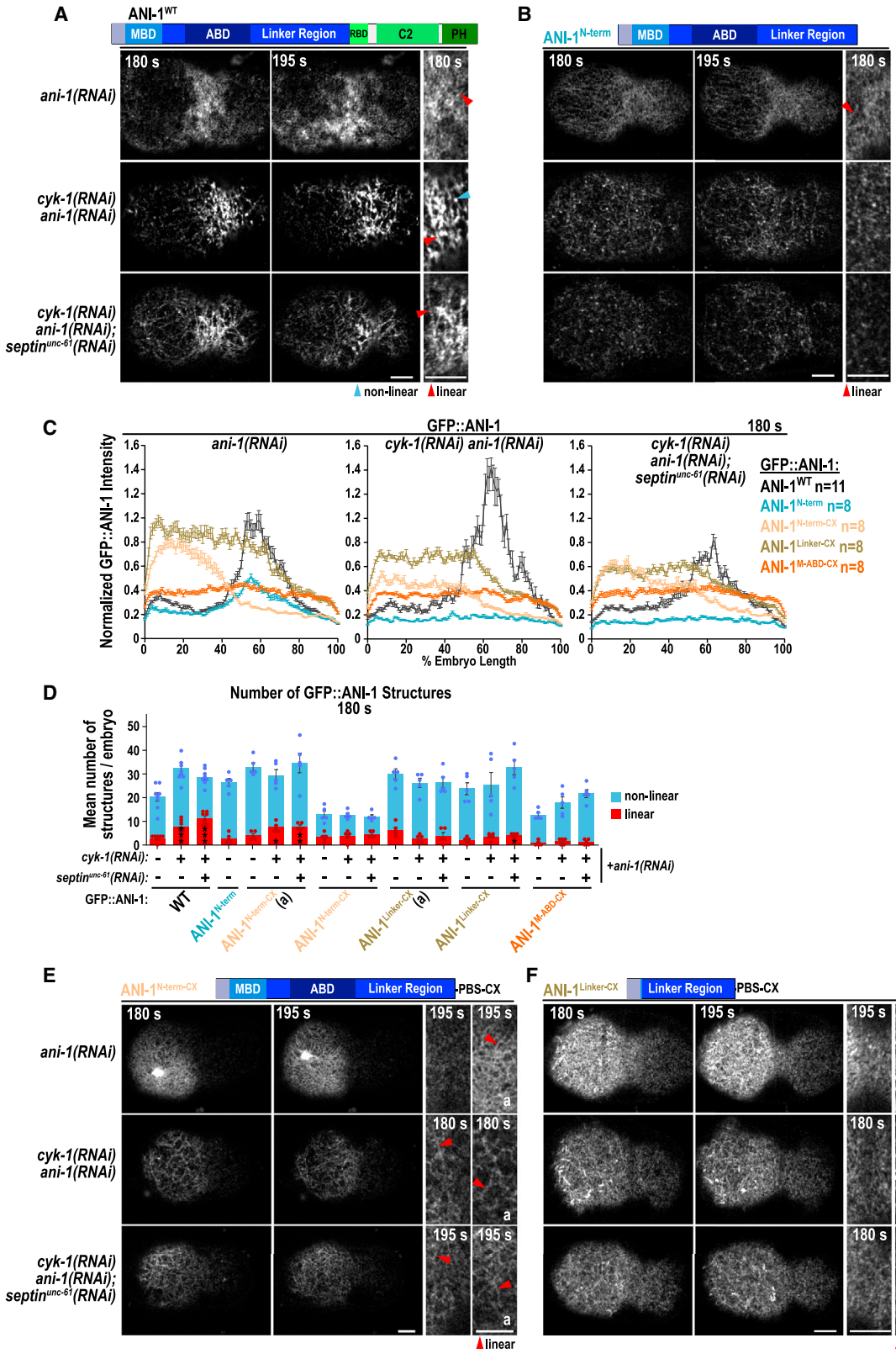

(legend on next page)

an ANI-1-dependent mechanism that promotes furrow ingression when the levels of formin-nucleated F-actin and septins are strongly reduced (Figure S11). We propose that, in this situation, active RhoA recruits ANI-1 and NMY-2 to the cell equator during anaphase. ANI-1 is tethered to the equatorial membrane by its C2 and RBD domain and NMY-2 directly binds lipids of the plasma membrane. The disordered ANI-1 N terminus extends into the cytoplasm, interacts with neighboring ANI-1 molecules, and forms linear structures that circumferentially align around the cell equator in an NMY-2-dependent manner. The linear ANI-1 structures together with the residual F-actin form a contractile ring that is decorated by NMY-2 and is able to constrict. The generated force is conveyed to the plasma membrane by membrane-bound ANI-1 and NMY-2 to form the cleavage furrow. Some linear ANI-1 structures are present in wild-type embryos and could also assist with furrow ingression by a similar mechanism in the presence of normal levels of formin-nucleated F-actin.

NMY-2 is an independent membrane anchor that links the actin cortex with the membrane

NMY-2 enriches in foci on the equatorial plasma membrane after F-actin depolymerization even in the absence of the ANI-1 N terminus. Furthermore, *in vitro* binding assays show that NMY-2, together with the RLC and ELC, interacts with multiple plasma membrane lipids. Together, our data suggest that NMY-2, after activation by RhoA signaling, binds the membrane directly. Membrane binding of myosin II seems conserved in other organisms as, in *Drosophila* cells, myosin also localizes to the membrane independently of anillin and F-actin.[33] In fission yeast, Mid1p targets Myo2 to the cytokinesis nodes during ring assembly[37,38] and, with the onset of ring constriction, Mid1p but not Myo2 leaves the division sites,[94] suggesting that Myo2 could bind the membrane independently of Mid1p. A previous study found that myosin II interacts with lipids through its RLC-binding site and lipid binding resulted in displacement of the RLC.[95] This implies that membrane-bound myosin II is in the inactive state, since the RLC is required for myosin II activity. In contrast, we observed that NMY-2 interacts with membrane lipids in the presence of the RLC and ELC, suggesting that NMY-2 can bind the membrane in its active state. Thus, in *C. elegans*, membrane-bound active NMY-2 might represent an independent membrane anchor that links the plasma membrane with the actin cortex and thereby could transmit forces generated in the contractile ring to the plasma membrane. NMY-2 membrane tethering might function redundantly with other membrane-binding components such as ECT2,[96] anillin,[48] and RacGAP1.[97]

Formation of linear ANI-1 structures is modulated by the amount of F-actin

We discover that ANI-1 localizes not only to cortical patches[34,70] but also to some linear structures during cytokinesis in the one-cell *C. elegans* embryo. After the reduction of formin-nucleated F-actin, numerous linear ANI-1 structures form and circumferentially align around the cell equator. How could F-actin limit the formation of linear ANI-1 structures? We speculate that, when unbranched F-actin levels are high, ANI-1 binds F-actin and distributes along the filaments, which limits contacts between ANI-1 molecules or restrains extension or flexibility of the disordered ANI-1 N terminus. When unbranched F-actin levels are low, such as in the case of CYK-1 depletion, ANI-1 N termini are free, accessible to self-interact and form linear structures. In the complete absence of F-actin, ANI-1^{WT}, and to some extent even ANI-1 Δ48–460 and ANI-1$^{N\text{-}term\text{-}CX}$, first forms circular structures that become linear at late anaphase time points. The delayed formation of linear ANI-1 structures in the absence of F-actin strongly suggests that the residual short actin filaments might bridge adjacent linear ANI-1 structures to accelerate the process. We did not observe a change in ANI-1 structure formation after the reduction of Arp2/3-generated branched F-actin, suggesting that ANI-1 preferentially binds CYK-1-nucleated unbranched F-actin.

Anillin binds septins, which can oligomerize into higher-order structures such as filaments.[64,98] Septins are required for the formation of filamentous anillin structures in Latrunculin A-treated *Drosophila* S2 cells.[33,52] Similarly, our data suggest that, in the absence of F-actin, septins facilitate linear structure formation of full-length ANI-1. However, a C-terminal ANI-1 fragment (ANI-1$^{AH\text{-}PH}$), which still harbors the septin binding PH domain, was insufficient for linear structure formation in the absence of F-actin, suggesting that linear structures form via the N terminus. Linear ANI-1 structures induced by *cyk-1(RNAi)* were not affected by septin$^{UNC\text{-}61}$ or septin$^{UNC\text{-}61}$ and septin$^{UNC\text{-}59}$ co-depletion, although cortical ANI-1 levels were clearly reduced. This shows that linear ANI-1 structures form efficiently after a strong reduction of both *C. elegans* septins as long as residual F-actin is present. Only in cases when F-actin is completely absent do septins facilitate linear structure formation. This suggests that the residual F-actin and septin support linear structure formation, probably stabilizing and/or bundling ANI-1. Although the septin depletion was highly efficient, we cannot entirely exclude a contribution of some remaining septin in linear ANI-1 structure formation, and future work will have to generate null mutations in both septin genes to test this.

Filamentous-type anillin was not only observed in Latrunculin A-treated *Drosophila* cells[33,52] but also along F-actin bundles

Figure 6. The membrane-targeted N-terminal half of ANI-1 is sufficient for linear structure formation

(A, B, E, and F) Representation of ANI-1 transgenes and cortical confocal images of GFP-tagged ANI-1 variants for indicated RNAi conditions and time points after NEBD. Magnifications of the cell equator and an anterior region (a) for ANI-1$^{N\text{-}term\text{-}CX}$ and ANI-1$^{Linker\text{-}CX}$ are displayed. Non-linear (blue) and linear (red) structures are highlighted by arrowheads. Scaling was increased for equator magnifications of ANI-1$^{N\text{-}term\text{-}CX}$ and ANI-1^{WT}, ANI-1$^{N\text{-}term}$, and ANI-1$^{N\text{-}term\text{-}CX}$ with septin$^{UNC\text{-}61}$ co-depletion, and for the latter two also for *cyk-1(RNAi)ani-1(RNAi)*. Scale bars, 5 μm.

(C) Mean normalized cortical fluorescence intensity of GFP-tagged ANI-1 variants for indicated RNAi treatments; n = number of embryos. ANI-1^{WT} graphs are reproduced from Figure 5B.

(D) Mean number of structures at the equatorial and anterior (a) cortex for the different ANI-1 variants after RNAi depletions. The p values were calculated using Mann-Whitney U or Student's t test: *$p < 0.05$, **$p < 0.01$, ***$p < 0.001$ in comparison to *ani-1(RNAi)* embryos expressing the same transgene; dots represent data points of individual embryos. ANI-1^{WT} graphs are reproduced from Figure 5C.

All error bars indicate SEM.

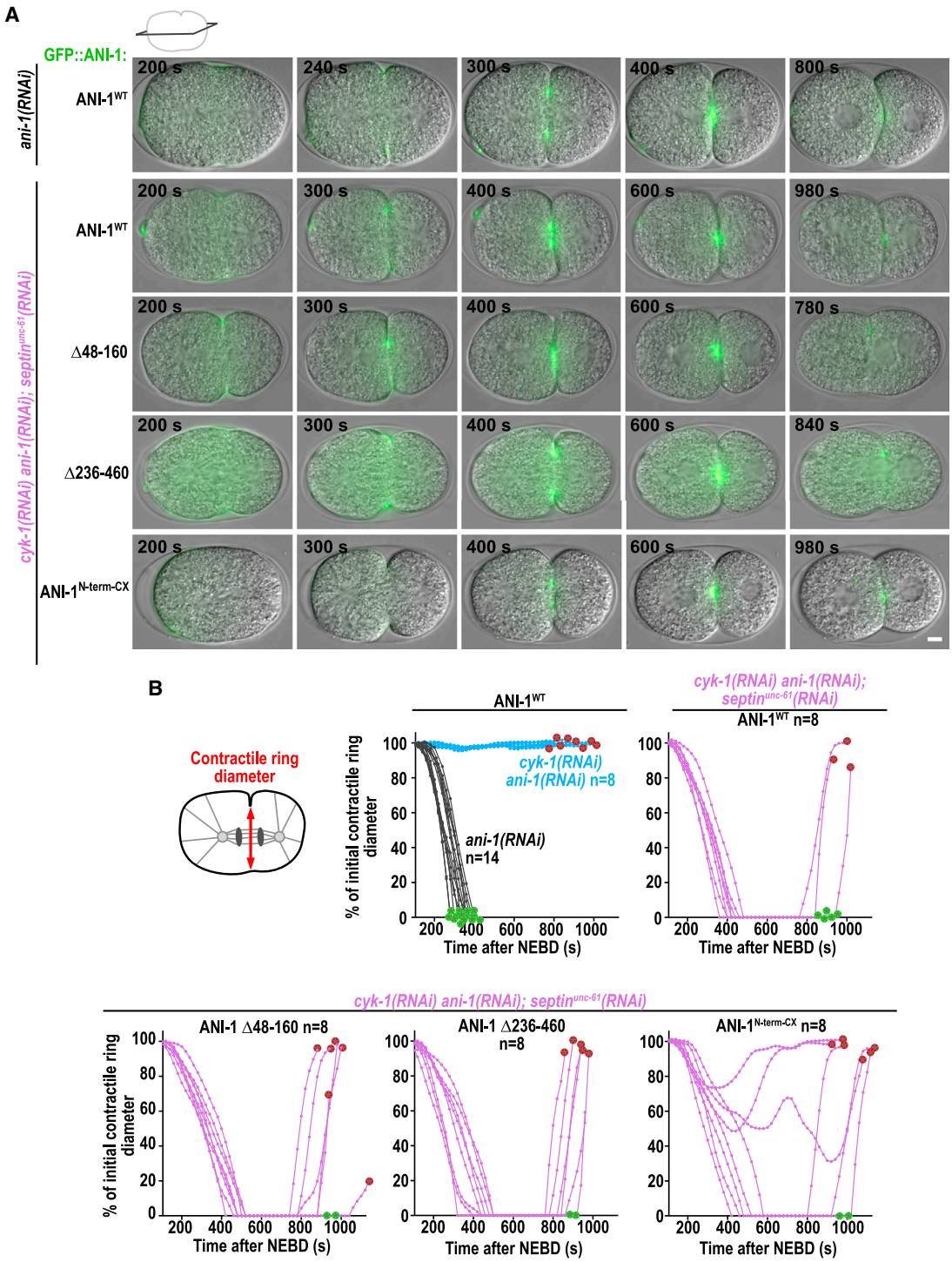

Figure 7. The membrane-targeted N-terminal ANI-1 fragment partially rescues furrow ingression in *cyk-1(RNAi)ani-1(RNAi);septin*$^{unc-61}$*(RNAi)*

(A) Merged differential interference contrast (DIC) and wide-field fluorescent central plane images for indicated GFP-tagged ANI-1 variants, RNAi conditions, and time points after NEBD. Scale bar, 5 μm.

(B) Plotted is the contractile ring diameter for indicated RNAi conditions and ANI-1 variants; n = number of embryos. Green and red encircled stars indicate whether embryos succeed or fail cytokinesis, respectively.

in unperturbed vertebrate cells[49] after myosin II inhibition.[53] Thus, the competence of anillin to form linear structures may be a conserved feature from worms to humans.

The C-terminal half of ANI-1 concentrates at the cell equator in septin-dependent circular structures

Anillin's C-terminal half harbors three membrane interaction elements: the RBD, the C2, and the PH domain, and each of them contributes to membrane localization of anillin in human cells.[46–48] Importantly, the ANI-1 C-terminal half forms circular and not linear structures in *cyk-1(RNAi)* and Latrunculin A-treated embryos. The localization of the ANI-1$^{C\text{-}term}$ to the circular structures strongly depends on septins, thus *C. elegans* ANI-1, similar to anillin in other organisms, should bind to septins via the PH domain.[46,48,49,86]

Human anillin binds septins not only directly with the PH domain but also indirectly via CIN85 with amino acids 1–150 at its very N terminus.[85] Thus it is possible that ANI-1 has a second septin-binding site at its very N-terminal end. We found that removal of amino acids 48–160 from ANI-1 did not prevent linear structure formation or furrow ingression after CYK-1 and septin co-depletion. Further, the presence of amino acids 1–48 in the ANI-1$^{C\text{-}term}$ fragment and amino acids 1–459 in the ANI-1$^{M\text{-}ABD\text{-}CX}$ fragment was not sufficient for linear structure formation. Together, indirect septin binding of ANI-1 via its very N terminus is either not conserved in *C. elegans* or is not essential for the process studied here.

Since ANI-1 is reduced after septin depletion and septin recruitment to the contractile ring entirely depends on ANI-1,[34,48] ANI-1 and septin stabilize each other on the plasma membrane.

After septin and CYK-1 co-depletion, a residual pulsatile membrane localization of ANI-1$^{C\text{-}term}$, ANI-1 Δ48–460, and ANI-1$^{\Delta Linker}$ persisted. This could reflect direct binding to the plasma membrane and/or binding to active RhoA. Given that the ANI-1$^{C\text{-}term}$ membrane localization strongly depends on septins, changes in ANI-1$^{C\text{-}term}$ dynamics cannot be exclusively attributed to active RhoA dynamics. Therefore, employing the ANI-1$^{C\text{-}term}$ as a biosensor for active RhoA[22,35,89] should be done with caution.

The disordered ANI-1 N terminus is sufficient for linear structure formation

The membrane-targeted N-terminal ANI-1 half localized in linear structures. Further, our mutant analysis of full-length ANI-1 revealed that neither the MBD nor the ABD nor both domains together are required for ANI-1 linear structure formation in control and *cyk-1(RNAi)* embryos. Only further shortening of ANI-1 by removal of the linker region prevented the formation of linear structures, and circular septin-dependent foci formed instead. Splitting the N-terminal ANI-1 half revealed that the linker region formed a few and the M-ABD no linear structures, indicating that both regions contribute to efficient linear structure formation when tethered to the membrane. Since the linker region of ANI-1 was sufficient for linear structures formation when bound to the membrane by the ANI-1 C terminus (ANI-1$^{\Delta 48\text{-}460}$), it suggests that the employed membrane anchor might not mimic all necessary functional features such as enrichment in certain lipids domains[48] and/or the correct distance from the membrane. Nevertheless, the membrane-targeted N-terminal fragment rescued embryonic lethality more efficiently than the non-targeted version, demonstrating that membrane binding of the Nterminus improves its functionality. Deletion of the linker region from full-length ANI-1 reduced linear structures after *ani-1(RNAi)*, supporting our conclusion that the linker is a key region to form them. Unfortunately, deletion of the linker appears to compromise the function of both the M-ABD and the Cterminus, since the ANI-1$^{\Delta Linker}$ mutant is more lethal than the ANI-1$^{C\text{-}term}$ mutant, which lacks the entire N terminus, including the linker region. In addition, the ANI-1$^{\Delta Linker}$ forms no circular septin-dependent structures after *cyk-1(RNAi)*, although it contains the PH domain. We therefore speculate that the M-ABD and C terminus bind each other in the ANI-1$^{\Delta Linker}$ mutant and thereby block each other's function.

Since the N terminus of Mid1p forms high-molecular-weight oligomers,[99] one possibility is that the ANI-1 N terminus assembles into linear structures by self-interaction-mediated oligomerization. Furthermore, liquid-liquid phase separation mechanisms might drive the formation of linear ANI-1 structures. Our structure prediction reveals that the N terminus of ANI-1 is highly disordered but the Cterminus is not. This feature of ANI-1 is conserved from fission yeast[92] to worms and humans. Disordered regions frequently mediate the formation of biomolecular condensates by liquid-liquid phase separation,[100] and indeed the disordered N terminus of Mid1p forms condensates *in vitro*.[92] Liquid droplets are typically isotropic but their shape and material properties are tunable in multiple ways.[101] For example, isotropic liquid condensates of fused in sarcoma (FUS) transform into spindle-shaped condensates when F-actin is incorporated in the droplets.[102] We speculate that linear ANI-1 structures could form by similar principles: the isotropic spherical shape of the biomolecular ANI-1 condensates is biased to an extended anisotropic form by additional factors such as remaining F-actin polymers or posttranslational modifications of ANI-1.

The ANI-1 N terminus promotes furrow ingression after co-depletion of formin and septins

After CYK-1 depletion, ANI-1 forms linear structures and, at the same time, cortical septin$^{UNC\text{-}59}$ levels increase. The reduction in F-actin levels after *cyk-1(RNAi)* might increase the free pool of ANI-1, which then binds and stabilizes septin and thereby causes an elevation in cortical septin levels. Septins or the excess thereof could then tether ANI-1 tightly to the membrane and thereby hinder cleavage furrow ingression in CYK-1-depleted embryos. A reduction in septin levels might weaken the interaction between ANI-1 and the plasma membrane and consequently lead to increased mobility of ANI-1 on the membrane, which could facilitate the interaction between ANI-1 molecules and the binding of ANI-1 to NMY-2 and the residual F-actin. All *cyk-1(RNAi);septin$^{unc\text{-}61}$(RNAi)* embryos fully ingress a cleavage furrow, but half of them fail in abscission and the furrow regresses. Septins are essential for abscission in *Drosophila* and human cells[65,68] but not in *C. elegans* embryos.[67] Thus, our data indicate a functional redundancy between unbranched F-actin and septins during abscission in *C. elegans*.

Our data suggest that the N terminus of ANI-1 interacts with NMY-2, since co-localization of NMY-2 and ANI-1 after Latrunculin A treatment requires its presence. Consistent with that, NMY-2 was required for the circumferential alignment of the linear ANI-1 structures. Surprisingly, deletion of the putative MBD did not abrogate linear ANI-1 structure alignment. Thus, either the NMY-2 binding region is not properly predicted or NMY-2 does not align ANI-1 via direct binding. Since CYK-1-depleted embryos only exhibit short-range cortical flows,[103] the alignment of the linear ANI-1 structures around the cell equator is unlikely to be flow dependent, as suggested for unbranched F-actin.[22] Therefore, we favor alternative models where localized motor activity of NMY-2 and crosslinkers promotes equatorial circumferential alignment.[23]

Furrow ingression in CYK-1 and septin-depleted embryos required residual F-actin, NMY-2, and ANI-1. Furthermore, furrow ingression was only supported by ANI-1 fragments that formed linear structures and that circumferentially aligned around the cell equator, similar to unbranched F-actin in control embryos. Therefore, it is tempting to speculate that those ANI-1 structures have a prominent role in furrowing in septin and CYK-1 co-depleted embryos. Although CYK-1 depletion was highly efficient, residual CYK-1 could generate some actin filaments at the cell equator. Additionally, actin filaments could be polymerized at the polar cortex and transported to the equator by equatorial-directed cortical flows.[104] However, we consider flow-mediated actin transport unlikely since cortical flows are compromised in *cyk-1(RNAi)* embryos[103] and actin filament turnover is typically too high for efficient long-range transport.[105] Even though those mechanisms might result in some F-actin at the cell equator, we and others could not detect equatorial F-actin enrichment.[79,81–83]

It is known that several anillin homologs, including *C. elegans* ANI-1, bind and bundle F-actin.[50,55,56] Human anillin even mediates the formation of actin rings from actin filaments *in vitro*.[63] Thus, the circumferentially aligned linear ANI-1 structures could organize the few remaining actin filaments into a stable equatorial ring by providing a scaffold and by bridging the residual actin filaments. Although it has been reported that ANI-1-induced actin rings can contract in the absence of myosin *in vitro*,[63] ANI-1 rings formed *in vivo* after co-depletion of CYK-1 and septins do require NMY-2 for constriction. Anillin organizes NMY-2 into cortical patches in the *C. elegans* zygote,[34] stabilizes myosin II in the contractile ring, and interacts with NMY-2.[33,46,53] Therefore, ANI-1 could mediate the higher-order organization of NMY-2, stabilize NMY-2 in the furrow region, and bring NMY-2 in close proximity to residual F-actin so that it can generate force as a motor or tension as an F-actin crosslinker, similar to what happens in normal contractile rings.[93]

However, since detectable F-actin did not accumulate at the equator after CYK-1 and septin co-depletion and the ABD of ANI-1 was not required for furrow ingression, we favor an alternative explanation. We hypothesize that linear ANI-1 structures represent a novel type of network that contracts by biomolecular condensation. ANI-1 is predicted to have numerous IDRs at the N terminus, and we showed that the Nterminus is sufficient for linear structure formation and furrow ingression. IDRs are frequently found in proteins that form biomolecular condensates by liquid-liquid phase separation. Recent reports demonstrate that biomolecular condensation can also exert forces on cellular structures and alter the shape of membranes.[106–108] For example, the formation of biomolecular condensates of FUS on the surface of membrane vesicles generates compressive stress and causes inward membrane bending.[109] We speculate that condensation of linear ANI-1 structures results in the contraction of the ANI-1 network and ultimately in the inward bending of the plasma membrane (Figure S11). The contractile force generated by ANI-1 condensation is then propagated around the ANI-1 network by NMY-2 filaments, which bind and crosslink the ANI-1 linear structures. As a first step, future work will need to show that *C. elegans* ANI-1, like Mid1p from fission yeast,[92] also undergoes liquid-liquid phase separation. Linear ANI-1 structures are also observed in wild-type embryos that have normal F-actin levels. So, it is possible that ANI-1 linear structures may assist with furrow ingression in a normal situation and take over the process when unbranched F-actin levels are reduced.

In summary, we find that ANI-1 forms linear structures and supports furrow ingression when unbranched F-actin levels are low. Although actomyosin-dependent constriction is the most actively investigated mechanism for cytokinetic furrowing, alternative ways have been reported to exist. For example, furrow ingression is mediated in *Dictyostelium* and human RPE1 by the opposite migration direction of the two daughter cells[75–77] and in archaea by supercoiling of the elastic ESCRT-III filament.[110,111] Our findings highlight the existence of a compensatory mechanism of cleavage furrow ingression that is likely to contribute to the enormous robustness of cytokinesis.

Limitations of the study

The study employs RNAi-mediated protein depletions to analyze the function of various cytokinesis regulators. Although the study shows that the RNAi depletions are highly efficient, it cannot be excluded that residual amounts of proteins contribute to the processes. In addition, the condensation-based model of ring constriction is based on the prediction that ANI-1 undergoes liquid-liquid phase separation, which still must be demonstrated for *C. elegans* ANI-1.

STAR★METHODS

Detailed methods are provided in the online version of this paper and include the following:

- KEY RESOURCES TABLE
- RESOURCE AVAILABILITY
  - Lead contact
  - Materials availability
  - Data and code availability
- EXPERIMENTAL MODEL AND SUBJECT DETAILS
- METHOD DETAILS
  - Embryonic lethality counts
  - Immunoblotting
  - Mos1-mediated single copy insertion (MosSCI) of ANI-1 variants
  - Fluorescence microscopy and image analysis

- Latrunculin A treatment
- 6xHIS::NMY-2 cloning and NMY-2/MLC-4/MLC-5 protein expression
- PIP strips and immunoblotting

- QUANTIFICATION AND STATISTICAL ANALYSIS

SUPPLEMENTAL INFORMATION

Supplemental information can be found online at https://doi.org/10.1016/j.celrep.2023.113076.

ACKNOWLEDGMENTS

We are grateful to Christin Nöcker, Maysoon Noureddine, Suraj Shaji, and Isabel Schultz-Pernice for helping with experiments. Microscopy was performed either at the Center for Advanced Light Microscopy (CALM, Ludwig-Maximilians-Universität München) or at the Optical Imaging Center Erlangen (OICE, Friedrich-Alexander-Universität Erlangen-Nürnberg). We are grateful to Christof Osman for access to the Nikon Ti2-Eclipse microscope. For critical comments on the manuscript, we thank Friederike Wolff and Sabine Müller. The Deutsche Forschungsgemeinschaft supported E. Zanin (ZA619/3, 265449562), T. Mikeladze-Dvali (MI1867/1-3), and the Leica SP8 DIVE-FALCON (INST90/1074-1 FUGG for Benedikt Kost). A.-X.C. was supported by the European Research Council under the European Union's Horizon 2020 Research and Innovation Programme (640553–ACTOMYO) and by a Principal Investigator position from the Portuguese Foundation for Science and Technology (FCT) (CEECIND/01967/2017). F-Y.C. has an FCT junior researcher position (DL 57/2016/CP1355/CT0013). J.B. and E.R. were members of the Life Science Munich graduate program. For *C. elegans* strains, we thank Amy Maddox, Stephan Grill, and Zhirong Bao and the CGC, which is funded by NIH Office of Research Infrastructure Programs (P40 OD010440).

AUTHOR CONTRIBUTIONS

Conceptualization, E.Z., T.M.-D., and A.X.C.; methodology, E.Z., A.X.C., M.L., and F.Y.C.; investigation, M.L., F.Y.C., A.L., J.B., D.S.O., and E.R.; formal analysis, M.L.; writing – original draft, E.Z.; writing – review & editing, E.Z., T.M.-D., and A.X.C.; visualization, E.Z., funding acquisition, E.Z., T.M.-D., F.Y.C., and A.X.C.; supervision, E.Z., T.M.-D., and A.X.C.

DECLARATION OF INTERESTS

The authors declare no competing interests.

INCLUSION AND DIVERSITY

We support inclusive, diverse, and equitable conduct of research. While citing references scientifically relevant for this work, we also actively worked to promote gender balance in our reference list.

Received: December 24, 2022
Revised: July 13, 2023
Accepted: August 16, 2023
Published: September 3, 2023

REFERENCES

1. Mishima, M. (2016). Centralspindlin in Rappaport's cleavage signaling. Semin. Cell Dev. Biol. *53*, 45–56. https://doi.org/10.1016/j.semcdb.2016.03.006.
2. D'Avino, P.P., Giansanti, M.G., and Petronczki, M. (2015). Cytokinesis in animal cells. Cold Spring Harb. Perspect. Biol. *7*, a015834. https://doi.org/10.1101/cshperspect.a015834.
3. Pollard, T.D., and O'Shaughnessy, B. (2019). Molecular Mechanism of Cytokinesis. Annu. Rev. Biochem. *88*, 661–689. https://doi.org/10.1146/annurev-biochem-062917-012530.
4. Mangal, S., Sacher, J., Kim, T., Osório, D.S., Motegi, F., Carvalho, A.X., Oegema, K., and Zanin, E. (2018). TPXL-1 activates Aurora A to clear contractile ring components from the polar cortex during cytokinesis. J. Cell Biol. *217*, 837–848. https://doi.org/10.1083/jcb.201706021.
5. Zanin, E., Desai, A., Poser, I., Toyoda, Y., Andree, C., Moebius, C., Bickle, M., Conradt, B., Piekny, A., and Oegema, K. (2013). A conserved RhoGAP limits M phase contractility and coordinates with microtubule asters to confine RhoA during cytokinesis. Dev. Cell *26*, 496–510. https://doi.org/10.1016/j.devcel.2013.08.005.
6. Schneid, S., Wolff, F., Buchner, K., Bertram, N., Baygün, S., Barbosa, P., Mangal, S., and Zanin, E. (2021). The BRCT domains of ECT2 have distinct functions during cytokinesis. Cell Rep. *34*, 108805. https://doi.org/10.1016/j.celrep.2021.108805.
7. Dechant, R., and Glotzer, M. (2003). Centrosome separation and central spindle assembly act in redundant pathways that regulate microtubule density and trigger cleavage furrow formation. Dev. Cell *4*, 333–344.
8. Yüce, O., Piekny, A., and Glotzer, M. (2005). An ECT2-centralspindlin complex regulates the localization and function of RhoA. J. Cell Biol. *170*, 571–582. https://doi.org/10.1083/jcb.200501097.
9. Basant, A., and Glotzer, M. (2018). Spatiotemporal Regulation of RhoA during Cytokinesis. Curr. Biol. *28*, R570–R580. https://doi.org/10.1016/j.cub.2018.03.045.
10. Gomez-Cavazos, J.S., Lee, K.-Y., Lara-Gonzalez, P., Li, Y., Desai, A., Shiau, A.K., and Oegema, K. (2020). A Non-canonical BRCT-Phosphopeptide Recognition Mechanism Underlies RhoA Activation in Cytokinesis. Curr. Biol., 1–27. https://doi.org/10.1016/j.cub.2020.05.090.
11. Prokopenko, S.N., Brumby, A., O'Keefe, L., Prior, L., He, Y., Saint, R., and Bellen, H.J. (1999). A putative exchange factor for Rho1 GTPase is required for initiation of cytokinesis in Drosophila. Genes Dev. *13*, 2301–2314. https://doi.org/10.1101/gad.13.17.2301.
12. Chen, A., Arora, P.D., Lai, C.C., Copeland, J.W., Moraes, T.F., McCulloch, C.A., Lavoie, B.D., and Wilde, A. (2020). The scaffold-protein IQGAP1 enhances and spatially restricts the actin-nucleating activity of Diaphanous-related formin 1 (DIAPH1). J. Biol. Chem. *295*, 3134–3147. https://doi.org/10.1074/jbc.RA119.010476.
13. Chen, A., Arora, P.D., McCulloch, C.A., and Wilde, A. (2017). Cytokinesis requires localized β-actin filament production by an actin isoform specific nucleator. Nat. Commun. *8*, 1530. https://doi.org/10.1038/s41467-017-01231-x.
14. Otomo, T., Otomo, C., Tomchick, D.R., Machius, M., and Rosen, M.K. (2005). Structural Basis of Rho GTPase-Mediated Activation of the Formin mDia1. Mol. Cell *18*, 273–281. https://doi.org/10.1016/j.molcel.2005.04.002.
15. Li, F., and Higgs, H.N. (2003). The mouse Formin mDia1 is a potent actin nucleation factor regulated by autoinhibition. Curr. Biol. *13*, 1335–1340. https://doi.org/10.1016/s0960-9822(03)00540-2.
16. Piekny, A.J., and Maddox, A.S. (2010). The myriad roles of Anillin during cytokinesis. Semin. Cell Dev. Biol. *21*, 881–891. https://doi.org/10.1016/j.semcdb.2010.08.002.
17. Naydenov, N.G., Koblinski, J.E., and Ivanov, A.I. (2021). Anillin is an emerging regulator of tumorigenesis, acting as a cortical cytoskeletal scaffold and a nuclear modulator of cancer cell differentiation. Cell. Mol. Life Sci. *78*, 621–633. https://doi.org/10.1007/s00018-020-03605-9.
18. Kühn, S., and Geyer, M. (2014). Formins as effector proteins of Rho GTPases. Small GTPases *5*, e29513. https://doi.org/10.4161/sgtp.29513.
19. Schroeder, T.E. (1968). Cytokinesis: filaments in the cleavage furrow. Exp. Cell Res. *53*, 272–276.

20. Henson, J.H., Ditzler, C.E., Germain, A., Irwin, P.M., Vogt, E.T., Yang, S., Wu, X., and Shuster, C.B. (2017). The organization of actin and myosin II filaments in the contractile ring: new support for an old model of cytokinesis. Mol. Biol. Cell *28*, 613–623. https://doi.org/10.1091/mbc.E16-06-0466.

21. Spira, F., Cuylen-Haering, S., Mehta, S., Samwer, M., Reversat, A., Verma, A., Oldenbourg, R., Sixt, M., and Gerlich, D.W. (2017). Cytokinesis in vertebrate cells initiates by contraction of an equatorial actomyosin network composed of randomly oriented filaments. Elife *6*, e30867. https://doi.org/10.7554/eLife.30867.

22. Reymann, A.-C., Staniscia, F., Erzberger, A., Salbreux, G., and Grill, S.W. (2016). Cortical flow aligns actin filaments to form a furrow. Elife *5*, e17807. https://doi.org/10.7554/eLife.17807.

23. Leite, J., Chan, F.Y., Osório, D.S., Saramago, J., Sobral, A.F., Silva, A.M., Gassmann, R., and Carvalho, A.X. (2020). Equatorial Non-muscle Myosin II and Plastin Cooperate to Align and Compact F-actin Bundles in the Cytokinetic Ring. Front. Cell Dev. Biol. *8*, 573393. https://doi.org/10.3389/fcell.2020.573393.

24. Swan, K.A., Severson, A.F., Carter, J.C., Martin, P.R., Schnabel, H., Schnabel, R., and Bowerman, B. (1998). cyk-1: a C. elegans FH gene required for a late step in embryonic cytokinesis. J. Cell Sci. *111*, 2017–2027. https://doi.org/10.1242/jcs.111.14.2017.

25. Severson, A.F., Baillie, D.L., and Bowerman, B. (2002). A Formin Homology protein and a profilin are required for cytokinesis and Arp2/3-independent assembly of cortical microfilaments in C. elegans. Curr. Biol. *12*, 2066–2075. https://doi.org/10.1016/s0960-9822(02)01355-6.

26. Pelham, R.J., and Chang, F. (2002). Actin dynamics in the contractile ring during cytokinesis in fission yeast. Nature *419*, 82–86. https://doi.org/10.1038/nature00999.

27. Watanabe, S., Ando, Y., Yasuda, S., Hosoya, H., Watanabe, N., Ishizaki, T., and Narumiya, S. (2008). mDia2 induces the actin scaffold for the contractile ring and stabilizes its position during cytokinesis in NIH 3T3 cells. Mol. Biol. Cell *19*, 2328–2338. https://doi.org/10.1091/mbc.E07-10-1086.

28. Straight, A.F., Cheung, A., Limouze, J., Chen, I., Westwood, N.J., Sellers, J.R., and Mitchison, T.J. (2003). Dissecting temporal and spatial control of cytokinesis with a myosin II Inhibitor. Science *299*, 1743–1747. https://doi.org/10.1126/science.1081412.

29. De Lozanne, A., and Spudich, J.A. (1987). Disruption of the Dictyostelium myosin heavy chain gene by homologous recombination. Science *236*, 1086–1091. https://doi.org/10.1126/science.3576222.

30. Cuenca, A.A., Schetter, A., Aceto, D., Kemphues, K., and Seydoux, G. (2003). Polarization of the C. elegans zygote proceeds via distinct establishment and maintenance phases. Development *130*, 1255–1265. https://doi.org/10.1242/dev.00284.

31. Pollard, T.D. (2020). Myosins in Cytokinesis. Adv. Exp. Med. Biol. *1239*, 233–244. https://doi.org/10.1007/978-3-030-38062-5_11.

32. Khaliullin, R.N., Green, R.A., Shi, L.Z., Gomez-Cavazos, J.S., Berns, M.W., Desai, A., and Oegema, K. (2018). A positive-feedback-based mechanism for constriction rate acceleration during cytokinesis in Caenorhabditis elegans. Elife *7*, e36073. https://doi.org/10.7554/eLife.36073.

33. Hickson, G.R.X., and O'Farrell, P.H. (2008). Rho-dependent control of anillin behavior during cytokinesis. J. Cell Biol. *180*, 285–294. https://doi.org/10.1083/jcb.200709005.

34. Maddox, A.S., Habermann, B., Desai, A., and Oegema, K. (2005). Distinct roles for two C. elegans anillins in the gonad and early embryo. Development *132*, 2837–2848. https://doi.org/10.1242/dev.01828.

35. Tse, Y.C., Piekny, A., and Glotzer, M. (2011). Anillin promotes astral microtubule-directed cortical myosin polarization. Mol. Biol. Cell *22*, 3165–3175. https://doi.org/10.1091/mbc.E11-05-0399.

36. Davies, T., Jordan, S.N., Chand, V., Sees, J.A., Laband, K., Carvalho, A.X., Shirasu-Hiza, M., Kovar, D.R., Dumont, J., and Canman, J.C. (2014). High-Resolution Temporal Analysis Reveals a Functional Timeline for the Molecular Regulation of Cytokinesis. Dev. Cell *30*, 209–223. https://doi.org/10.1016/j.devcel.2014.05.009.

37. Motegi, F., Mishra, M., Balasubramanian, M.K., and Mabuchi, I. (2004). Myosin-II reorganization during mitosis is controlled temporally by its dephosphorylation and spatially by Mid1 in fission yeast. J. Cell Biol. *165*, 685–695. https://doi.org/10.1083/jcb.200402097.

38. Saha, S., and Pollard, T.D. (2012). Anillin-related protein Mid1p coordinates the assembly of the cytokinetic contractile ring in fission yeast. Mol. Biol. Cell *23*, 3982–3992. https://doi.org/10.1091/mbc.E12-07-0535.

39. Willet, A.H., McDonald, N.A., Bohnert, K.A., Baird, M.A., Allen, J.R., Davidson, M.W., and Gould, K.L. (2015). The F-BAR Cdc15 promotes contractile ring formation through the direct recruitment of the formin Cdc12. J. Cell Biol. *208*, 391–399. https://doi.org/10.1083/jcb.201411097.

40. Laplante, C., Huang, F., Tebbs, I.R., Bewersdorf, J., and Pollard, T.D. (2016). Molecular organization of cytokinesis nodes and contractile rings by super-resolution fluorescence microscopy of live fission yeast. Proc. Natl. Acad. Sci. USA *113*, E5876–E5885. https://doi.org/10.1073/pnas.1608252113.

41. Laporte, D., Coffman, V.C., Lee, I.J., and Wu, J.Q. (2011). Assembly and architecture of precursor nodes during fission yeast cytokinesis. J. Cell Biol. *192*, 1005–1021. https://doi.org/10.1083/jcb.201008171.

42. McDonald, N.A., Lind, A.L., Smith, S.E., Li, R., and Gould, K.L. (2017). Nanoscale architecture of the Schizosaccharomyces pombe contractile ring. Elife *6*, e28865. https://doi.org/10.7554/eLife.28865.

43. Vavylonis, D., Wu, J.-Q., Hao, S., O'Shaughnessy, B., and Pollard, T.D. (2008). Assembly mechanism of the contractile ring for cytokinesis by fission yeast. Science *319*, 97–100. https://doi.org/10.1126/science.1151086.

44. van Oostende Triplet, C., Jaramillo Garcia, M., Haji Bik, H., Beaudet, D., and Piekny, A. (2014). Anillin interacts with microtubules and is part of the astral pathway that defines cortical domains. J. Cell Sci. *127*, 3699–3710. https://doi.org/10.1242/jcs.147504.

45. Beaudet, D., Pham, N., Skaik, N., and Piekny, A. (2020). Importin binding mediates the intramolecular regulation of anillin during cytokinesis. Mol. Biol. Cell *31*, 1124–1139. https://doi.org/10.1091/mbc.E20-01-0006.

46. Piekny, A.J., and Glotzer, M. (2008). Anillin is a scaffold protein that links RhoA, actin, and myosin during cytokinesis. Curr. Biol. *18*, 30–36. https://doi.org/10.1016/j.cub.2007.11.068.

47. Sun, L., Guan, R., Lee, I.-J., Liu, Y., Chen, M., Wang, J., Wu, J.-Q., and Chen, Z. (2015). Mechanistic Insights into the Anchorage of the Contractile Ring by Anillin and Mid1. Dev. Cell *33*, 413–426. https://doi.org/10.1016/j.devcel.2015.03.003.

48. Liu, J., Fairn, G.D., Ceccarelli, D.F., Sicheri, F., and Wilde, A. (2012). Cleavage Furrow Organization Requires PIP2-Mediated Recruitment of Anillin. Curr. Biol. *22*, 64–69. https://doi.org/10.1016/j.cub.2011.11.040.

49. Oegema, K., Savoian, M.S., Mitchison, T.J., and Field, C.M. (2000). Functional analysis of a human homologue of the Drosophila actin binding protein anillin suggests a role in cytokinesis. J. Cell Biol. *150*, 539–552.

50. Field, C.M., Coughlin, M., Doberstein, S., Marty, T., and Sullivan, W. (2005). Characterization of anillin mutants reveals essential roles in septin localization and plasma membrane integrity. Development *132*, 2849–2860. https://doi.org/10.1242/dev.01843.

51. El Amine, N., Kechad, A., Jananji, S., and Hickson, G.R.X. (2013). Opposing actions of septins and Sticky on Anillin promote the transition from contractile to midbody ring. J. Cell Biol. *203*, 487–504. https://doi.org/10.1083/jcb.201305053.

52. Carim, S.C., and Hickson, G.R.X. (2023). The Rho1 GTPase controls anillo-septin assembly to facilitate contractile ring closure during cytokinesis. iScience *26*, 106903. https://doi.org/10.1016/j.isci.2023.106903.

53. Straight, A.F., Field, C.M., and Mitchison, T.J. (2005). Anillin binds nonmuscle myosin II and regulates the contractile ring. Mol. Biol. Cell *16*, 193–201. https://doi.org/10.1091/mbc.E04-08-0758.

54. Field, C.M., and Alberts, B.M. (1995). Anillin, a contractile ring protein that cycles from the nucleus to the cell cortex. J. Cell Biol. *131*, 165–178. https://doi.org/10.1083/jcb.131.1.165.

55. Tian, D., Diao, M., Jiang, Y., Sun, L., Zhang, Y., Chen, Z., Huang, S., and Ou, G. (2015). Anillin Regulates Neuronal Migration and Neurite Growth by Linking RhoG to the Actin Cytoskeleton. Curr. Biol. *25*, 1135–1145. https://doi.org/10.1016/j.cub.2015.02.072.

56. Jananji, S., Risi, C., Lindamulage, I.K.S., Picard, L.-P., Van Sciver, R., Laflamme, G., Albaghjati, A., Hickson, G.R.X., Kwok, B.H., and Galkin, V.E. (2017). Multimodal and Polymorphic Interactions between Anillin and Actin: Their Implications for Cytokinesis. J. Mol. Biol. *429*, 715–731. https://doi.org/10.1016/j.jmb.2017.01.020.

57. Matsuda, K., Sugawa, M., Yamagishi, M., Kodera, N., and Yajima, J. (2020). Visualizing dynamic actin cross-linking processes driven by the actin-binding protein anillin. FEBS Lett. *594*, 1237–1247. https://doi.org/10.1002/1873-3468.13720.

58. Watanabe, S., Okawa, K., Miki, T., Sakamoto, S., Morinaga, T., Segawa, K., Arakawa, T., Kinoshita, M., Ishizaki, T., and Narumiya, S. (2010). Rho and anillin-dependent control of mDia2 localization and function in cytokinesis. Mol. Biol. Cell *21*, 3193–3204. https://doi.org/10.1091/mbc.E10-04-0324.

59. D'Avino, P.P., Takeda, T., Capalbo, L., Zhang, W., Lilley, K.S., Laue, E.D., and Glover, D.M. (2008). Interaction between Anillin and RacGAP50C connects the actomyosin contractile ring with spindle microtubules at the cell division site. J. Cell Sci. *121*, 1151–1158. https://doi.org/10.1242/jcs.026716.

60. Goldbach, P., Wong, R., Beise, N., Sarpal, R., Trimble, W.S., and Brill, J.A. (2010). Stabilization of the actomyosin ring enables spermatocyte cytokinesis in Drosophila. Mol. Biol. Cell *21*, 1482–1493. https://doi.org/10.1091/mbc.e09-08-0714.

61. Maddox, A.S., Lewellyn, L., Desai, A., and Oegema, K. (2007). Anillin and the Septins Promote Asymmetric Ingression of the Cytokinetic Furrow. Dev. Cell *12*, 827–835. https://doi.org/10.1016/j.devcel.2007.02.018.

62. Budnar, S., Husain, K.B., Gomez, G.A., Naghibosadat, M., Varma, A., Verma, S., Hamilton, N.A., Morris, R.G., and Yap, A.S. (2019). Anillin Promotes Cell Contractility by Cyclic Resetting of RhoA Residence Kinetics. Dev. Cell *49*, 894–906.e12. https://doi.org/10.1016/j.devcel.2019.04.031.

63. Kučera, O., Siahaan, V., Janda, D., Dijkstra, S.H., Pilátová, E., Zatecka, E., Diez, S., Braun, M., and Lansky, Z. (2021). Anillin propels myosin-independent constriction of actin rings. Nat. Commun. *12* (*1*). https://doi.org/10.1038/s41467-021-24474-1.

64. Mostowy, S., and Cossart, P. (2012). Septins: the fourth component of the cytoskeleton. Nat. Rev. Mol. Cell Biol. *13*, 183–194. https://doi.org/10.1038/nrm3284.

65. Estey, M.P., Di Ciano-Oliveira, C., Froese, C.D., Bejide, M.T., and Trimble, W.S. (2010). Distinct roles of septins in cytokinesis: SEPT9 mediates midbody abscission. J. Cell Biol. *191*, 741–749. https://doi.org/10.1083/jcb.201006031.

66. Nguyen, T.Q., Sawa, H., Okano, H., and White, J.G. (2000). The C. elegans septin genes, unc-59 and unc-61, are required for normal postembryonic cytokineses and morphogenesis but have no essential function in embryogenesis. J. Cell Sci. *113*, 3825–3837. https://doi.org/10.1101/gad.831500.

67. Green, R.A., Mayers, J.R., Wang, S., Lewellyn, L., Desai, A., Audhya, A., and Oegema, K. (2013). The midbody ring scaffolds the abscission machinery in the absence of midbody microtubules. J. Cell Biol. *203*, 505–520. https://doi.org/10.1083/jcb.201306036.

68. Kechad, A., Jananji, S., Ruella, Y., and Hickson, G.R.X. (2012). Anillin Acts as a Bifunctional Linker Coordinating Midbody Ring Biogenesis during Cytokinesis. Curr. Biol. *22*, 197–203. https://doi.org/10.1016/j.cub.2011.11.062.

69. Renshaw, M.J., Liu, J., Lavoie, B.D., and Wilde, A. (2014). Anillin-dependent organization of septin filaments promotes intercellular bridge elongation and Chmp4B targeting to the abscission site. Open Biol. *4*, 130190. https://doi.org/10.1098/rsob.130190.

70. Lewellyn, L., Dumont, J., Desai, A., and Oegema, K. (2010). Analyzing the effects of delaying aster separation on furrow formation during cytokinesis in the Caenorhabditis elegans embryo. Mol. Biol. Cell *21*, 50–62. https://doi.org/10.1091/mbc.E09-01-0089.

71. Garno, C., Irons, Z.H., Gamache, C.M., McKim, Q., Reyes, G., Wu, X., Shuster, C.B., and Henson, J.H. (2021). Building the cytokinetic contractile ring in an early embryo: Initiation as clusters of myosin ii, anillin and septin, and visualization of a septin filament network. PLoS One, 1–27. https://doi.org/10.1371/journal.pone.0252845.

72. Fenix, A.M., Taneja, N., Buttler, C.A., Lewis, J., Van Engelenburg, S.B., Ohi, R., and Burnette, D.T. (2016). Expansion and concatenation of non-muscle myosin IIA filaments drive cellular contractile system formation during interphase and mitosis. Mol. Biol. Cell *27*, 1465–1478. https://doi.org/10.1091/mbc.E15-10-0725.

73. Beach, J.R., Shao, L., Remmert, K., Li, D., Betzig, E., and Hammer, J.A., III. (2014). Nonmuscle Myosin II Isoforms Coassemble in Living Cells. Curr. Biol. *24*, 1160–1166. https://doi.org/10.1016/j.cub.2014.03.071.

74. Osório, D.S., Chan, F.Y., Saramago, J., Leite, J., Silva, A.M., Sobral, A.F., Gassmann, R., and Carvalho, A.X. (2019). Crosslinking activity of nonmuscle myosin II is not sufficient for embryonic cytokinesis in C. elegans. Development *146*, dev179150. https://doi.org/10.1242/dev.179150.

75. Neujahr, R., Heizer, C., and Gerisch, G. (1997). Myosin II-independent processes in mitotic cells of Dictyostelium discoideum: redistribution of the nuclei, re-arrangement of the actin system and formation of the cleavage furrow. J. Cell Sci. *110*, 123–137.

76. Nagasaki, A., Kanada, M., and Uyeda, T.Q. (2009). Cell adhesion molecules regulate contractile ring-independent cytokinesis in Dictyostelium discoideum. Cell Res. *19*, 236–246. https://doi.org/10.1038/cr.2008.318.

77. Dix, C.L., Matthews, H.K., Uroz, M., McLaren, S., Wolf, L., Heatley, N., Win, Z., Almada, P., Henriques, R., Boutros, M., et al. (2018). The Role of Mitotic Cell-Substrate Adhesion Re- modeling in Animal Cell Division. Dev. Cell *45*, 132–145.e3. https://doi.org/10.1016/j.devcel.2018.03.009.

78. Onishi, M., Umen, J.G., Cross, F.R., and Pringle, J.R. (2020). Cleavage-furrow formation without F-actin in Chlamydomonas. Proc. Natl. Acad. Sci. USA *117*, 18511–18520. https://doi.org/10.1073/pnas.1920337117.

79. Jordan, S.N., Davies, T., Zhuravlev, Y., Dumont, J., Shirasu-Hiza, M., and Canman, J.C. (2016). Cortical PAR polarity proteins promote robust cytokinesis during asymmetric cell division. J. Cell Biol. *212*, 39–49. https://doi.org/10.1083/jcb.201510063.

80. Pruyne, D. (2016). Revisiting the Phylogeny of the Animal Formins: Two New Subtypes, Relationships with Multiple Wing Hairs Proteins, and a Lost Human Formin. PLoS One *11*, e0164067. https://doi.org/10.1371/journal.pone.0164067.

81. Davies, T., Kim, H.X., Romano Spica, N., Lesea-Pringle, B.J., Dumont, J., Shirasu-Hiza, M., and Canman, J.C. (2018). Cell-intrinsic and -extrinsic mechanisms promote cell-type-specific cytokinetic diversity. Elife *7*, e36204. https://doi.org/10.7554/eLife.36204.

82. Ding, W.Y., Ong, H.T., Hara, Y., Wongsantichon, J., Toyama, Y., Robinson, R.C., Nédélec, F., and Zaidel-Bar, R. (2017). Plastin increases cortical connectivity to facilitate robust polarization and timely cytokinesis. J. Cell Biol. *216*, 1371–1386. https://doi.org/10.1083/jcb.201603070.

83. Chan, F.Y., Silva, A.M., Saramago, J., Pereira-Sousa, J., Brighton, H.E., Pereira, M., Oegema, K., Gassmann, R., and Carvalho, A.X. (2019). The ARP2/3 complex prevents excessive formin activity during cytokinesis. Mol. Biol. Cell *30*, 96–107. https://doi.org/10.1091/mbc.E18-07-0471.

84. Werner, M., Munro, E., and Glotzer, M. (2007). Astral Signals Spatially Bias Cortical Myosin Recruitment to Break Symmetry and Promote Cytokinesis. Curr. Biol. *17*, 1286–1297. https://doi.org/10.1016/j.cub.2007.06.070.

85. Panagiotou, T.C., Chen, A., and Wilde, A. (2022). An anillin-CIN85-SEPT9 complex promotes intercellular bridge maturation required for successful cytokinesis. Cell Rep. *40*, 111274. https://doi.org/10.1016/j.celrep.2022.111274.

86. Kinoshita, M., Field, C.M., Coughlin, M.L., Straight, A.F., and Mitchison, T.J. (2002). Self- and Actin-Templated Assembly of Mammalian Septins. Dev. Cell *3*, 791–802. https://doi.org/10.1016/S1534-5807(02)00366-0.

87. Shivas, J.M., and Skop, A.R. (2012). Arp2/3 mediates early endosome dynamics necessary for the maintenance of PAR asymmetry in Caenorhabditis elegans. Mol. Biol. Cell *23*, 1917–1927. https://doi.org/10.1091/mbc.E12-01-0006.

88. Sobral, A.F., Chan, F.Y., Norman, M.J., Osório, D.S., Dias, A.B., Ferreira, V., Barbosa, D.J., Cheerambathur, D., Gassmann, R., Belmonte, J.M., and Carvalho, A.X. (2021). Plastin and spectrin cooperate to stabilize the actomyosin cortex during cytokinesis. Curr. Biol. *31*, 5415–5428.e10. https://doi.org/10.1016/j.cub.2021.09.055.

89. Michaux, J.B., Robin, F.B., McFadden, W.M., and Munro, E.M. (2018). Excitable RhoA dynamics drive pulsed contractions in the early C. elegans embryo. J. Cell Biol. *217*, 4230–4252. https://doi.org/10.1083/jcb.201806161.

90. Tse, Y.C., Werner, M., Longhini, K.M., Labbé, J.-C., Goldstein, B., and Glotzer, M. (2012). RhoA activation during polarization and cytokinesis of the early Caenorhabditis elegans embryo is differentially dependent on NOP-1 and CYK-4. Mol. Biol. Cell *23*, 4020–4031. https://doi.org/10.1091/mbc.E12-04-0268.

91. Carim, S.C., Kechad, A., and Hickson, G.R.X. (2020). Animal Cell Cytokinesis: The Rho-Dependent Actomyosin-Anilloseptin Contractile Ring as a Membrane Microdomain Gathering, Compressing, and Sorting Machine. Front. Cell Dev. Biol. *8*, 575226. https://doi.org/10.3389/fcell.2020.575226.

92. Chatterjee, M., and Pollard, T.D. (2019). The Functionally Important N-Terminal Half of Fission Yeast Mid1p Anillin Is Intrinsically Disordered and Undergoes Phase Separation. Biochemistry *58*, 3031–3041. https://doi.org/10.1021/acs.biochem.9b00217.

93. Leite, J., Osorio, D.S., Sobral, A.F., Silva, A.M., and Carvalho, A.X. (2019). Network Contractility During Cytokinesis—from Molecular to Global Views. Biomolecules *9*, 194–128. https://doi.org/10.3390/biom9050194.

94. Willet, A.H., DeWitt, A.K., Beckley, J.R., Clifford, D.M., and Gould, K.L. (2019). NDR Kinase Sid2 Drives Anillin-like Mid1 from the Membrane to Promote Cytokinesis and Medial Division Site Placement. Curr. Biol. *29*, 1055–1063.e2. https://doi.org/10.1016/j.cub.2019.01.075.

95. Liu, X., Shu, S., Billington, N., Williamson, C.D., Yu, S., Brzeska, H., Donaldson, J.G., Sellers, J.R., and Korn, E.D. (2016). Mammalian Nonmuscle Myosin II Binds to Anionic Phospholipids with Concomitant Dissociation of the Regulatory Light Chain. J. Biol. Chem. *291*, 24828–24837. https://doi.org/10.1074/jbc.M116.739185.

96. Su, K.-C., Takaki, T., and Petronczki, M. (2011). Targeting of the RhoGEF Ect2 to the equatorial membrane controls cleavage furrow formation during cytokinesis. Dev. Cell *21*, 1104–1115. https://doi.org/10.1016/j.devcel.2011.11.003.

97. Lekomtsev, S., Su, K.-C., Pye, V.E., Blight, K., Sundaramoorthy, S., Takaki, T., Collinson, L.M., Cherepanov, P., Divecha, N., and Petronczki, M. (2012). Centralspindlin links the mitotic spindle to the plasma membrane during cytokinesis. Nature *492*, 276–279. https://doi.org/10.1038/nature11773.

98. Cavini, I.A., Leonardo, D.A., Rosa, H.V.D., Castro, D.K.S.V., D'Muniz Pereira, H., Valadares, N.F., Araujo, A.P.U., and Garratt, R.C. (2021). The Structural Biology of Septins and Their Filaments: An Update. Front. Cell Dev. Biol. *9*, 765085. https://doi.org/10.3389/fcell.2021.765085.

99. Celton-Morizur, S., Bordes, N., Fraisier, V., Tran, P.T., and Paoletti, A. (2004). C-terminal anchoring of mid1p to membranes stabilizes cytokinetic ring position in early mitosis in fission yeast. Mol. Cell Biol. *24*, 10621–10635. https://doi.org/10.1128/MCB.24.24.10621-10635.2004.

100. Ong, J.Y., and Torres, J.Z. (2020). Phase Separation in Cell Division. Mol. Cell *80*, 9–20. https://doi.org/10.1016/j.molcel.2020.08.007.

101. Weirich, K.L., Banerjee, S., Dasbiswas, K., Witten, T.A., Vaikuntanathan, S., and Gardel, M.L. (2017). Liquid behavior of cross-linked actin bundles. Proc. Natl. Acad. Sci. USA *114*, 2131–2136. https://doi.org/10.1073/pnas.1616133114.

102. Scheff, D.R., Weirich, K.L., Dasbiswas, K., Patel, A., Vaikuntanathan, S., and Gardel, M.L. (2020). Tuning Shape and Internal Structure of Protein Droplets via Biopolymer Filaments. Soft Matter, 1–10. https://doi.org/10.1039/C9SM02462J.

103. Naganathan, S.R., Fürthauer, S., Rodriguez, J., Fievet, B.T., Jülicher, F., Ahringer, J., Cannistraci, C.V., and Grill, S.W. (2018). Morphogenetic degeneracies in the actomyosin cortex. Elife *7*, 354. https://doi.org/10.7554/eLife.37677.

104. Hird, S.N., and White, J.G. (1993). Cortical and cytoplasmic flow polarity in early embryonic cells of Caenorhabditis elegans. J. Cell Biol. *121*, 1343–1355. https://doi.org/10.1083/jcb.121.6.1343.

105. Li, Y., and Munro, E. (2021). Filament-guided filament assembly provides structural memory of filament alignment during cytokinesis. Dev. Cell *56*, 2486–2500.e6. https://doi.org/10.1016/j.devcel.2021.08.009.

106. Ganar, K.A. (2021). Shaping Synthetic Cells through Cytoskeleton-Condensate-Membrane Interactions. Curr. Opin. Colloid Interface Sci., 1–12. https://doi.org/10.1016/j.cocis.2021.101459.

107. Quail, T., Golfier, S., Elsner, M., Ishihara, K., Murugesan, V., Renger, R., Jülicher, F., and Brugués, J. (2021). Force generation by protein–DNA cocondensation. Nat. Phys. *17*, 1007–1012. https://doi.org/10.1038/s41567-021-01285-1.

108. Bergeron-Sandoval, L.-P., Kumar, S., Heris, H.K., Chang, C.L.A., Cornell, C.E., Keller, S.L., François, P., Hendricks, A.G., Ehrlicher, A.J., Pappu, R.V., and Michnick, S.W. (2021). Endocytic proteins with prion-like domains form viscoelastic condensates that enable membrane remodeling. Proc. Natl. Acad. Sci. USA *118*, e2113789118. https://doi.org/10.1073/pnas.2113789118.

109. Yuan, F., Alimohamadi, H., Bakka, B., Trementozzi, A.N., Day, K.J., Fawzi, N.L., Rangamani, P., and Stachowiak, J.C. (2021). Membrane bending by protein phase separation. Proc. Natl. Acad. Sci. USA *118*, e2017435118. https://doi.org/10.1073/pnas.2017435118.

110. Harker-Kirschneck, L., Hafner, A.E., Yao, T., Vanhille-Campos, C., Jiang, X., Pulschen, A., Hurtig, F., Hryniuk, D., Culley, S., Henriques, R., et al. (2022). Physical mechanisms of ESCRT-III-driven cell division. Proc. Natl. Acad. Sci. USA *119*, e2107763119. https://doi.org/10.1073/pnas.2107763119.

111. Tarrason Risa, G., Hurtig, F., Bray, S., Hafner, A.E., Harker-Kirschneck, L., Faull, P., Davis, C., Papatziamou, D., Mutavchiev, D.R., Fan, C., et al. (2020). The proteasome controls ESCRT-III-mediated cell division in an archaeon. Science *369*, eaaz2532. https://doi.org/10.1126/science.aaz2532.

112. Bell, K.R., Werner, M.E., Doshi, A., Cortes, D.B., Sattler, A., Vuong-Brender, T., Labouesse, M., and Maddox, A.S. (2020). Novel cytokinetic ring components drive negative feedback in cortical contractility. Mol. Biol. Cell *31*, 1623–1636. https://doi.org/10.1091/mbc.E20-05-0304.

113. Dickinson, D.J., Schwager, F., Pintard, L., Gotta, M., and Goldstein, B. (2017). A Single-Cell Biochemistry Approach Reveals PAR Complex Dynamics during Cell Polarization. Dev. Cell *42*, 416–434.e11. https://doi.org/10.1016/j.devcel.2017.07.024.

114. Frøkjaer-Jensen, C., Davis, M.W., Hopkins, C.E., Newman, B.J., Thummel, J.M., Olesen, S.-P., Grunnet, M., and Jorgensen, E.M. (2008). Single-copy insertion of transgenes in Caenorhabditis elegans. Nat. Genet. *40*, 1375–1383. https://doi.org/10.1038/ng.248.

115. Chen, D., Hastie, E., and Sherwood, D. (2019). Endogenous Expression of UNC-59/Septin in *C. elegans*. MicroPubl. Biol. https://doi.org/10.17912/micropub.biology.000200.

116. Schindelin, J., Arganda-Carreras, I., Frise, E., Kaynig, V., Longair, M., Pietzsch, T., Preibisch, S., Rueden, C., Saalfeld, S., Schmid, B., et al. (2012). Fiji: an open-source platform for biological-image analysis. Nat. Methods *9*, 676–682. https://doi.org/10.1038/nmeth.2019.

117. Stiernagle, T. (2006). Maintenance of *C. elegans*. WormBook, 1–11. https://doi.org/10.1895/wormbook.1.101.1.

118. Carvalho, A., Olson, S.K., Gutierrez, E., Zhang, K., Noble, L.B., Zanin, E., Desai, A., Groisman, A., and Oegema, K. (2011). Acute Drug Treatment in the Early C. elegans Embryo. PLoS One *6*, e24656–e24658. https://doi.org/10.1371/journal.pone.0024656.

119. Zanin, E., Dumont, J., Gassmann, R., Cheeseman, I., Maddox, P., Bahmanyar, S., Carvalho, A., Niessen, S., YatesIII, J.R., Oegema, K., and Desai, A. (2011). Affinity Purification of Protein Complexes in C. elegans, Second edition (Elsevier Inc.). https://doi.org/10.1016/B978-0-12-544172-8.00011-6.

120. Liu, Z.Q. (1991). Scale space approach to directional analysis of images. Appl. Opt. *30*, 1369–1373. https://doi.org/10.1364/AO.30.001369.

STAR★METHODS

KEY RESOURCES TABLE

REAGENT or RESOURCE	SOURCE	IDENTIFIER
Antibodies		
Mouse monoclonal anti-GFP (clones 7.1 and 13.1)	Roche	Cat#11814460001; RRID: AB_390913
Mouse monoclonal anti-Actin (clone AC-15)	Sigma-Aldrich	Cat#A1978; RRID: AB_476692
Mouse monoclonal anti-FLAG (clone M2)	Sigma-Aldrich	Cat#F1804; RRID: AB_262044
Mouse monoclonal anti-Strep-tag™ II	IBA Lifesciences	Cat#2-1507-001; RRID: AB_513133
Mouse monoclonal anti-His-tag (clone HIS.H8)	Millipore	Cat#05-949; RRID: AB_492660
Goat anti-Mouse IgG (H/L)-HRP Conjugate antibody (polyclonal)	Bio-Rad	Cat#1706516; RRID: AB_11125547
Bacterial and virus strains		
Escherichia coli OP50	Caenorhabditis Genetics Center (CGC)	N/A
Escherichia coli DH5a	Thermo Fisher Scientific	Cat#18265017
Escherichia coli HT115 (DE3)	N/A	N/A
Chemicals, peptides, and recombinant proteins		
ECL Prime Western Blotting Detection Reagent	Cytiva Amersham™	Cat#RPN2236
Pierce™ ECL Western Blotting Substrate	Thermo Fisher Scientific	Cat#32109
Latrunculin A	Enzo Life Sciences; Sigma-Aldrich	Cat#BML-T119; Cat#L5163
FM™ 4–64 Dye	Thermo Fisher Scientific	Cat#T13320
Critical commercial assays		
PIP Strips – Lipid-Protein Interaction Assay	Echelon Bioscience	Cat#P-6001
MEGAscript™ T7 Transcription Kit	Thermo Fisher Scientific	Cat#AM1334
Experimental models: organisms/strains		
Wild type (*Caenorhabditis elegans*)	Caenorhabditis Genetics Center (CGC)	N2
xsSi5 [pie-1p::GFP::ani-1^{AH-PH}::pie-1 3′UTR + Cbr-unc-119(+)]II	(Tse et al.)[90]	MG617
ani-1(mon7[mNeonGreen^3xFlag::ani-1]) III	(Rehain-Bell et al.)[112]	MDX29
zbIs2[pie-1p::LifeAct::RFP + unc-119(+)]	Zhirong Bao	BV70
nmy-2(cp52[nmy-2::mkate2 + LoxP unc-119(+) LoxP]) I; unc-119(ed3) III	(Dickinson et al.)[113]	LP229
cyk-1::gfp	(Reymann et al.)[22]	SWG004
oxTi179 II; unc-119(ed3) III	(Frøkjær-Jensen et al.)[114]	EG8079
unc-59(qy50[unc-59::GFP::3xflag::AID]) I	(Chen et al.)[115]	NK2225
ltIs157 [pAC16; ppie-1::LifeAct::GFP; unc-119 (+)]; unc- 119(ed3) III; prtSi2[pAC71; Pnmy-2:: re-encoded nmy- 2::mCherry:: StrepTagII::3′UTR nmy-2; cb-unc-119(+)] II	(Osório et al.)[74]	GCP22
nmy-2(cp13[nmy-2::gfp + LoxP]) I; OD56 (mCherry::histone H2B; ltIs44 [pie-1p::mCherry::PH(PLC1delta1)+unc-119(+)]	This study	ZAN23
ani-1(mon7[mNeonGreen^3xFlag::ani-1]) III; zbIs[pie-1:: LifeAct::RFP + unc-119(+)]	This study	ZAN348
nmy-2(cp52[nmy-2::mkate2 + LoxP unc-119(+) LoxP]) I; unc-119(ed3) III; ani-1(mon7[mNeonGreen^3xFlag::ani-1]) III	This study	ZAN351
nmy-2(cp52[nmy-2::mkate2 + LoxP unc-119(+) LoxP]) I; unc-119(ed3) III; xsSi5 [pie-1p::GFP::ani-1^{AH-PH}::pie-1 3′UTR + Cbr-unc-119(+)] II	This study	ZAN368

(*Continued on next page*)

Continued

REAGENT or RESOURCE	SOURCE	IDENTIFIER
cyk-1::gfp, zbIs2[pie-1p::LifeAct::RFP + unc-119(+)]	This study	ZAN371
Si192[pEZ379; pani-1::GFP::ANI-1RE-WT; cb-unc-119(+)]II; unc-119(ed3) III	This study	ZAN373
Si193[pEZ388; pani-1::GFP::ANI-1RE-Δ236-460AA; cb-unc-119(+)]II; unc-119(ed3) III	This study	ZAN375
Si194[pEZ389; pani-1::GFP::ANI-1RE-Δ48-460AA; cb-unc-119(+)]II; unc-119(ed3) III	This study	ZAN376
Si197[pEZ390; pani-1::GFP::ANI-1$^{N-term-CX}$ (1-763AA-PBS-CX); cb-unc-119(+)]II; unc-119(ed3) III	This study	ZAN379
Si200[pEZ391; pani-1::GFP::ANI-1^{C-term} (Δ48-680AA); cb-unc-119(+)]II; unc-119(ed3) III	This study	ZAN382
Si201[pEZ387; pani-1::GFP::ANI-1RE-Δ48–160; cb-unc-119(+)]II; unc-119(ed3) III	This study	ZAN383
Si203[pEZ419; pani-1::GFP::ANI-1^{N-term} (1-763AA); cb-unc-119(+)]II; unc-119(ed3) III	This study	ZAN386
Si204[pEZ422; pani-1::GFP::ANI-1$^{Linker-CX}$ (1-47AA, 441–763 AA-PBS-CX); cb-unc-119(+)]II; unc-119(ed3) III	This study	ZAN387
Si205[pEZ421; pani-1::GFP::ANI-1$^{M-ABD-CX}$ (1-459AA-PBS-CX); cb-unc-119(+)]II; unc-119(ed3) III	This study	ZAN390
Si206[pEZ420; pani-1::GFP::ANI-1^{ΔLinker} (Δ460-763AA); cb-unc-119(+)]II; unc-119(ed3) III	This study	ZAN391
unc-59(qy50[unc-59::GFP::AID])I; ltIs37 [pAA64; pie-1/mCherry::his-58; unc-119 (+)]	This study	GCP1126
Recombinant DNA		
pACEbac1-6xHis:nmy-2	This study	N/A
pACEbac1-StrepTagII:mlc-4	(Osório et al.)[74]	pAC437
pACEbac1-StrepTagII:mlc-5	(Osório et al.)[74]	pAC438
pCFJ350: pani-1::gfp::ani-1RE-WT::ani-1	This study	pEZ379
pCFJ350: pani-1::gfp::ani-1RE-Δ48-160AA::ani-1	This study	pEZ387
pCFJ350: pani-1::gfp::ani-1RE-Δ236-460AA::ani-1	This study	pEZ388
pCFJ350: pani-1::gfp::ani-1RE-Δ48-460AA::ani-1	This study	pEZ389
pCFJ350: pani-1::gfp::ani-1^{N-term} (1-763AA-PBS-CX)::ani-1	This study	pEZ390
pCFJ350: pani-1::gfp::ani-1^{C-term} (Δ48-680AA)::ani-1	This study	pEZ391
pCFJ350: pani-1::gfp::ani-1^{N-term} (1-763AA)::ani-1	This study	pEZ419
pCFJ350: pani-1::gfp::ani-1^{ΔLinker} (Δ460-763AA)::ani-1	This study	pEZ420
pCFJ350: pani-1::gfp::ani-1$^{Linker-CX}$ (1-47AA, 441-763AA-PBS-CX)::ani-1	This study	pEZ422
pCFJ350: pani-1::gfp::ani-1$^{M-ABD-CX}$ (1-459AA-PBS-CX)::ani-1	This study	pEZ421
Software and algorithms		
NIS Elements 5.21.03	Nikon	https://www.microscope.healthcare.nikon.com/en_EU/products/software/nis-elements

(*Continued on next page*)

Continued

REAGENT or RESOURCE	SOURCE	IDENTIFIER
LAS X 3.5.7.23225	Leica	https://www.leica-microsystems.com/products/microscope-software/p/leica-las-x-ls/
Andor iQ3	Oxford Instruments	https://andor.oxinst.com/
Fiji (ImageJ) 1.54	Schindelin et al.[116]	https://imagej.nih.gov/ij/
Prism 9	GraphPad	https://www.graphpad.com/
Image Lab v. 5.2.1	Bio-Rad	http://www.bio-rad.com/
MS Excel	Microsoft	https://www.microsoft.com/
KNIME Analytics Platform 4.6.3	KNIME	https://www.knime.com/

RESOURCE AVAILABILITY

Lead contact

Further information and requests for resources and reagents should be directed to and will be fulfilled by the lead contact, Esther Zanin (esther.zanin@fau.de).

Materials availability

C. elegans strains and plasmids generated in this study will be made available upon request via the lead contact.

Data and code availability

This paper does not report original code. Primary data associated with the paper is available upon reasonable request.

EXPERIMENTAL MODEL AND SUBJECT DETAILS

C. elegans strains were maintained at 20°C on NGM plates seeded with *Escherichia coli* (OP50).[117] Details of the used worm strains[112,113,115] are provided in key resources table.

RNAi experiments were performed by injection or feeding and details of the RNAi experiments are listed in Table S1. For the generation of dsRNA for injection the target sequence was amplified by PCR from cDNA or genomic DNA with sequence specific primers containing T7 overhangs on both sides (Table S1). The purified PCR product was used as a template for the *in vitro* transcription reaction using the MEGAscript T7 kit (AM1334 Invitrogen, Thermo Fischer). dsRNA was injected into young hermaphrodites mounted on 2% agarose pads. After injections worms were rescued on OP50 seeded NGM plates and incubated at 20°C for 15–19 h (*perm-1*), 24–28 h (*nmy-2*), or 39–49 h (*cyk-1*, *ani-1*, *arx-2*, *septin*$^{unc-59}$, *septin*$^{unc-61}$). Since *septin*$^{unc-61}$*(RNAi)* and septin co-depletion showed a similar phenotype, we pursued most experiments with *septin*$^{unc-61}$*(RNAi)*. For *perm-1* and *ani-1* double RNAi (Figure S9D), worms were first injected with *ani-1* dsRNA and after 30 h incubation time at 20°C injected again with *perm-1* dsRNA. For *cyk-1* or *cyk-1; septin*$^{unc-61}$ and *nmy-2* double/triple RNAi (Figure 3), worms were first injected with *cyk-1* or *cyk-1; septin*$^{unc-61}$ dsRNA and after 22 h incubation time at 20°C injected again with *nmy-2* dsRNA.

For feeding RNAi, L4440 vectors carrying part of the sequence of *ani-1* or *perm-1* were obtained from the Ahringer library (Source Bioscience), sequenced to confirm the gene target, and transformed into HT115 (DE3) bacteria. Briefly, the RNAi bacterial clones were grown until an OD of 1.6 in 50 mL Lysogeny broth (LB) medium containing 12.5 μg/mL tetracycline and 50 μg/mL ampicillin overnight at 37°C. The overnight culture was centrifuged at 4000 g for 10 min, the supernatant was removed, and the cell pellet was resuspended in 2.5 mL LB medium containing 12.5 μg/mL tetracycline, 50 μg/mL ampicillin, and 0.23 mg/mL IPTG (isopropyl β-D-1-thiogalactopyranoside). In parallel, unseeded NGM plates were dried for 1 h in a 37°C incubator. Then, 100 μL of a 1:1:1 mix of 50 μg/mL ampicillin, 12.5 μg/mL tetracycline, and 0.1 g/mL IPTG was added. These treated plates were inoculated with 100 μL of bacterial culture. To obtain permeabilized embryos in Figures 4 and S6, the inoculated bacterial culture consisted of 20 μL of bacteria expressing *perm-1* dsRNA[118] and 80 μL of LB (*perm-1(RNAi)* alone), or 20 μL of bacteria expressing *perm-1* dsRNA and 80 μL of bacteria expressing *ani-1* (*perm-1(RNAi)*). The expression of dsRNA was induced for 5 h at 37°C, in the dark. 25–30 L4 stage hermaphrodites were added to the treated plates and incubated at 20°C for 45–48 h before dissection for imaging. For Latrunculin A treatment in Figure S9D hermaphrodites were injected first injected with *ani-1* and subsequently with *perm-1* day RNA as described above.

METHOD DETAILS

Embryonic lethality counts

To determine embryonic lethality after *ani-1(RNAi)*, young adult worms were injected with *ani-1* dsRNA and incubated at 20°C for 48 h. Afterward, injected worms were singled on NGM plates, incubated 20 h and sacrificed after 24 h. The number of larvae and dead embryos was counted 24 h later.

Immunoblotting

For immunoblotting, worms were picked in MPEG (M9 plus 0.05% polyethylene glycol 8000 (PEG)) buffer and washed three times. The volume of the MPEG buffer was reduced and sample buffer was added to reach approximately 1 worm/μL. Worms were incubated at 95°C for 5 min, followed by centrifugation at room temperature for 10 min at 20000 *g* to spin down debris and subsequently 20 μL of supernatant were loaded in each lane.[119] Membranes were incubated with anti-Actin (A1978 Sigma, 1:6000), anti-FLAG (F1804 Sigma, 1:2500) or anti-GFP (11814460001 Roche, 1:600) primary antibodies. HRP-conjugated mouse (1706516 Bio-Rad, 1:7500) were used as secondary antibodies.

Mos1-mediated single copy insertion (MosSCI) of ANI-1 variants

For the *gfp::ani-1* transgenes the genomic *ani-1* locus (6507 bp) with its promotor (565 bp) and 3′UTR (319 bp) were cloned together with GFP into pCFJ350 by Gibson cloning. ANI-1 transgenes were *ani-1* RNAi resistant so that we could specifically deplete endogenous ANI-1 by RNAi and test the function of the ANI-1 variants. For this, exon 5 was rendered RNAi resistant by amino acid codon shuffling (Figure S8D). For the ANI-1$^{N-term-CX}$, ANI-1$^{Linker-CX}$, ANI-1$^{M-ABD-CX}$ variants the PBS and the CX motif of RHO-1 (*C. elegans* RhoA, AA181-192) were fused to the C-terminal end. We chose this region as a membrane anchor, since it was sufficient for membrane localization and did not exhibit any specific cortical enrichment during anaphase. All transgenes are listed in the key resources table.

Ani-1 transgenes were integrated on chromosome II (EG8079) using the MosSCI method.[114] Young hermaphrodites were mounted on 2% agarose pads and injected with a mix containing the vector carrying the *ani-1* transgene, the transposase (pCFJ601) and co-injection markers (pCFJ90 and pCFJ104). Worms were singled on NGM plates seeded with OP50 and incubated at 25°C for 7–10 days until starved. Wild type movers, negative for the mCherry-tagged array markers, were checked for homozygous GFP expression and correct integration was verified using PCR.

Fluorescence microscopy and image analysis

C. elegans gravid hermaphrodites were dissected in 4 μL M9 buffer on a 18 × 18 mm coverslip. The embryos were mounted on a 2% agarose pad by inverting the coverslip onto the pad and then sealed with vaseline. Confocal images (Figures 1, 2, 3, S1A, S1F, S2, S3A, S4, and S5) were acquired using a Nikon inverted microscope (Eclipse Ti) equipped with a confocal spinning disk unit, a 100× 1.45-NA Plan-Apochromat oil immersion objective and an Andor DU-888 X-11056 camera (1024x1024 pixels). The system was controlled by NIS Elements software. GFP and red-fluorescent probes were imaged using 488 nm and 561 nm lasers, respectively, and for some experiments transmission images were acquired in the central plane. Confocal images of Figures 5A, 5D, 5E, 6E, S9B, and S9C were acquired on the Leica SP8 confocal laser scanning microscope equipped with a white light laser, 63x/1.3 GLYC objective and a photomultiplier and of Figures 5F, 6A, 6B, 6F, S1E, S3C, S7, and S9D, on a Leica TCS SP8 DIVE-FALCON equipped with 488 nm argon and 561 nm lasers and APO CS2 63x/1.4 oil objective. To display images acquired on the Leica SP8, a Gaussian Blur filter with a radius of 0.8 was applied to reduce noise. Cortical images in Figures 4 and S6 were acquired on a spinning disk confocal system (Andor Revolution XD Confocal System; Andor Technology) with a confocal scanner unit (CSU-X1; Yokogawa Electric Corporation) mounted on an inverted microscope (Ti-E, Nikon) equipped with a 60×1.4 NA Plan-Apochromat oil objective and solid-state lasers of 488 nm (50 mW) and 561 nm (50 mW). For image acquisition, 12 × 0.5 μm z-stacks were collected every 5 s by using an electron multiplication back-thinned charge coupled device camera (iXon Ultra 897; Andor Technology). Acquisition parameters, shutters and focus were controlled by Andor iQ3 software. Wide-field fluorescent and DIC images in Figures 7A and S10A were acquired on either a Nikon Ti2-Eclipse microscope equipped with a CFI Apochromat 100×1.49 NA oil objective and a Prime 95B, A18E203001 camera or on a Zeiss AxioImager.Z1 ApoTome microscope equipped with a 63×1.4-NA Plan-Apochromat oil immersion objective (Zeiss) and AxioCamMR3 camera to measure contractile ring diameter.

Image analysis and quantification was performed in Fiji.[116] All data analysis was performed in Excel, Prism (GraphPad) or KNIME analytics (http://www.knime.org) and figures were assembled with the Affinity Designer software.

For high-time resolution data, imaging was started during pronuclear migration with central planes images acquired every 16 s (Figures 2, 3, 5, 6, S1, S2E, S3, S4, S5A, S7, and S9). At the time of NEBD (defined as the time point when the border of the nucleus was no longer visible in the DIC channel) imaging was stopped and resumed at the cell cortex before anaphase onset with a time interval of 2.5 s (Figures 2, 3, S1A, S1F, S2E, S4, and S5A) or 5 s (Figures 5, 6, S1E, S3C, S7, and S9).

Fluorescence intensity along cortical plane images (Figures 5B, 6C, S1B, S1E, S1F, S2E, S3B, S3E, S4C, S5B, S5E, and S6F) was measured by drawing a wide line from the anterior to the posterior cortex of the embryo 180 s after NEBD, which is around the time of contractile ring assembly (Figure S1B). Cortical fluorescence intensity was normalized by dividing by the mean cytoplasmic intensity measured in a rectangular box in the posterior region of central plane images at the time of NEBD. The mean normalized cortical

intensity was calculated for 101 intervals from the anterior (0%) to the posterior (100%) for each embryo. To correct the fluorescent signal for bleaching, the mean cortical intensity was measured over time in a rectangular box in the posterior region for each embryo. The mean fluorescence intensity relative to the initial intensity was calculated for control embryos ($n \geq 11$) for each time point and used as a 'correction coefficient'. To correct for bleaching, the fluorescent intensity measured at a specific time point was multiplied with the 'correction coefficient' of this time point.

Directionality of ANI-1 and LifeAct was determined on cortical images that were processed by subtracting the mean fluorescence intensity measured outside the embryos. Subsequently a Gaussian Blur filter with a radius of 0.5 was applied followed by an Unsharp Mask filter with a radius of 2 pixels and a Mask Weight of 0.6. Images were also rotated (anterior – left, posterior – right). To measure directionality a rectangular box was placed at the cell equator at selected time points after NEBD and the ImageJ plugin 'Directionality' with the method local gradient orientation[120] was used. The orientation of ANI-1 and LifeAct was classified into 45 bins from 0° to 90° orientation. The mean percentage of ANI-1 and LifeAct structures with 0°–20°, reflecting anterior-posterior orientation, and 68°–88°, reflecting circumferentially orientation, was calculated for each embryo.

The number of linear and non-linear structures was analyzed on cortical images that were processed as described for the directionality analysis. Additionally, the mean fluorescence intensity measured at the anterior cortex was subtracted from the cortical image at the end. A rectangular box was positioned at the cell equator (and anterior for ANI-1$^{N-term-CX}$ and ANI-1$^{Linker-CX}$ embryos) and the length and width of all structures was determined manually. For each structure the length/width ratio was calculated and structures with the length/width ratio <4 were classified as non-linear and structures with a length/width ratio ≥ 4 were classified as linear (Figure S3A).

The contractile ring diameter was measured manually on central plane images acquired every 20 s starting at NEBD. The initial ring diameter NEBD was set to 100% diameter width. Embryos were filmed from NEBD of the first cell division until to onset of the second cell division.

Latrunculin A treatment

Adult hermaphrodites that had been treated with *perm-1* dsRNA (see above) were dissected, and permeabilized embryos were filmed in meiosis medium (25 mM HEPES, pH 7.4, 0.5 mg/mL inulin, 20% heat-inactivated fetal bovine serum, and 60% Leibowitz-15 medium) without compression. Embryos were either imaged in an custom build microdevice containing microwells[118] (Figures 4 and S6) or in a self-made imaging chamber (Figures S7A and S9D). For the self-made chamber double sided tape was folded into two layers, a 5 mm well was introduced with a puncher and the tape was glued onto a freshly 0.1% poly-L-lysine coated 24 × 60 mm glass coverslip. Using a few drops of water, the coverslip was tapped onto a metal slide containing a central whole surrounding the well and 10 μL meiosis medium were added to the well in which the worms were dissected. 10 μM Latrunculin A (L5163 Sigma, BML-T119 Enzo Life Sciences) was added between metaphase and anaphase onset. At the end of each video, medium containing 33 μM FM 4–64 (T13320 Invitrogen/Thermo Scientific) was added to the imaging chamber to confirm that the imaged embryo was permeable.

6xHIS::NMY-2 cloning and NMY-2/MLC-4/MLC-5 protein expression

NMY-2 full length was amplified from *C. elegans* cDNA and cloned into the pACEbac1 expression vector using Gibson assembly with an N-terminal 6×Histidine tag followed by a flexible linker (GlySerGlySerGly). The primers used were oAC1233 - 5′-ACCATG GCTCTGGTAGCGGCACATCATCTCGACAAAAAGATGATGAG-3' (forward) and oAC1234 - 5′-TAGTACTTCTCGACAAGCTTTTAG TTGCGAACTGAGTCGCG GTCT-3' (reverse). The backbone was amplified from pACEbac1 vector using the following primers oAC1235 – 5′-AAGCTTGTCGAGAAGTACTAGAGGATCATAATC-3' (forward) and oAC1236 5′-GCCGCTACCAGAGCCATGG-3' (Reverse). Baculovirus expression of the 6xHIS::NMY-2 full-length/StreptagII::MLC-4/StreptagII:MLC-5 complex, cell lysates and tandem streptactin/Ni-NTA affinity chromatography were performed as described previously for NMY-2 HMM complexes.[74] The concentrated eluate of the Ni-NTA purification was dialyzed overnight in high salt buffer (10 mM MOPS, 500 mM NaCl, 3 mM NaN_3, 1 mM EDTA, 1 mM DTT (pH 7.3)). Glycerol and DTT were added to a final concentration of 10% (v/v) and 1 mM, respectively. Aliquots were flash-frozen in liquid nitrogen and stored at −80°C.

PIP strips and immunoblotting

To analyze lipid binding, PIP strips (P-6001 Echelon Bioscience) were used according to the manufacturer's instructions. Each membrane consists of 16 spots: 15 contain several lipids and 1 empty (blank). Additionally, on the empty space on the top of the membranes, was spotted with two controls for proper detection consisting of 1 μL of each protein sample (0.5–1 μg) or 1 μL of the secondary antibody pre-diluted 1:100 (secondary antibody control). The two control spots were allowed to dry before proceeding with the protocol. Membranes were then incubated with blocking solution (3% BSA fatty-acid free (Sigma-Aldrich) in PBS (Gibco, Thermo Fisher) with 0.1% (v/v) Tween 20) (PBS-T) for one 1 h at RT. Membranes were then incubated with 4 μg/mL of either StreptagII::MLC-4 or 6xHIS::NMY-2/Strep-tag II::MLC-4/Strep-tag II:MLC-5 complex in blocking buffer for 1 h at RT, followed by three washes in PBS-T with gentle agitation for 5 min. To detect bound proteins, membranes were incubated for 1 h at room temperature in blocking solution with mouse anti-Strep-tagII antibody (2-1507-001 IBA Lifesciences, 1:750) for Strep-tagII::MLC-4 detection or mouse anti-6xHistidine tag antibody (05–949 Millipore, 1:2,500) for 6xHIS::NMY-2 detection. After washing, membranes were incubated with HRP-conjugated anti-mouse antibody at 1:5,000 in blocking solution and incubated for 1 h at RT. This was followed by another round of three

washes and PBS was used for the final wash. All steps were performed under gentle agitation. Immunoblots were visualized by chemiluminescence using Pierce ECL Western Blotting Substrate (Thermo Fisher) and a ChemiDoc XRS+ System with Image Lab Software (Bio-Rad).

QUANTIFICATION AND STATISTICAL ANALYSIS

Statistical analysis was performed in Prism (GraphPad). Mean values are presented with error bars representing standard error of the mean (SEM) as indicated in the figure legends. For data with normal distribution a parametric (two sided Student's *t*-test) and with nonnormal distribution a Mann-Whitney-U test for was performed.

Cell Reports, Volume *42*

Supplemental information

Anillin forms linear structures and facilitates furrow ingression after septin and formin depletion

Mikhail Lebedev, Fung-Yi Chan, Anna Lochner, Jennifer Bellessem, Daniel S. Osório, Elisabeth Rackles, Tamara Mikeladze-Dvali, Ana Xavier Carvalho, and Esther Zanin

Table S1: dsRNA generation, T7 sequence is underlined

Gene	Oligonucleotide 1	Oligonucleotide 2	Source	RNAi condition	Concentration [µg/µl]
cyk-1	TAATACGACTCACTATAGGTTGGAGTTCGATGCAGAAGA	TAATACGACTCACTATAGGTTGCCTTGTCAGGAACTGAA	cDNA	injection	0.5-1.0
nmy-2	TAATACGACTCACTATAGGAATTGAATCTCGGTTGAAGGAA	TAATACGACTCACTATAGGACTGCATTTCACGCATCTTATG	cDNA	injection	0.18-0.36
ani-1	TAATACGACTCACTATAGGAGCCGGAGTTGGAAAGCTG	TAATACGACTCACTATAGGCCTATTCTTTTCCAAACGTTGC	genomic DNA	injection	0.35-0.7
unc-61	TAATACGACTCACTATAGGAGCGTGTTAATGTGATCCCAG	TAATACGACTCACTATAGGTCCAGTCTCTCCATCTCCAATC	genomic DNA	injection	0.3-1.0
unc-59	TAATACGACTCACTATAGGTGGGAGCCAATAGTGAACTAC	TAATACGACTCACTATAGGCGATTCTTCTCATTCTTCGGC	genomic DNA	injection	0.3
arx-2	TAATACGACTCACTATAGGCAGCTTCGTCAAATGCTTG	TAATACGACTCACTATAGGTATTTCCATGCAATACGCG	cDNA	injection	1.0
perm-1	TAATACGACTCACTATAGGAATTTTCTAGGTCGTCAATCTTCA	TAATACGACTCACTATAGGCGAAAACGCGATCATTTTTA	genomic DNA	injection	0.1
perm-1	AATGTTTATGAACCCGAGCG	TTCACGCAGTTGTTGACACA	[1]	feeding	N.A.
ani-1	CATGTTCACTGACAACTGGGATA	CAAACTCAATGGAGAGGACAATC	Bioscience	feeding	N.A.

Supplemental FIGURE 1

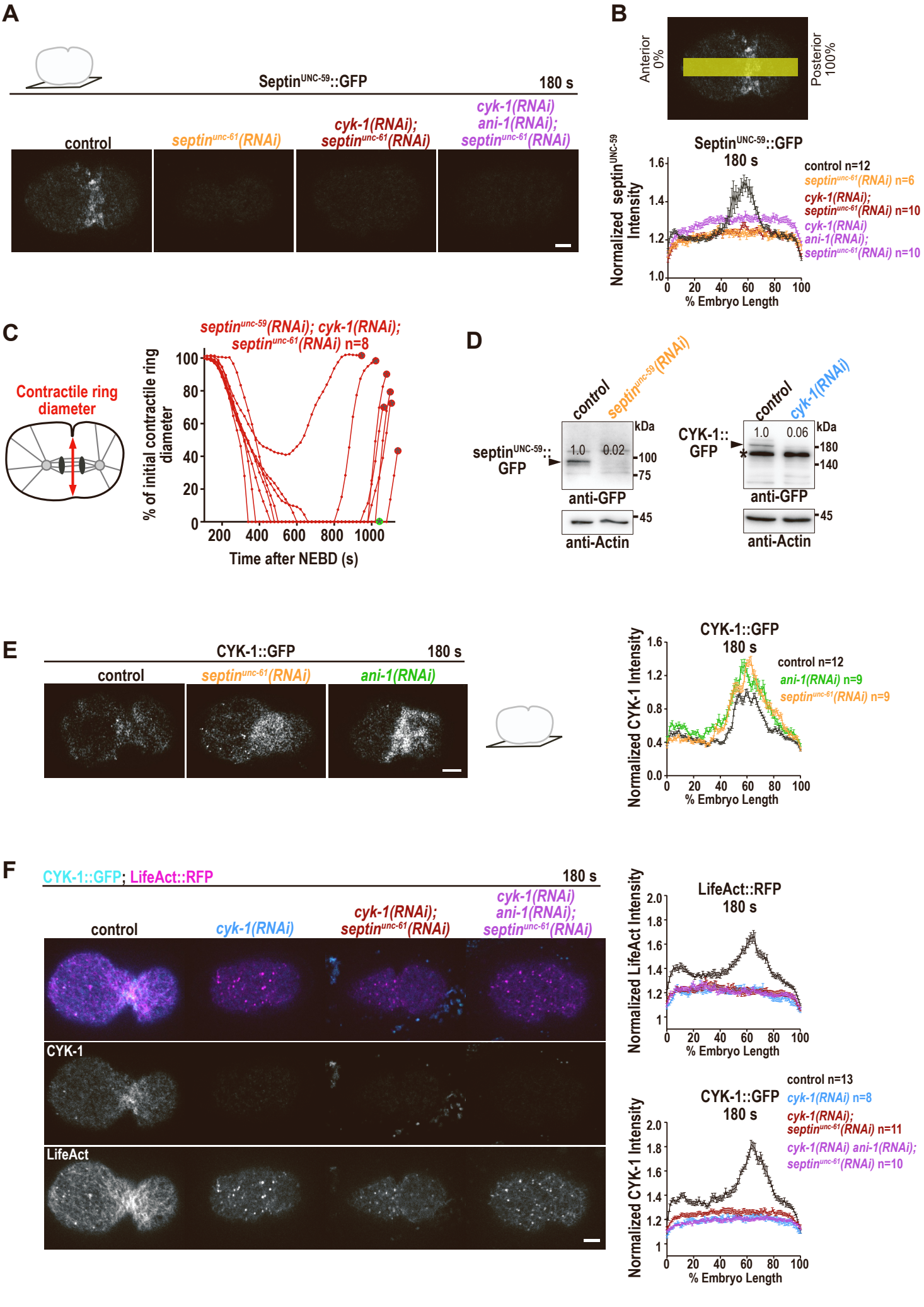

Figure S1 Single, double and triple RNAi co-depletions of CYK-1 and septin are highly efficient, related to Figure 1

A) Confocal single z-plane cortical images of endogenously tagged septin^{UNC-59}::GFP for indicated RNAi conditions 180 s after NEBD.

B) Normalized mean septin^{UNC-59}::GFP fluorescence intensity from the anterior (0% embryonic length) to the posterior (100%) cortex 180 s after NEBD for the indicated RNAi conditions.

C) The contractile ring diameter is plotted as % of the initial contractile ring diameter over time for individual embryos treated with *septin^{unc-59}(RNAi); cyk-1(RNAi); septin^{unc-61}(RNAi)*. Green and red encircled stars indicate whether embryos succeed or fail cytokinesis, respectively.

D) Immunoblot of septin^{UNC-59}::GFP and CYK-1::GFP expressing worms with and without *septin^{unc-59}(RNAi)* or *cyk-1(RNAi)* probed with antibodies against GFP and actin, as a loading control. The mean septin^{UNC-59}::GFP or CYK-1::GFP protein levels (3 worm extracts) are indicated, star indicates a non-specific band.

E) Confocal cortical single z-plane images of endogenously tagged CYK-1::GFP (left) and normalized mean CYK-1::GFP fluorescence intensity from the anterior to the posterior cortex 180 s after NEBD for indicated RNAi conditions (right).

F) Confocal cortical single z-plane images of endogenously tagged CYK-1::GFP (cyan) and LifeAct::RFP (magenta) expressing embryos for the indicated RNAi conditions 180 s after NEBD (left). Normalized mean CYK-1::GFP and LifeAct::RFP fluorescence intensity from the anterior to the posterior cortex 180 s after NEBD (right).

All scale bars are 5 µm, error bars are SEM and n=number of embryos analyzed.

Supplemental FIGURE 2

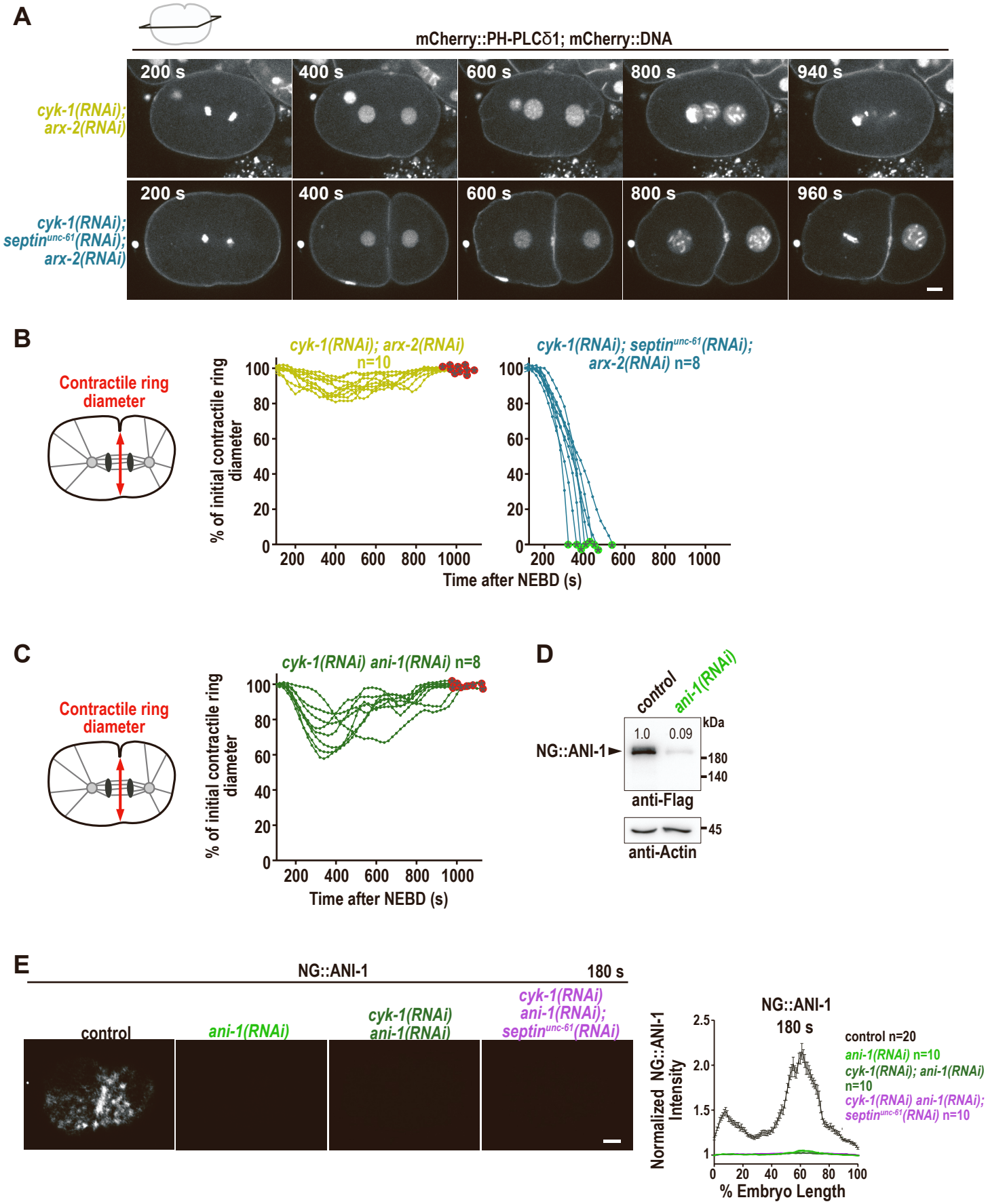

Figure S2 ARX-2 depletion does not prevent furrow ingression in *cyk-1(RNAi); septin^{unc-61}(RNAi)* embryos, related to Figure 1

A) Central plane images of embryos expressing the membrane marker mCherry::PH-PLCδ1 and mCherry::DNA (Histone-H2B) and treated with the indicated RNAi conditions.

B, C) The contractile ring diameter is plotted as % of the initial contractile ring diameter over time for individual embryos for indicated RNAi conditions. Green and red encircled stars indicate whether embryos succeed or fail cytokinesis, respectively.

D) Immunoblot of endogenously tagged NeonGreen::ANI-1 (NG::ANI-1) expressing worms with and without *ani-1(RNAi)* probed with antibodies against Flag and actin, as a loading control. The mean NG::ANI-1 protein levels (3 worm extracts) are indicated.

E) Confocal cortical single z-plane images of NG::ANI-1 (left) and normalized mean NG::ANI-1 fluorescence intensity from the anterior to the posterior cortex 180 s after NEBD for indicated RNAi conditions (right).

All scale bars are 5 µm, error bars are SEM and n=number of embryos analyzed.

Supplemental FIGURE 3

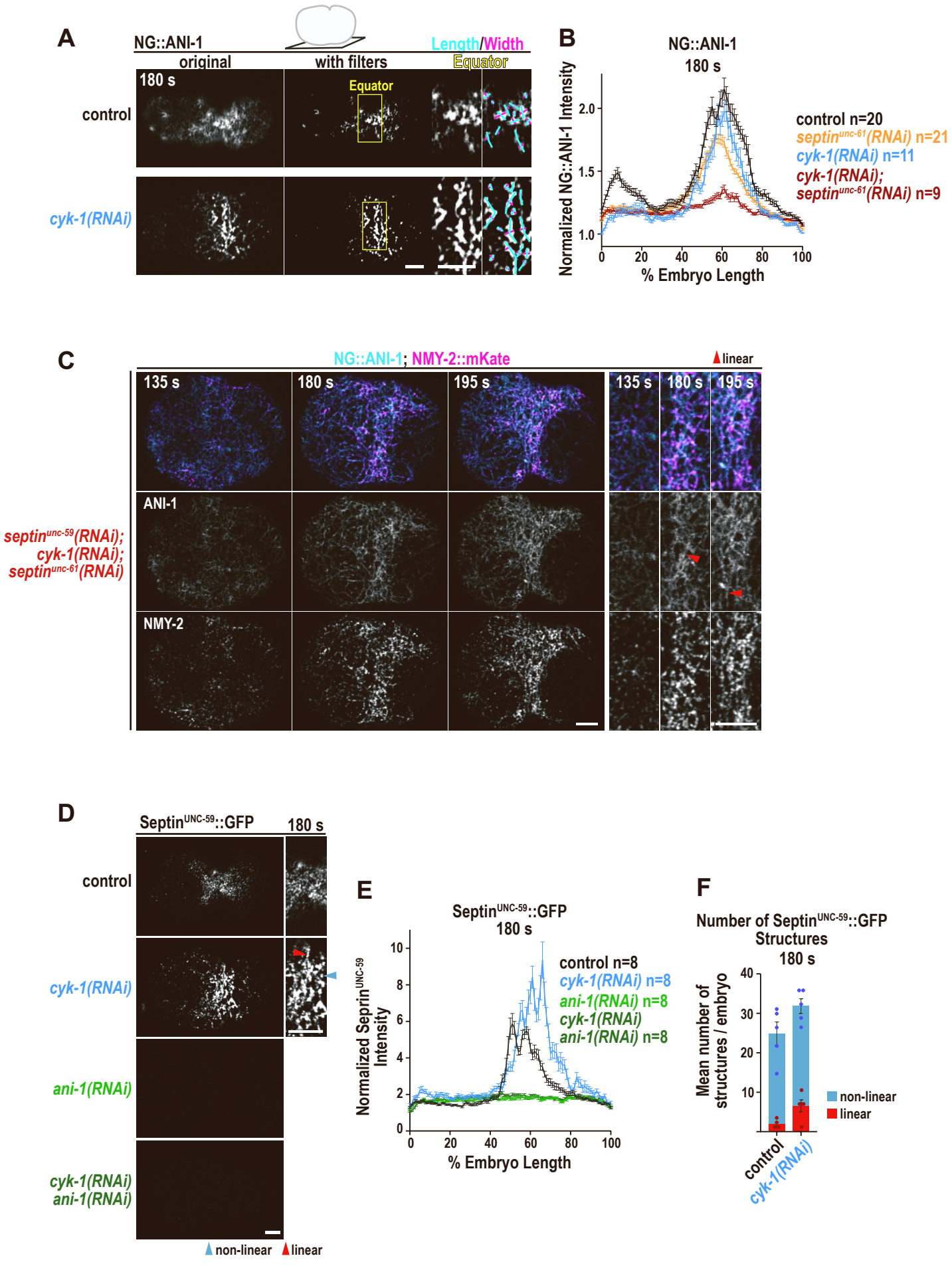

Figure S3 Equatorial septin^{UNC-59}::GFP levels are elevated after CYK-1 depletion and strongly reduced after ANI-1 depletion, related to Figure 2

A) After filtering the original image, the length and width of each structure was measured in a region at the cell equator unless stated otherwise. Structures with a length/with ratio ≥4 were classified as linear and a length/with ratio <4 as non-linear.

B) Mean normalized NG::ANI-1 fluorescence intensity from the anterior to the posterior cortex at 180 s after NEBD for indicated RNAi conditions. The control NG::ANI-1 graph is reproduced from Fig. S2E.

C) Confocal single z-plane images of the cell cortex of endogenously tagged NG::ANI-1 (cyan) and NMY-2::mKate (magenta) for *septin^{unc-59}(RNAi); cyk-1(RNAi); septin^{unc-61}(RNAi)* embryos. Magnification of the equatorial region of the same embryos are shown on the right.

D) Confocal single z-plane images and magnifications of the equatorial region of embryos with endogenously GFP-tagged septin^{UNC-59} at 180 s after NEBD are shown.

E) Mean normalized septin^{UNC-59}::GFP fluorescence intensity from the anterior to the posterior cortex for indicated RNAi conditions at 180 s after NEBD.

F) Mean number of septin^{UNC-59}::GFP structures per embryo for the indicated conditions at 180 s after NEBD. Dots represent data points of individual embryos.

Linear structures are highlighted by red and non-linear by blue arrowheads. Error bars are SEM, all scale bars are 5 µm, n=number of embryos analyzed.

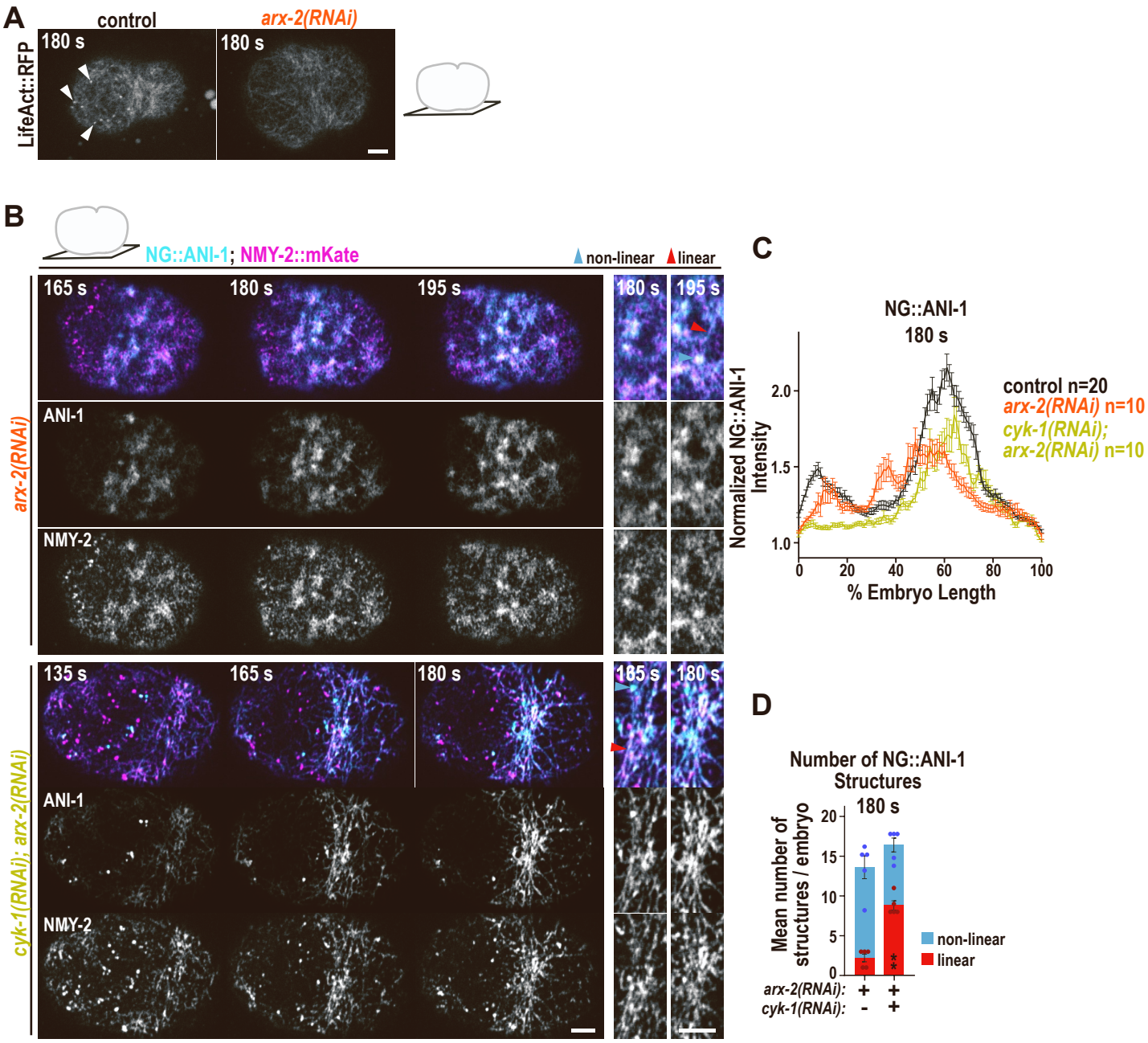

Figure S4 ARX-2 depletion does not influence NG::ANI-1 localization, related to Figure 2

A) Confocal single z-plane images of LifeAct::RFP for control and *arx-2(RNAi)* embryos at 180 s after NEBD. After *arx-2(RNAi)* F-actin puncta (white arrowheads) disappear.

B) Confocal single z-plane images of the cell cortex of NG::ANI-1 (cyan) and NMY-2::mKate (magenta) after *arx-2(RNAi)* or *cyk-1(RNAi); arx-2(RNAi)*. Magnification of the cell equator is shown on the right. Note: cleavage furrow ingression is delayed in *arx-2(RNAi)* in comparison to control embryos (compare with Fig. 2A, 180 s). Linear structures are highlighted by red and non-linear by blue arrowheads.

C) Normalized mean NG::ANI-1 fluorescence intensity from the anterior to the posterior cortex at 180 s after NEBD for indicated RNAi conditions. Control graph is reproduced from Fig. S2E and n=number of embryos analyzed.

D) The mean number of linear and non-linear NG::ANI-1 structures per embryo at an equatorial region for the indicated RNAi conditions at 180 s after NEBD. P-value was calculated using Mann-Whitney-U test and represents ** p<0.01 in comparison to *arx-2(RNAi)* treated embryos and dots represent data points of individual embryos.

All scale bars are 5 µm and error bars are SEM.

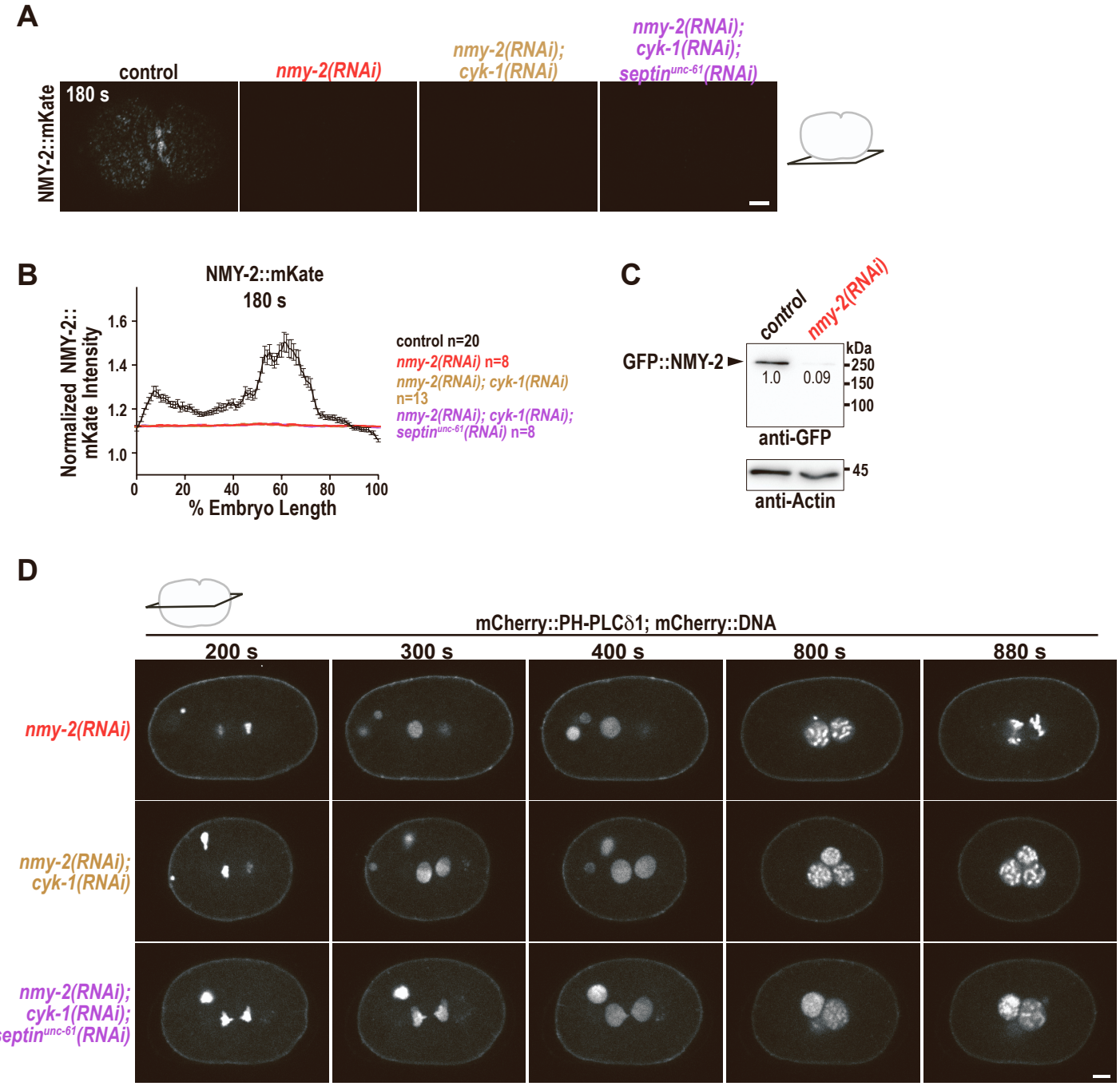

Figure S5 Single, double and triple RNAi co-depletions of NMY-2, CYK-1 and septin^{UNC-61} are highly efficient, related to Figure 3

A) Confocal single z-plane cortical images of NMY-2::mKate for indicated RNAi conditions 180 s after NEBD.

B) Graphs display the mean normalized NMY-2::mKate cortical fluorescence intensity for the indicated RNAi conditions 180 s after NEBD.

C) Immunoblots of adults worms expressing endogenously-tagged GFP::NMY-2 with or without *nmy-2(RNAi)* and probed with the indicated antibodies. The mean intensity of the GFP::NMY-2 band is shown (3 worm extracts).

D) Central plane images of embryos expressing the general membrane marker mCherry::PH-PLC1 and mCherry::DNA (Histone-H2B) and treated with the indicated RNAi conditions and time points after NEBD.

E) Normalized cortical NG::ANI-1 fluorescence intensity for indicated RNAi conditions 180 s after NEBD. Control graph reproduced from Fig. S2E.

Error bars are SEM, scale bars are 5 μm and n= number of embryos analyzed.

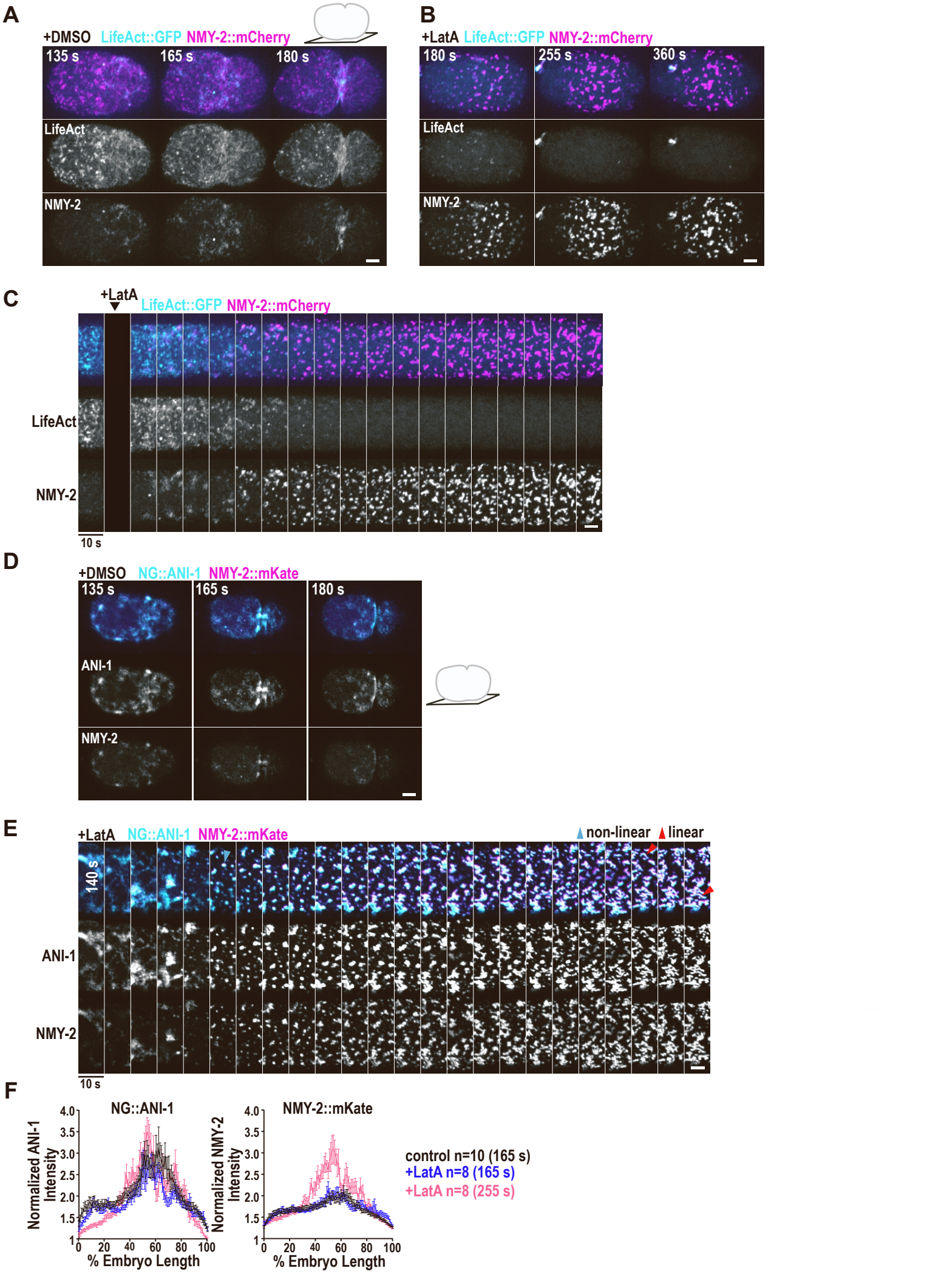
A
+DMSO LifeAct::GFP NMY-2::mCherry
135 s
165 s
180 s
LifeAct
NMY-2
B
+LatA LifeAct::GFP NMY-2::mCherry
180 s
255 s
360 s
LifeAct
NMY-2
C
+LatA
LifeAct::GFP NMY-2::mCherry
LifeAct
NMY-2
10 s
D
+DMSO NG::ANI-1 NMY-2::mKate
135 s
165 s
180 s
ANI-1
NMY-2
E
+LatA NG::ANI-1 NMY-2::mKate
non-linear
linear
140 s
ANI-1
NMY-2
10 s
F
NG::ANI-1
Normalized ANI-1 Intensity
% Embryo Length
NMY-2::mKate
Normalized NMY-2 Intensity
% Embryo Length
control n=10 (165 s)
+LatA n=8 (165 s)
+LatA n=8 (255 s)

Figure S6 Cortical fluorescence intensities of NMY-2::mKate and NG::ANI-1 after Latrunculin A treatment, related to Figure 4

A-C) Maximum intensity projections of 10 cortical z-planes of permeabilized one-cell embryos expressing NMY-2::mCherry (magenta) and LifeAct::GFP (cyan) treated with DMSO (A) or Latrunculin A (B, C). Panel (C) shows a kymograph of the equatorial region of the embryo in panel (B).

D, E) Maximum intensity projections of 10 cortical z-planes of permeabilized one-cell embryos expressing NMY-2::mKate (magenta) and NG::ANI-1 (cyan) treated with DMSO (D) or Latrunculin A (E). Panel (E) shows a kymograph of the equatorial region of the embryo of Fig. 4A.

F) Normalized mean cortical NMY-2::mKate and NG::ANI-1 fluorescence intensity from the anterior to the posterior cortex for control and Latrunculin A treated embryos at indicated time points.

Error bars are SEM, scale bars are 5 µm and n=number of embryos analyzed.

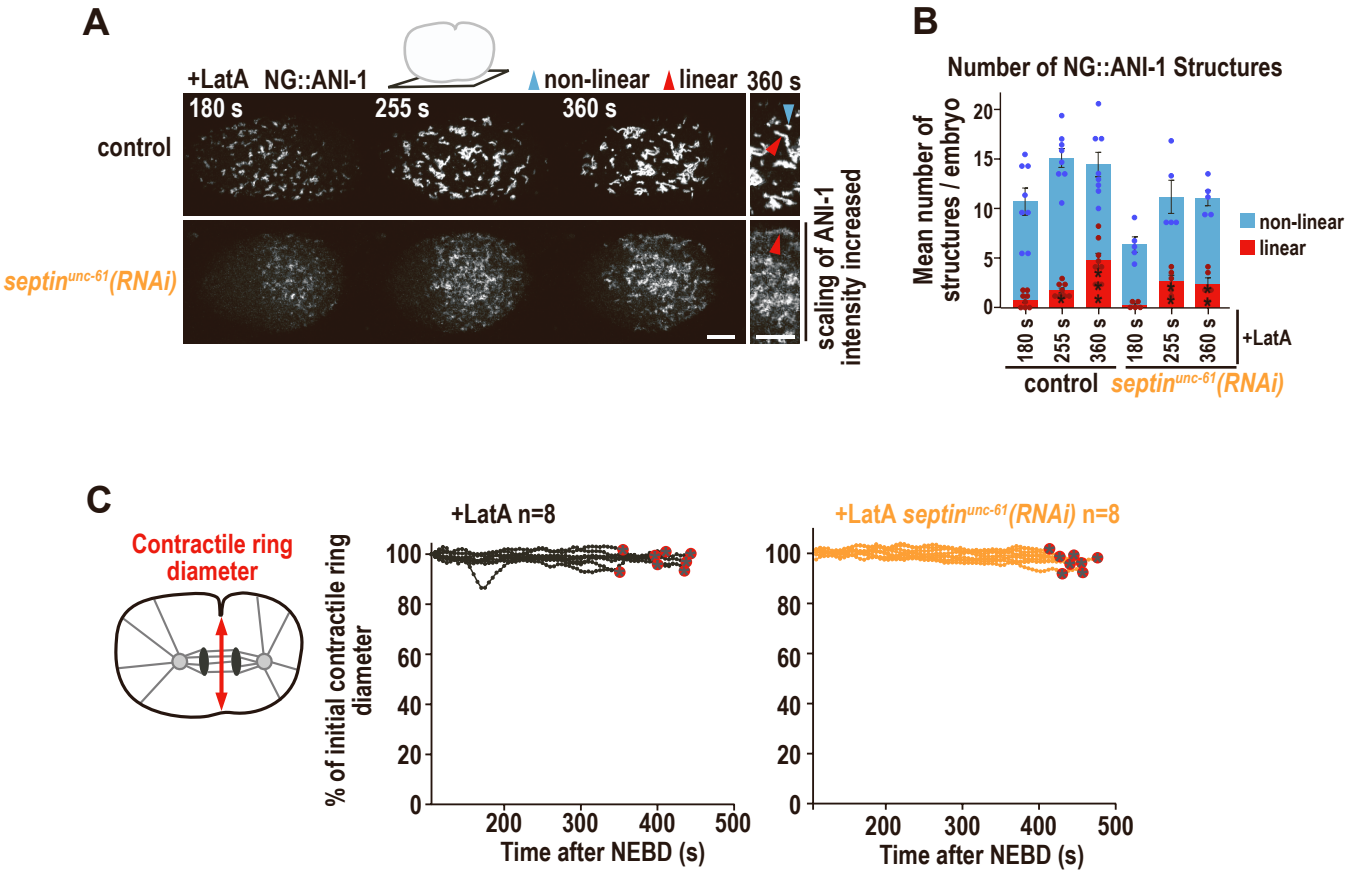

Figure S7 Septin^{UNC-61} facilitates linear structure formation in the absence of F-actin, related to Figure 4
A) Maximum intensity projections of 6 cortical z-planes of permeabilized one-cell embryos expressing NG::ANI-1 and treated without and with *septin^{unc-61}(RNAi)* and Latrunculin A. Intensity scaling of *septin^{unc-61}(RNAi)* embryo was increased.
B) Mean number of NG::ANI-1 structures at the cell equator per embryo without and with *septin^{unc-61}(RNAi)* and Latrunculin A treatment. Error bars are SEM, *P*-values were calculated using Mann-Whitney-U or student *t*-test and represent * p<0.05, ** p<0.01, *** p<0.001 in comparison to 180 s, dots represent data points of individual embryos. Control condition is reproduced from Fig. 4B.
C) Plotted is the contractile ring diameter of each embryo over time for Latrunculin A treated embryos with and without *septin^{unc-61}(RNAi)*, n=number of embryos analyzed. Red encircled stars indicate that embryos fail cytokinesis.

Supplemental FIGURE 8

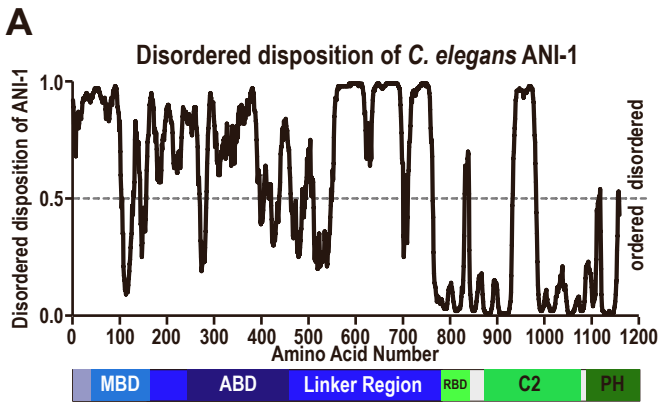

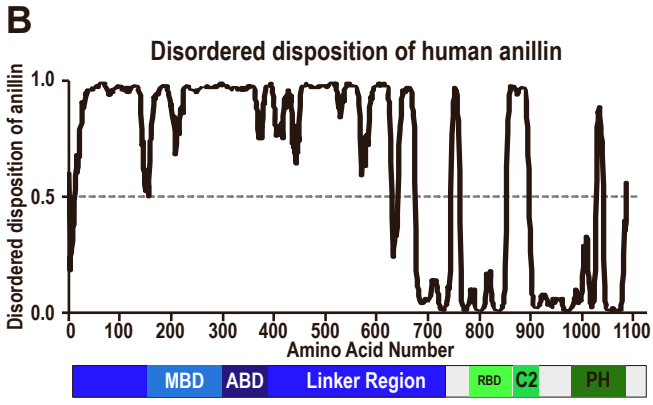

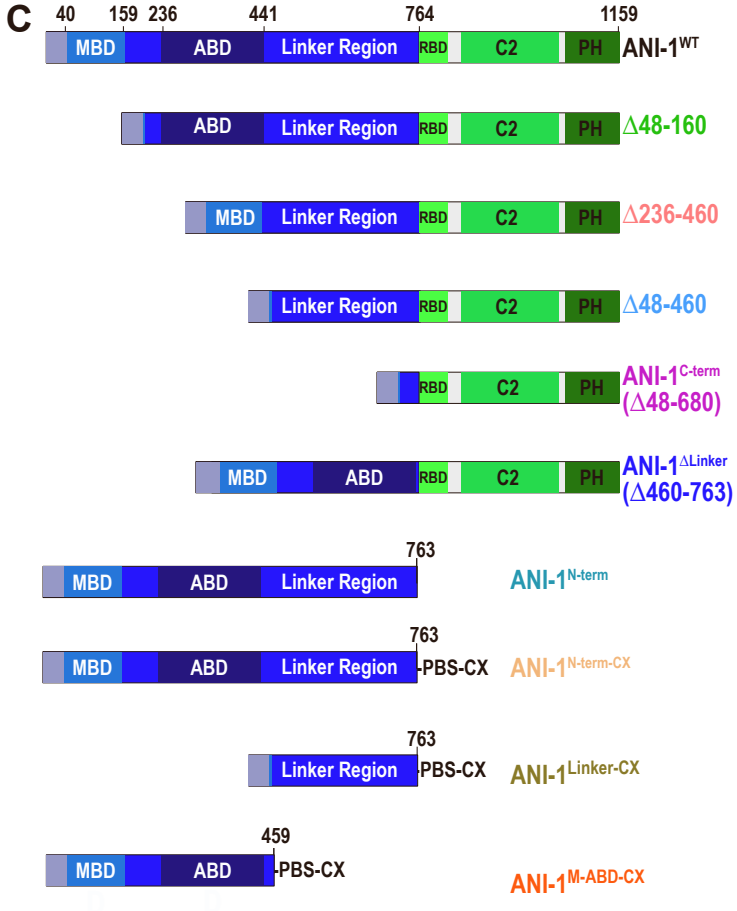

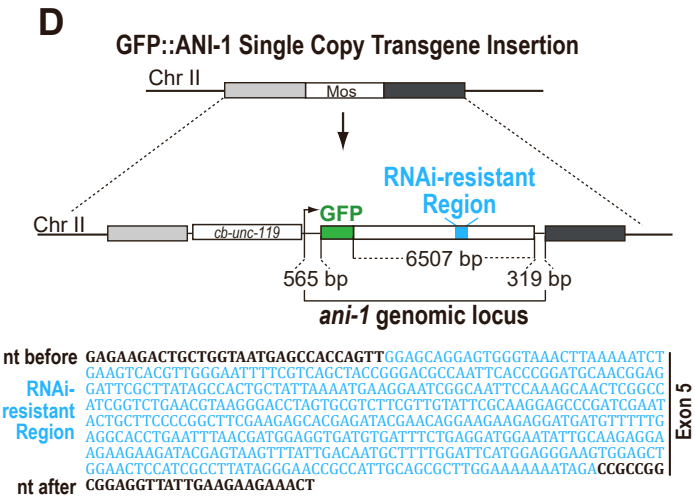

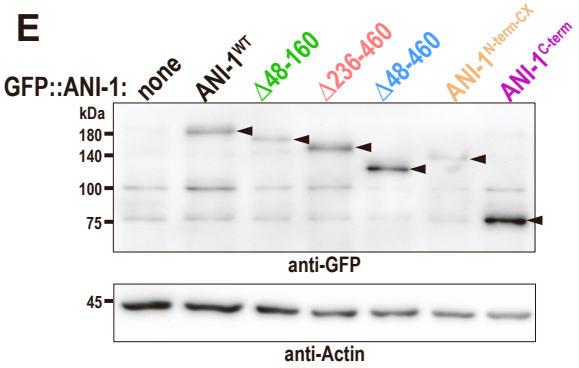

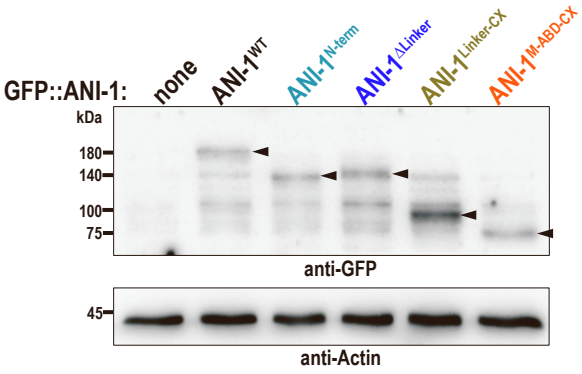

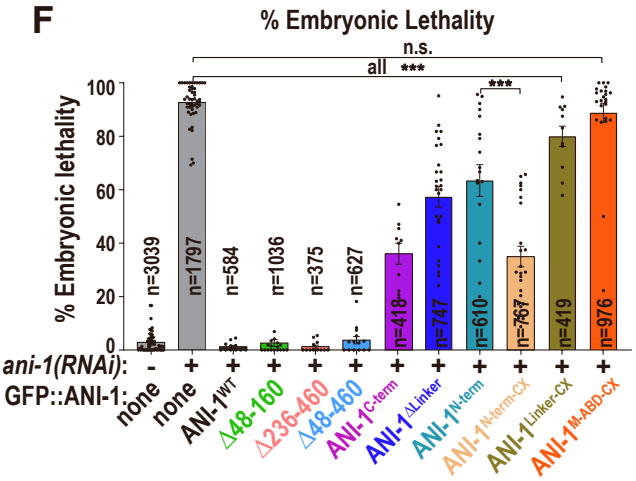

Figure S8 The N-terminal halves of *C. elegans* and human anillin are predicted to be highly disordered, related to Figure 5

A-B) Graphs display the predicted disordered regions of *C. elegans* ANI-1 and human anillin which were determine with DISOPRED3 [S2]. For comparison a scheme of their functional domains is shown below.

C) Schematic representation of GFP-tagged ANI-1^{WT} and tested ANI-1 mutant proteins.

D) GFP-tagged ANI-1 transgenes were integrated into the 'Mos' site on chromosome II. The ANI-1 transgenes comprise the genomic *ani-1* locus and *gfp*. Transgenes are resistant to *ani-1* RNAi targeting by re-encoding exon 5 but keeping the amino acid sequence and codon usage the same.

E) Immunoblots of adult worms expressing the indicated GFP-tagged ANI-1 proteins probed with anti-GFP and anti-actin antibodies.

F) Graph is plotting the mean percentage of embryonic lethality for the indicated GFP-tagged ANI-1 proteins and RNAi conditions. P-values were calculated using Mann-Whitney-U or student *t*-test and represent n.s. $p>0.05$ and *** $p<0.001$. Error bars are SEM and n= number of progeny (larvae and embryos) counted.

Supplemental FIGURE 9

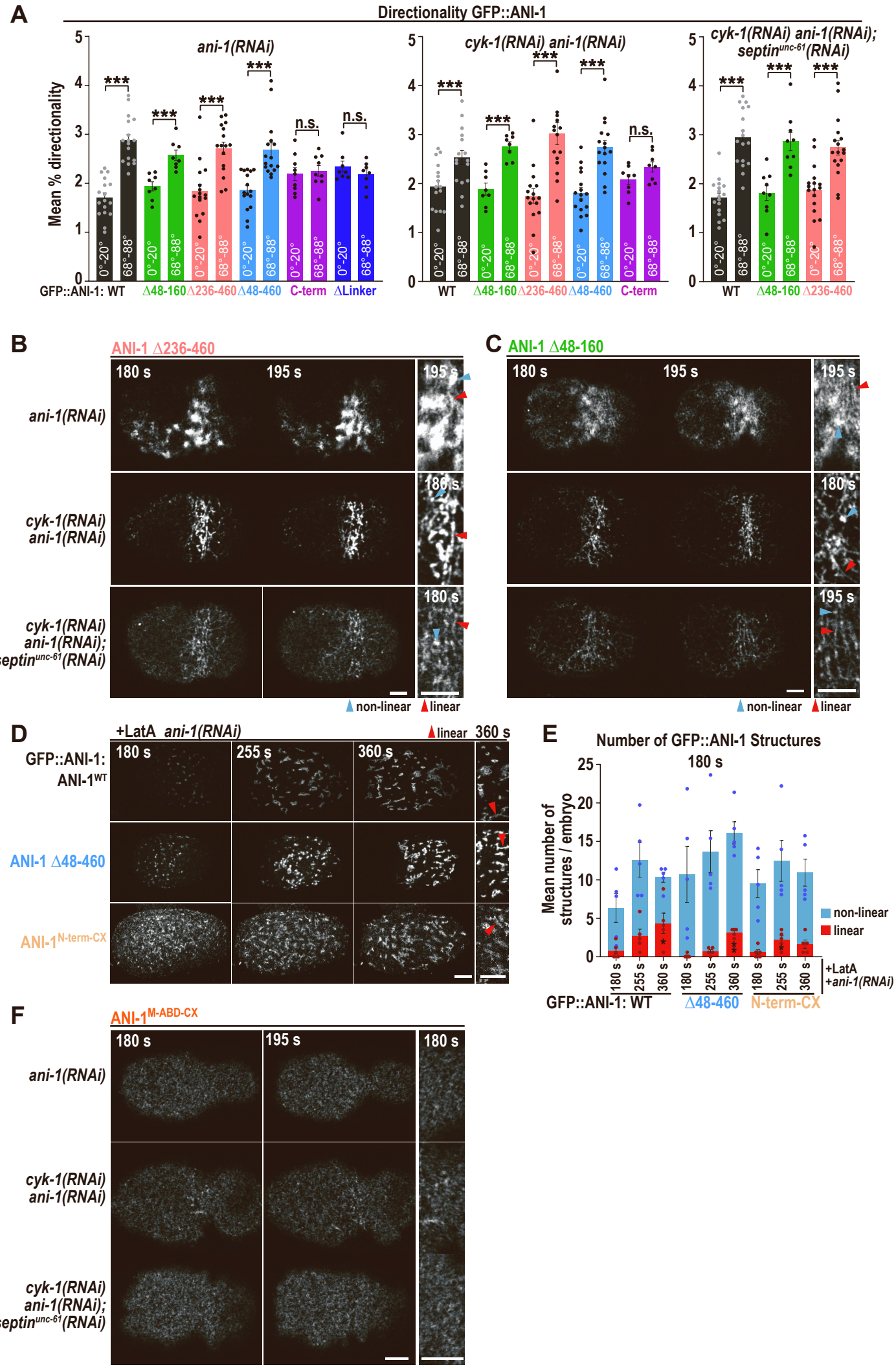

Figure S9 The MBD and ABD are not required for circumferential ANI-1 alignment, related to Figure 5

A) Mean percentage of 0-20º (anterior to posterior) and 68-88º (circumferentially) directionality measured for GFP-tagged ANI-1 proteins for indicated RNAi conditions 180 s after NEBD. *P*-values were determined with student *t*-test and represent *** $p<0.001$ and n.s. $p>0.05$.

B, C) Confocal cortical single z-plane images of GFP-tagged ANI-1 ∆236-460 (B) and ANI-1 ∆48-160 (C) expressing embryos for the indicated RNAi conditions and time points after NEBD. To better visualize the localization of GFP- tagged ANI-1 after septin^{UNC-61} co-depletion, the signal intensity scaling was increased in those conditions.

D) Maximum intensity projections of 6 cortical z-planes of permeabilized one-cell embryos expressing indicated GFP::ANI-1 transgenes and treated with Latrunculin A and *ani-1(RNAi).* Intensity scaling of ANI-1$^{N-term-CX}$ was increased.

E) Mean number of structures for indicated GFP::ANI-1 transgenes at the cell equator per embryo after *ani-1(RNAi)* and Latrunculin A treatment. *P*-values were calculated using Mann-Whitney-U or student *t*-test and represent * $p<0.05$, ** $p<0.01$ in comparison to 180 s.

F) Confocal cortical single z-plane images of GFP-tagged ANI-1$^{M-ABD-CX}$ expressing embryos for the indicated RNAi conditions and time points after NEBD.

For all cortical images: magnification of equatorial regions are shown on the right. Linear structures are highlighted by red and non-linear by blue arrowheads. Error bars are SEM and dots represent data points of individual embryos. Scale bars are 5 µm.

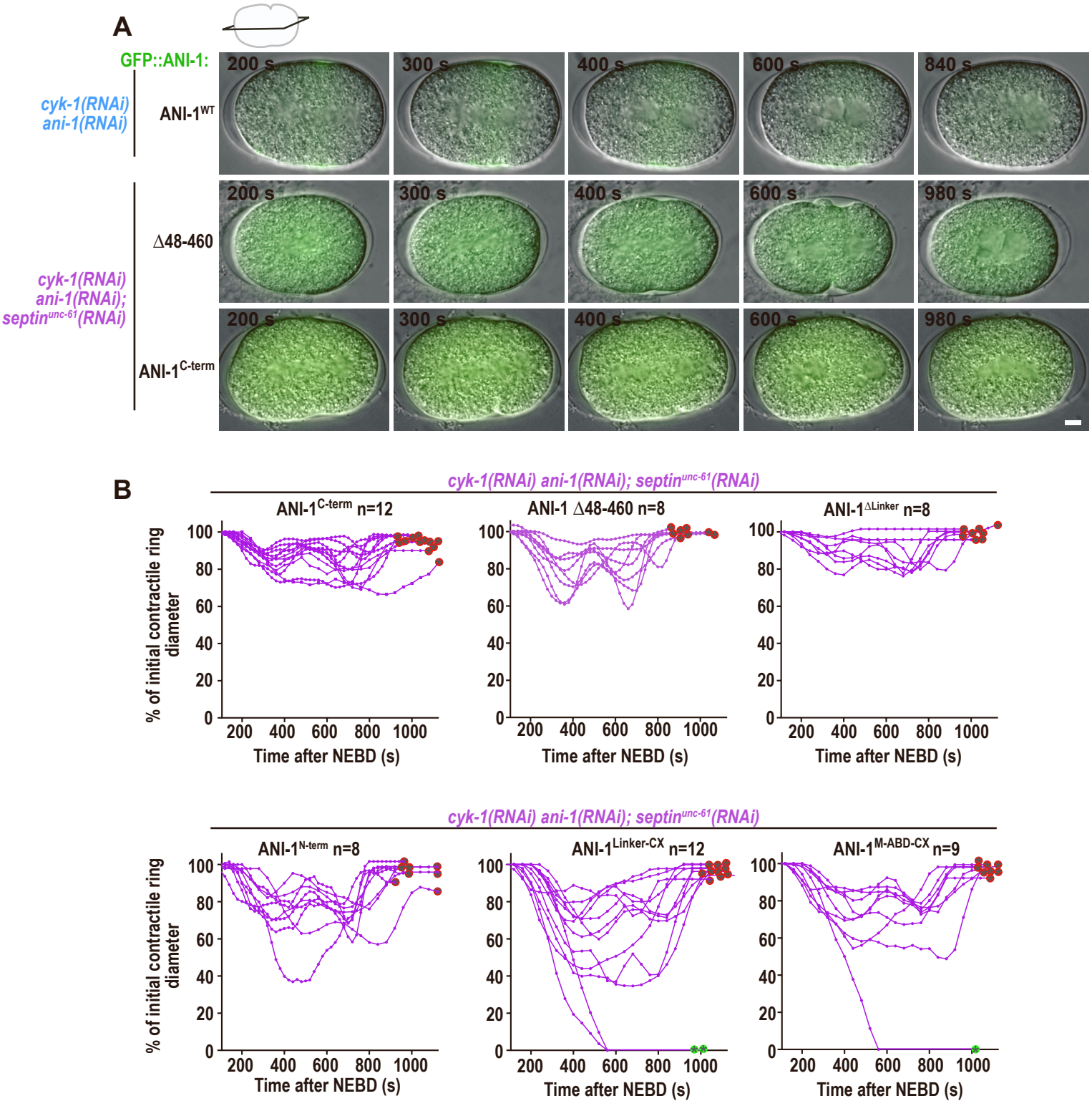

Figure S10 The Δ48-460 ANI-1 and ANI-1$^{C\text{-}term}$ mutants do not support furrow ingression after co-depletion of septins and formin, related to Figure 7

A) Merged central plane DIC and wide-field fluorescent images of the GFP-tagged ANI-1^{WT}, ANI-1$^{C\text{-}term}$ and ANI-1 Δ48-460 proteins for the indicated RNAi conditions and time points after NEBD. Scale bar is 5 μm.

B) Plotted is the contractile ring diameter of each embryo over time for indicated GFP-tagged ANI-1 mutant proteins and RNAi conditions, n=number of embryos analyzed. Green and red encircled stars indicate whether embryos succeed or fail cytokinesis, respectively.

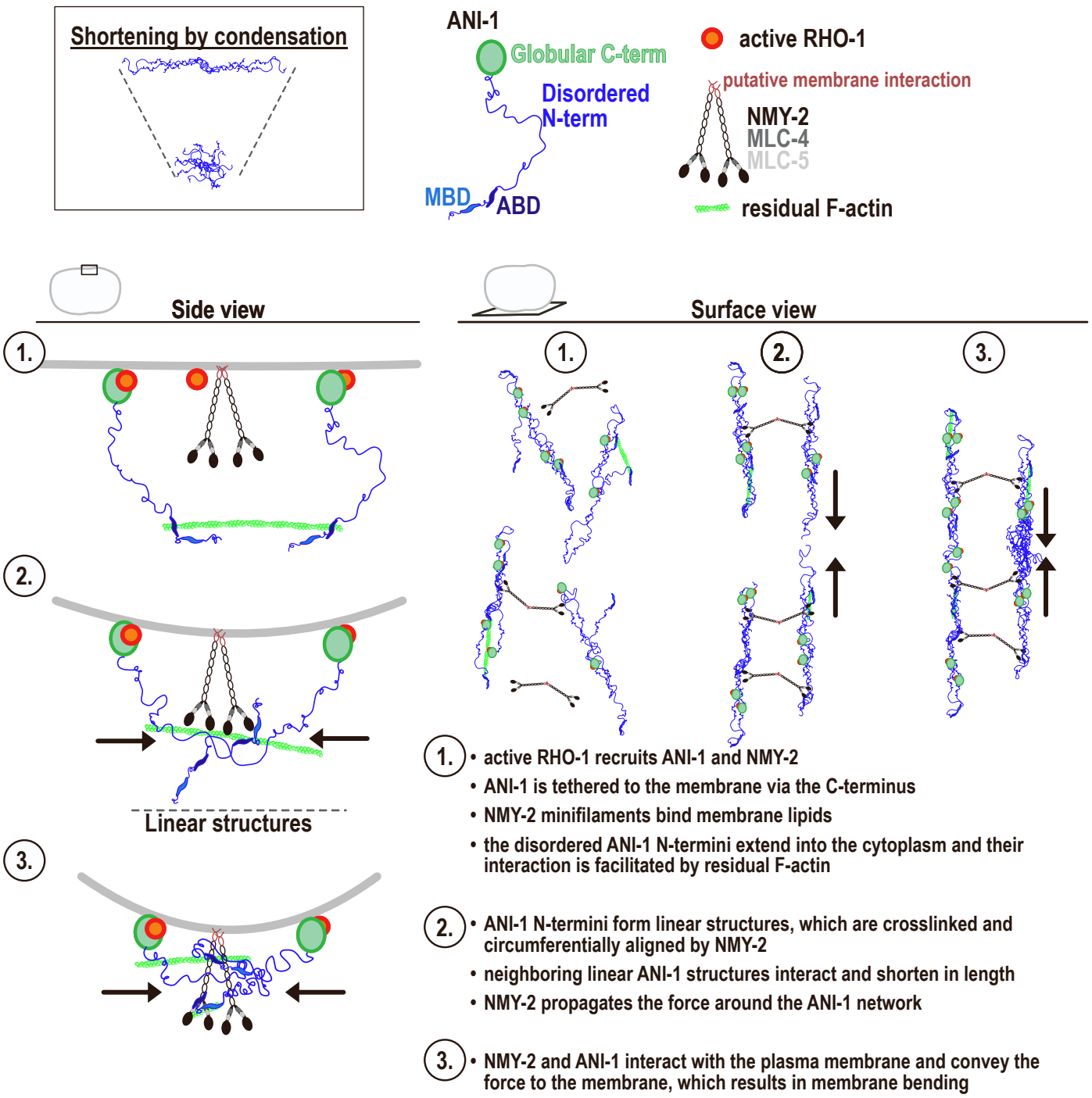

Figure S11, related to Discussion
Model illustrating how contraction of the ANI-1 network mediates cleavage furrow formation and ingression after the depletion of septins and formin.

Supplemental References:

[S1] Carvalho, A., S.K. Olson, E. Gutierrez, K. Zhang, L.B. Noble, E. Zanin, A. Desai, A. Groisman, and K. Oegema. 2011. Acute Drug Treatment in the Early *C. elegans* Embryo. PLoS ONE. 6:e24656-24658.

[S2] Jones, D.T., and D. Cozzetto. 2015. DISOPRED3: precise disordered region predictions with annotated protein-binding activity. Bioinformatics (Oxford, England). 31:857-863.